UNIVERSITY OF CALIFORNIA, SAN DIEGO

Design, fabrication and characterization of optical microcavities for application specific optical devices

A dissertation submitted in partial satisfaction of the requirements

for the degree Doctor of Philosophy

in

Electrical and Computer Engineering (Photonics)

by

Chyong-Hua Chen

Committee in charge

Professor Yeshaiahu Fainman, Chair
Professor Paul. K.L. Yu
Professor Kevin Quest
Professor Lu Jeu Sham
Professor Shu Chien

2006

The dissertation of Chyong-Hua Chen is approved, and it is acceptable in quality and form for publication on microfilm:

_____

_____

_____

_____

_____

Chair

University of California, San Diego

2006

Dedication

To my parents, friends, and colleagues,

I am deeply indebted for inspiration, support, encouragement and considerations. Without all of you, the success of this project and the completion of this thesis would not be possible.

Table of Contents

List of Figures

List of Tables

Acknowledgements

The text of Chapter 4, in part or in full, is a reprint of the material as it appears in the Applied Optics. The dissertation author was the primary researcher and/or author and the co-authors listed in this publication directed and supervised the research which forms the basis for this chapter.

The text of Chapter 5 and 6, in part or in full, is a reprint of the material as it appears in the Applied Optics. The dissertation author was the primary researcher and/or author and the co-authors listed in this publication directed and supervised the research which forms the basis for this chapter.

The text of Chapter 7, in part or in full, is a reprint of the material as it appears in the Optics Express. The dissertation author was the primary researcher and/or author and the co-authors listed in this publication directed and supervised the research which forms the basis for this chapter.

VITA

1991~1995 Bachelor of Science in Electrical Engineering department from National Tsing-Hua University in Taiwan

1995~1997 Master of Science in Electrical Engineering department from National Tsing-Hua University in Taiwan

1997~1998 Associate Engineer in Opto-Electronics & Systems Laboratories of the Industrial Technology Research Institute in Taiwan

1998~1999 Teaching assistant in Electrical Engineering department of National Tsing-Hua University in Taiwan

1999~2006 Doctor of Philosophy in Electrical and Computer Engineering (Photonics) from University of California, San Diego

PUBLICATIONS

Guy Klemens, Chyong-Hua Chen, and Yeshaiahu Fainman, "Design of optimized dispersive resonant cavities for nonlinear wave mixing," Opt. Express **13,** 9388-9397 (2005), http://www.opticsexpress.org/abstract.cfm?URI=OPEX-13-23-9388

L. Pang, K. Tetz, Y. Shen, C. H Chen and Y. Fainman, "Photosensitive quantum dot composites and their applications in optical structures", J. Vac. Sci. Technol. B 23, 2413-2418 (2005)

Chyong-Hua Chen, Lin Pang, Chia-Ho Tsai, Uriel Levy and Y. Fainman, "Compact and integrated TM-pass waveguide polarizer", Optics Express 13, 5347-5352 (2005) http://www.opticsexpress.org/abstract.cfm?URI=OPEX-13-14-5347

Chyong-Hua Chen, Kevin Tetz, and Y Fainman, " Resonant-cavity-enhanced PIN photodiode with broad quantum efficiency spectrum by use of an anomalous dispersion mirror," Applied Optics 44(29) 6131-6140, (2005)

Chyong-Hua Chen, Kevin Tetz, Wataru Nakagawa, and Y. Fainman, " Wide-field-of-view GaAs/AlxOy one-dimensional photonic crystal filter," Applied Optics 44 (8), 1503-1511 (2005)

W Nakagawa, Pang-Chen Sun, Chyong-Hua Chen, and Y Fainman, " Wide-field-of-view narrow-band spectral filters based on photonic crystal nanocavities, " Optics Letters 27(3), 191-3 (2002)

ABSTRACT OF THE DISSERTATION

Design, fabrication and characterization of optical microcavities for application specific optical devices

by

Chyong-Hua Chen

Doctor of Philosophy in Electrical and Computer Engineering (Photonics)

University of California, San Diego, 2006

Professor Yeshaiahu Fainman, Chair

Microresonators are widely used in the creation of optical devices which exploit their unique properties and characteristics such as spectral selectivity and field localization. We investigate two applications for microresonator devices that integrate multiple functionalities into the same volume through application specific design optimization. The first application is in free-space optical communications, where we develop a bandpass filter and an optical receiver which are integrated together. The second is in the guided wave application, where we develop a waveguide polarizer and a waveguide bandpass filter.

For the first free-space communication application, we examine how the functionalities of a flat-top passband and a wide angular bandwidth can be integrated with a photodetector by exploiting properties of 1-D photonic crystals with multiple defects. In the first part of the research, we achieve a thin-film bandpass filter by optimally choosing the optical thickness ratio of high to low refractive-index materials in dispersive mirrors and experimentally characterize the fabricated device, demonstrating a bandwidth of 65 nm and field of view of 50°. In the second part, we integrate a photodetector into the resonator using the dispersive mirrors to achieve these functionalities. We fabricate and characterize the resulting device: a back-illuminated $In_{0.47}Ga_{0.53}As$-based resonant-cavity-enhanced PIN photodiode, showing 0.80 peak quantum efficiency, 35.96nm spectral bandwidth and 30° angular bandwidth.

For our second application involving guided wave components, we develop two devices, a waveguide polarizer and a waveguide bandpass filter. The waveguide polarizer device uses nanostructures to realize highly birefringent waveguides. With an appropriately sized nanostructure, a waveguide can be fashioned that allows only TM-like modes to propagate through the waveguide. We create such a polarizer using nanostructures of 26 μm lengths in a GaAs/AlAs ridge waveguide, providing an insertion loss of 0.54 dB and an extinction ratio of 20 dB. In the waveguide bandpass filter device, the methodology used to design thin-film filters in our first free-space application is extended and optimized for designs using microcavities in a photonic bandgap monorail waveguide. We present a square waveguide filter centered at 1554 nm with a maximum transmission of 0.88 and a FWHM of 13.6 nm.

Chapter 1 Introduction

1.1 Motivation

Microresonators confine light to a small volume by resonant recirculation, leading to critical enhancement of the internal optical fields. As such, devices utilized with microresonators play a significant role in a large variety of applications. For example, microcavities made of active III-V semiconductor materials are used for resonant cavity-enhanced photodetectors [1], light-emitting diodes [2], low-threshold lasers [3] and fast optical switches [4]. In addition, with the benefit of wavelength selectivity property, microresonators are essential components in realization of filters, multiplexers (add) and demultiplexers (drop) in wavelength division multiplexed (WDM) lightwave systems [5]-[9].

On the basis of the confinement methods, microcavties are classified into three major categories: (1) Fabry-Perot resonators, (2) whispering gallery structures and (3) photonic crystals. In the first category, the cavity is created by introducing a gap (defect) between two high-reflectivity mirrors implemented either by 1-D photonic crystals or by grating-like structures [6],[10]-[14]. Representative examples are shown in Fig. 1-1. In the second category, the microresonator supports whispering gallery modes and is obtained by either microring or microdisk structures, typically coupled to two single-mode waveguides [15]-[19]. Example structures are shown in Fig. 1-2. In the last category, the microresonator is realized by introducing a small defect inside the photonic bandgap structure with 2-D or 3-D confinement as shown in Fig. 1-3 [20]-[22].

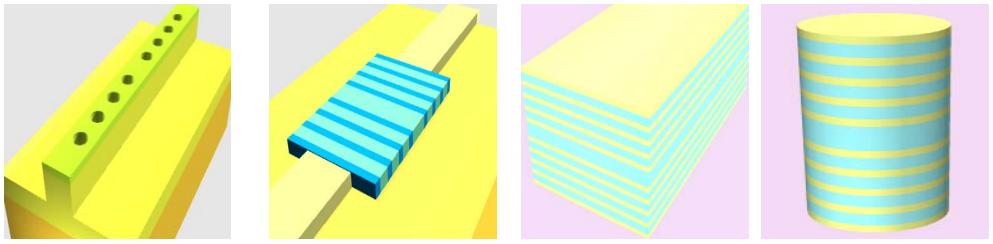

(a) (b) (c) (d)

Fig. 1-1 Fabry-Perot resonant structures: (a) Photonic bandgap microcavity waveguide (b) Bragg microcavity waveguide, (c) 1-D photonic crystal cavity (d) micropillar cavity.

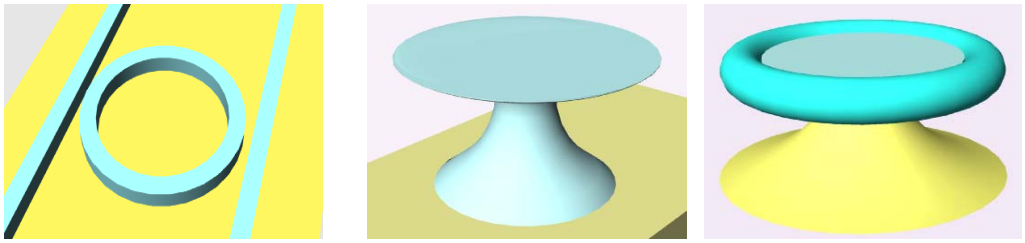

(a) (b) (c)

Fig. 1-2 Whispering gallery structures: (a) microrings, (b) microdisks and (c) microtoroids

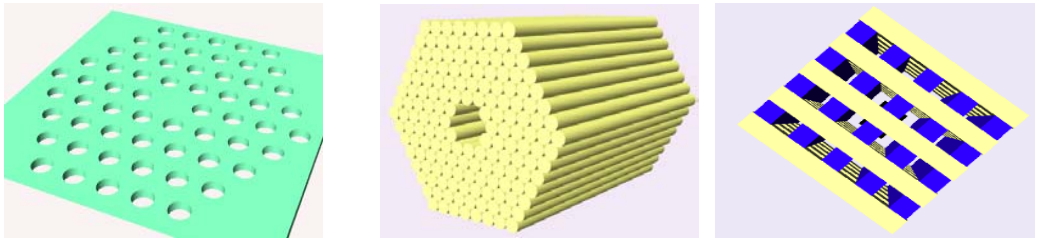

(a) (b) (c)

Fig. 1-3 Photonic crystal microcavities: (a) 2-D photonic crystal slab with defect (b) 2-D photonic crystal rods with defect and (c) 3-D photonic crystal cavity.

Application specific optical (ASO) devices are custom optical components tailored for a specific application while incorporating the functionalities of several devices into a subsystem integrated on a chip. In addition to being compatible with current fabrication technology, resulting in a significant cost reduction, these devices provide the benefits of higher performance, stable alignment, compactness and light-weight. For example, in order to couple the signal and pump source into an Erbium

doped fiber, and to avoid reflected light propagating back into the laser, a wavelength division multiplexing (WDM) filter and an isolator are added to the device. To miniaturize the sizes of these two components and to reduce the insertion loss resulting from connecting them, an IWDM (isolator-WDM hybrid) is realized. The hybrid device satisfies these functionalities with the benefit of reduction of insertion loss and better stability [23].

To accomplish these multiple-functionalities, the design methodology necessitates simultaneously addressing and optimizing performance characteristics, such as spectral bandwidth, angular bandwidth, polarization, etc. The objective of this thesis is to apply optical Fabry-Perot micro or nano-cavities to achieve miniaturization and integration of ASO devices for optical communication applications. Two major applications are being addressed in this thesis: one is the wide field-of-view photodetection system for the free-space optical communication and the other is on-chip polarization dependent photonic guided-wave devices for WDM lightwave systems. This work will focus on (1) the development of design techniques to mathematically analyze the photonic devices and systemically establish the design processes and (2) fabrication and characterization of these ASO devices.

1.2 Dissertation organization

The dissertation is organized as follows. Chapter 2 reviews the mathematical modeling tools used in the subsequent chapters. The characteristic matrix denotes the field properties inside the multilayer film, and the bidirectional eigenmode propagation method accurately describes the field propagation in each section of the waveguides. Via

the multiplication of the characteristic matrix for each layer or section, the relation between input and output fields are obtained, thereby obtaining the transmission and reflections properties of the entire device.

Chapter 3 describes the design methodology to synthesize optical bandpass filters by use of mircocavities in cascade. Based on Smith's method, we show that the wavelength-dependent mirrors play a prominent role in the determination of the transfer function. To achieve a flat-top passband, the mirror needs to have anomalous dispersion in reflection phase. Here, we present the design rules to achieve the desired dispersion characteristics by using coupled cavities, and we provide an example to demonstrate the design algorithms for an optical bandpass filter.

Chapter 4 presents the design and the characterization of an optical bandpass filter with a flat-top transmission band and a wide field-of-view by using 1-D photonic crystals. By integrating the aforementioned methodology with concepts that reduce the angular sensitivity, a bandpass filter with a field of view of ±50° is realized. The effect of the various design parameters on the performance of the device is discussed. The fabricated device is characterized and compared to the simulated results.

Chapter 5 develops the techniques to analyze the photodector embedded in microcavities and discusses the optimization of such devices with flat-top transmission and wide field of view. We obtain a semi-analytic formula to describe this type of photodetectors and to find the optimal conditions to achieve a flat-top quantum efficiency. In addition, we demonstrate bandwidth engineering by tuning the thickness of the active layer and the resonant cavities. We also discuss the sensitivity of the angular spectrum by tuning of the active layer thickness as well as the thickness ratio of the Bragg mirrors.

Chapter 6 presents the fabrication and characterization of the photodiode (PD) device. The effects of deviation from the design parameters on the performance of the resonated-cavity-enhanced (RCE) PD are discussed. Quantum efficiency, angular sensitivity and frequency response of the devices are measured and compared to the simulated results.

Chapter 7 describes the approach of introducing nanostructures into an optical waveguide and its advantage for the design of a TM-pass waveguide polarizer. The inserted nanostructures introduce form birefringence into the waveguide, and with proper choice of parameters the TE-like mode can be designed to radiate into the substrate. The properties of such waveguide polarizers, such as extinction ratio, insertion loss, and wavelength dependency, are discussed and simulated using the 3-D finite difference time domain (FDTD) method.

Chapter 8 establishes the design rules to obtain a waveguide bandpass filter with a flat-top transmission band and a wide stop band by introducing photonic bandgap microcavities into the waveguides. Using bidirectional eigenmode propagation method, it is found that the losses in the photonic bandgap mirrors dominate the performance of the filter, in particular its maximal transmission and the quality (Q) factor. To minimize the loss and to enhance the performance, mode-matching sections are added into the mirror structure. By analogy with the methodology presented in Chapter 3, we realize a bandpass waveguide filter with a flat-top passband and a wide stop band by introducing multiple microcavities into the photonic bandgap mirrors in the waveguides.

Chapter 9 summarizes the thesis and discusses potential future research directions.

References

[1] B Temelkuran, E Ozbay, JP Kavanaugh, G Tuttle, and KM Ho, "Resonant cavity enhanced detectors embedded in photonic crystals," Appl. Phys. Lett. 72 (19), 2376-2378 (1998)

[2] O Painter, J Vuckovic, and A Scherer, "Defect modes of a two-dimensional photonic crystal in an optically thin dielectric slab," J Opt. Soc. Am. B 16 (2), 275-285 (1999)

[3] M Loncar, T Yoshie, A Scherer P, Gogna, and YM Qiu , "Low-threshold photonic crystal laser," Appl. Phys. Lett. 81 (15), 2680-2682 (2002)

[4] PR Villeneuve, DS Abrams, SH Fan, and JD Joannopoulos, "Single-mode waveguide microcavity for fast optical switching," Opt. Lett. 21 (24), 2017-2019 (1996)

[5] Z. Zhang and M. Qiu, "Compact in-plane channel drop filter design using a single cavity with two degenerate modes in 2D photonic crystal slabs," Opt. Express 13(7), 2596-2604 (2005), http://www.opticsexpress.org/abstract.cfm?URI=OPEX-13-7-2596

[6] K J. Vahala, "Optical microcavities," Nature 424, 839-846 (2003)

[7] A Sharkawy SY, Shi, and DW Prather, "Multichannel wavelength division multiplexing with photonic crystals," Appl Opt. 40(14), 2247-2252(2001)

[8] G.T Paloczi,. J Scheuer, and A Yariv, "Compact microring-based wavelength-selective inline optical reflector," IEEE Photonics Technol. Lett. 17(2), 390-392 (2005)

[9] S.T Chu, B.E. Little, W Pan, T Kaneko, S Sato and Y Kokubun, "An eight-channel add-drop filter using vertically coupled microring resonators over a cross grid," IEEE Photonics Technol. Lett. 11(6), 691-693(1999)

[10] P Rigby, TF Krauss, "Photonics - The Vs and Qs of optical microcavities," Nature 390(6656), 125-125 (1997)

[11] F Giorgis, "Optical microcavities based on amorphous silicon–nitride Fabry–Pérot structures," Appl. Phys. Lett 77(4), 522-524 (2000)

[12] NG Stoltz, M Rakher, S Strauf, A Badolato, DD Lofgreen, PM Petroff, LA Coldren, D Bouwmeester, "High-quality factor optical microcavities using oxide apertured micropillars," Appl Phys. Lett 87 (3), 031105(2005)

[13] TF Krauss, B Vogele, CR Stanley, RM DelaRue, "Waveguide microcavity based on photonic microstructures," IEEE Photonic Technol. Lett. 9 (2), 176-178 (1997)

[14] JS Foresi, PR Villeneuve, J Ferrera, ER Thoen, G Steinmeyer, S Fan, JD Joannopoulos, LC Kimerling, HI Smith, EP Ippen, "Photonic-bandgap microcavities in optical waveguides," Nature 390 (6656), 143-145 (1997)

[15] QF Xu, B Schmidt, S Pradhan and M Lipson, "Micrometre-scale silicon electro-optic modulator," Nature 435 (7040), 325-327 (2005)

[16] TJ Kippenberg, SM Spillane, KJ Vahala, "Demonstration of ultra-high-Q small mode volume toroid microcavities on a chip," Appl Phys. Lett. 85 (25), 6113-6115 (2004)

[17] DK Armani, TJ Kippenberg, SM Spillane, KJ Vahala, "Ultra-high-Q toroid microcavity on a chip," Nature 421(6926), 925-928 (27 2003)

[18] D Armani, B Min, A Martin, KJ Vahala, 'Electrical thermo-optic tuning of ultrahigh-Q microtoroid resonators," Appl. Phys. Lett. 85 (22), 5439-5441(2004)

[19] E. Peter, I. Sagnes, G. Guirleo, S. Varoutsis, J. Bloch, A. Lemaître, and P. Senellart, "High-Q whispering-gallery modes in GaAs/AlOx microdisks," Appl. Phys. Lett. 86, 021103 (2005)

[20] A Scherer, O Painter, B D'Urso, R Lee, and A Yariv, "InGaAsP photonic band gap crystal membrane microresonators," J Vac. Sci. & Technol. B 16 (6), 3906-3910 (1998)

[21] A Scherer, O Painter, J Vuckovic, M Loncar, T Yoshie, 'Photonic crystals for confining, guiding, and emitting light," IEEE Trans Nanotechnol. 1 (1), 4-11 (2002)

[22] HG Park, JK Hwang, J Huh, HY Ryu, SH Kim, JS Kim, YH Lee, "Characteristics of modified single-defect two-dimensional photonic crystal lasers," IEEE J quantum electronics 38(10), 1353-1365 (2002)

[23] Information of IWDM Hybrid could be found in the following addresses: http://www.fiber-resources.com/newpic/2004112942403109.pdf
www.oplink.com/pdf/Mini_WDIH.pdf

Chapter 2 Reviews of the Design Models and Analysis

In this chapter, we review the mathematical models used to design and analyze the microcavity-based devices. Two different methods are described: one is the characteristic matrix method [1]-[6] and the other is the bidirectional eigenmode propagation method [7]-[9]. The former is widely applied for the design and the analysis of thin film multilayers while the latter is used to describe the propagation of the optical field within the waveguide. The chapter is organized as follow: in Section 2.1, the boundary conditions for a single layer, as stem form Maxwell equations are arranged in a notation of matrix known as a characteristic matrix. Section 2.2 shows the matrix calculation for a multilayer structure and Section 2.3 derives the transmission and the reflection from the multilayer structures by using the elements of the matrix. Section 2.4 briefly reviews the properties of periodic stacks. Section 2.5 overviews the method of bidirectional eigenmode propagation and demonstrates its relation to the transfer matrix method.

2.1 Characteristic matrix of a single film

Consider the linearly polarized wave shown in Fig. 2-1 impinging on a thin dielectric film between two semi-infinite transparent media. The film is assumed to be homogeneous, isotropic and of uniform thickness with refractive index n_1 and thickness d_1. The refractive indices of the input and output media are n_0 and n_s, respectively. Suppose that the monochromatic incident wave is

$$E_i = E_{il} e^{i(k_{il} \cdot r - \omega_i t)} \quad \text{.....(2.1)}$$

where E_{iI} is the amplitude of the field with a constant value, k_{iI} is the wave vector.

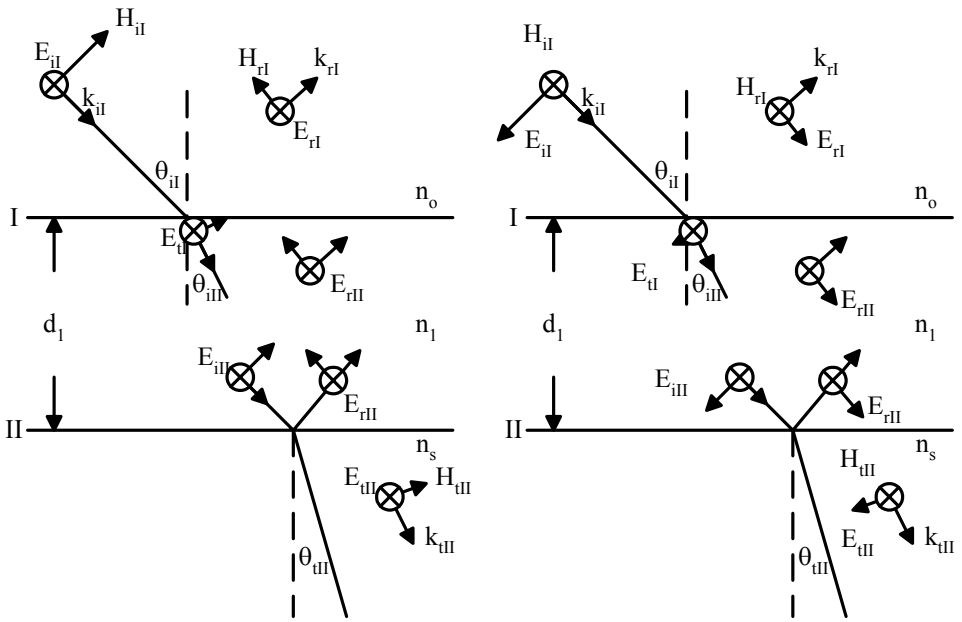

Fig. 2-1 Assumed electromagnetic fields at the boundaries of a thin film (a) E is perpendicular to the plane of incidence (b) E is parallel to the plane of incidence

The incident wave (E_i) splits into a reflected wave (E_r) and a transmitted wave (E_t) at the boundary. At boundary I, the amplitudes of the fields are expressed as E_{iI}, E_{rI}, and E_{tI}, and at boundary II, those are E_{iII}, E_{rII}, and E_{tII}. The incident angle is θ_{iI}, and the corresponding refractive angles at the film and output medium are θ_{iII} and θ_{iIII} as obtained by Snell's law, i.e.,

$$n_0 \sin\theta_{iI} = n_1 \sin\theta_{iII} = n_s \sin\theta_{iIII} \quad \text{.....(2.2)}$$

The boundary conditions of electromagnetic wave theory require the continuity of the tangential components of both the electric (E) and magnetic (H) field vectors across the boundaries. In this case, boundary I is defined by $z=z_0$, and the tangential components must be continuous for all values of x, y and t.

First, we discuss the field relations with the incident wave in the TE polarization, i.e. a wave with the electric vector normal to the plane of incidence (shown in Fig. 2-1 (a)). At the interface of $z=z_0$, we obtain

$$\begin{aligned} E_I &= E_{iI} + E_{rI} = E_{tI} + E'_{rII} \\ H_I &= Z_0(E_{iI} - E_{rI})n_0 \cos\theta_{iI} = Z_0(E_{tI} - E'_{rII})n_1 \cos\theta_{iII} \end{aligned} \quad \text{.....(2.3)}$$

where E'_{rII} is the reflected wave at boundary II propagating to boundary I, and $Z_0 = \sqrt{\frac{\varepsilon_0}{\mu_0}}$ with ε_0 and μ_0 being the permittivity and the permeability of vacuum.

Similarly, at the interface of $z=z_1$, we obtain

$$\begin{aligned} E_{II} &= E_{iII} + E_{rII} = E_{tII} \\ H_{II} &= Z_0(E_{iII} - E_{rII})n_1 \cos\theta_{iII} = Z_0 E_{tII} n_s \cos\theta_{iIII} \end{aligned} \quad \text{.....(2.4)}$$

A wave that propagates through the single layer of thickness d undergoes a phase shift of $2\pi\lambda^{-1}n_1d_1\cos\theta_{iII}$, which will be denoted by φ_1. Therefore,

$$\begin{aligned} E_{iII} &= E_{tI}e^{-i\varphi_1} \\ E'_{rII} &= E_{rII}e^{-i\varphi_1} \end{aligned} \quad \text{.....(2.5)}$$

By solving Eq. (2.3)-(2.5), the electric and magnetic fields at the input and the output of the single layer can be expressed in matrix notation,

$$\begin{bmatrix} E(z_0) \\ H(z_0) \end{bmatrix} = \begin{bmatrix} \cos\varphi_1 & i\sin\kappa_1 / Y_I \\ iY_I \sin\varphi_1 & \cos\varphi_1 \end{bmatrix} \begin{bmatrix} E(z_1) \\ H(z_1) \end{bmatrix} = M_I \begin{bmatrix} E(z_1) \\ H(z_1) \end{bmatrix} \quad \text{.....(2.6)}$$

$$\varphi_1 = 2\pi n_1 d_1 \cos\theta_{iII} / \lambda, \quad Y_I = Z_0 n_1 \cos\theta_{iII}$$

where the matrix M_I is called the characteristic matrix of the layer.,

For the TM polarization incidence wave, i.e., E-field parallel to the plane of incidence (shown in Fig. 2-1(b)), the same representation of the characteristic matrix in Eq. (2.6) is obtained except Y_I is replaced by $Z_0n_1\cos\theta_{iII}^{-1}$ with the same procedure.

2.2 Characteristic matrix of multiple layers

In the previous section, the characteristic matrix relates the fields at boundary I ($z=z_0$) to the fields at boundary II ($z=z_1$). As two over-layering films are deposited on the substrates, the characteristic matrix of film II could be expressed as

$$M_{II}=\begin{bmatrix}\cos\varphi_2 & (i\sin\varphi_2)/Y_{II}\\ iY_{II}\sin\varphi_2 & \cos\varphi_2\end{bmatrix} \quad \text{.....(2.7)}$$

where $\varphi_2=2\pi\lambda^{-1}n_2d_2\cos\theta_2$ and $Y_{II}= Z_0n_2\cos\theta_2$ for TE polarization and $Z_0n_2\cos\theta_2^{-1}$ for TM polarization with n_2 the refractive index, d_2 the thickness and θ_2 the refractive angle of the second film.

The relation between the fields at $z=z_1$ and $z=z_2$ is given by

$$\begin{bmatrix}E(z_1)\\ H(z_1)\end{bmatrix}=M_{II}\begin{bmatrix}E(z_2)\\ H(z_2)\end{bmatrix} \quad \text{.....(2.8)}$$

Multiplying both sides of Eq.(2.8) with M_I, we obtain

$$\begin{bmatrix}E(z_0)\\ H(z_0)\end{bmatrix}=M_IM_{II}\begin{bmatrix}E(z_2)\\ H(z_2)\end{bmatrix} \quad \text{.....(2.9)}$$

In general, if p is the number of layers, each with refractive index of n_i and thickness of d_i, then fields at the first ($z=z_0$) and the last layer ($z=z_p$) boundaries are related by

$$\begin{bmatrix}E(z_0)\\ H(z_0)\end{bmatrix}=M_IM_{II}M_{III}\cdots M_p\begin{bmatrix}E(z_p)\\ H(z_p)\end{bmatrix}=\begin{bmatrix}M_{11} & M_{12}\\ M_{21} & M_{22}\end{bmatrix}\begin{bmatrix}E(z_p)\\ H(z_p)\end{bmatrix} \quad \text{.....(2.10)}$$

2.3 Transfer matrix, reflectance, and transmittance

Next, we obtain the transmittance and the reflectance expressed by the elements of the characteristic matrix. The relations of the electromagnetic fields E and H to the positive- and negative-going wave E^+ and E^- are expressed as [2]

$$\begin{bmatrix} E \\ Z_0 H \end{bmatrix} = \begin{bmatrix} 1 & 1 \\ n & -n \end{bmatrix} \begin{bmatrix} E^+ \\ E^- \end{bmatrix} \quad \text{.....(2.11)}$$

Applying Eq. (2.11) to Eq. (2.10) of a p-layer thin film structure, we obtain

$$\begin{bmatrix} E^+(z_0) \\ E^-(z_0) \end{bmatrix} = \begin{bmatrix} 1 & 1 \\ n_0 & -n_0 \end{bmatrix}^{-1} \begin{bmatrix} M_{11} & M_{12} \\ M_{21} & M_{22} \end{bmatrix} \begin{bmatrix} 1 & 1 \\ n_s & -n_s \end{bmatrix} \begin{bmatrix} E^+(z_p) \\ E^-(z_p) \end{bmatrix} = \begin{bmatrix} S_{11} & S_{12} \\ S_{21} & S_{22} \end{bmatrix} \begin{bmatrix} E^+(z_p) \\ E^-(z_p) \end{bmatrix} \quad \text{.....(2.12)}$$

with
$$S_{11} = \frac{M_{11} + M_{21}/n_0 + n_s M_{12} + n_s M_{22}/n_0}{2}$$
$$S_{12} = \frac{M_{11} + M_{21}/n_0 - n_s M_{12} - n_s M_{22}/n_0}{2}$$
$$S_{21} = \frac{M_{11} - M_{21}/n_0 + n_s M_{12} - n_s M_{22}/n_0}{2}$$
$$S_{22} = \frac{M_{11} - M_{21}/n_0 - n_s M_{12} + n_s M_{22}/n_0}{2}$$

The S matrix is known as the transfer matrix, and can also be expressed with the reflection and transmission coefficients, i.e.

$$S = \begin{bmatrix} \frac{1}{t} & \frac{r^*}{t} \\ \frac{r}{t} & \frac{t^2 - r^* r}{t} \end{bmatrix} \quad \text{.....(2.13)}$$

where r and t are the reflection and transmission coefficients of the system, and * denotes the complex conjugate.

Therefore, the reflection coefficient r is

$$r = \frac{M_{11} - M_{21}/n_0 + n_s M_{12} - n_s M_{22}/n_0}{M_{11} + M_{21}/n_0 + n_s M_{12} + n_s M_{22}/n_0} \quad \text{.....(2.14)}$$

And the transmission coefficient t is

$$t = \frac{2}{M_{11} + M_{21}/n_0 + n_s M_{12} + n_s M_{22}/n_0} \quad \text{.....(2.15)}$$

The reflectance R and transmittance T are

$R = r \cdot r^*$ and $T = (n_s/n_0)\, t \cdot t^*$

In the subsequent sections, the properties of the periodic stack are overviewed using numeric examples.

2.4 Multilayer with periodic structure

A periodic multilayer usually consists of successive homogenous layers with alternately low and high refractive indices n_L and n_H of thickness d_L and d_H, respectively, placed between two homogenous media of refractive indices n_0 and n_s. The characteristic matrix M of a single period is given by [5]

$$\begin{bmatrix} \cos\varphi_H \cos\varphi_L - \frac{Y_L}{Y_H}\sin\varphi_H \sin\varphi_L & -i(\frac{1}{Y_L}\cos\varphi_H \sin\varphi_L + \frac{1}{Y_H}\sin\varphi_H \cos\varphi_L) \\ -i(Y_H \sin\varphi_H \cos\varphi_L + Y_L \cos\varphi_H \sin\varphi_L) & \cos\varphi_H \cos\varphi_L - \frac{Y_H}{Y_L}\sin\varphi_H \sin\varphi_L \end{bmatrix} \quad \text{.....(2.16)}$$

where $\varphi_H=2\pi\lambda^{-1}n_Hd_H\cos\theta_H$, $\varphi_L=2\pi\lambda^{-1}n_Ld_L\cos\theta_L$, $Y_H=Z_0n_H\cos\theta_H$ and $Y_L= Z_0n_L\cos\theta_L$ for TE incident polarization and $Y_H= Z_0n_H/\cos\theta_H$ and $Y_L= Z_0n_L/\cos\theta_L$ for TM polarization with refractive angles in the high- and low materials θ_H and θ_L respectively.

The characteristic matrix M^N of the periodic multilayer with N periods have been calculated using Chevyshev polynomials of the second kind, as [5]

$$M^N = \begin{bmatrix} m_{11}u_{N-1}(a) - u_{N-2}(a) & m_{12}u_{N-1}(a) \\ m_{21}u_{N-1}(a) & m_{22}u_{N-1}(a) - u_{N-2}(a) \end{bmatrix} \quad \text{.....(2.17)}$$

where m_{11}, m_{12}, m_{21} and m_{22} are the elements of the matrix M, $a=(m_{11}+m_{22})/2$, and $u_N(x)$ are Chebyshev polynomials defined as

$$u_N(x) = \frac{\sin\left[(N+1)\cos^{-1}x\right]}{\sqrt{1-x^2}} \quad \text{.....(2.18)}$$

The reflection and transmission coefficients are obtained by substituting the matrix elements into Eq (2.14).

The most famous and simplest periodic stack is the quarter-wave stack consisting of layers with the same optical thickness. The quarter-wave stack is designed for a

central wavelength λ_0 such that the optical thickness of each layer is $\lambda_0/4$, i.e. $n_L d_L = n_H d_H = \lambda_0/4$. The characteristic matrix M at λ_0 is

$$M = \begin{bmatrix} -\frac{n_H}{n_L} & 0 \\ 0 & -\frac{n_L}{n_H} \end{bmatrix} \quad \text{.....(2.19)}$$

and the characteristic matrix M^N of the multilayer with N periods is

$$M^N = \begin{bmatrix} (-\frac{n_H}{n_L})^N & 0 \\ 0 & (-\frac{n_L}{n_H})^N \end{bmatrix} \quad \text{.....(2.20)}$$

The reflectivity is given by

$$R_{2N} = \left(\frac{1 - \frac{n_s}{n_0} (\frac{n_L}{n_H})^{2N}}{1 + \frac{n_s}{n_0} (\frac{n_L}{n_H})^{2N}} \right)^2 \quad \text{.....(2.21)}$$

Eq (2.21) shows that R_{2N} increases (and approach 1 asymptotically) with the increase of the ratio n_H/n_L and with the increase in N

Fig. 2-2 shows the reflectivity spectrum of periodic stacks with different numbers of periods N. We use the parameters of n_H=3.374, n_L=1.5 and n_0=n_s=1. As expected, the periodic stack produces a high-reflection spectral region centered at λ_0. In addition, the reflectivity outside of the high-reflection region oscillates with wavelength. With the increase of N, the reflectivity increases and the spectral bandwidth of the high-reflectivity region becomes narrower.

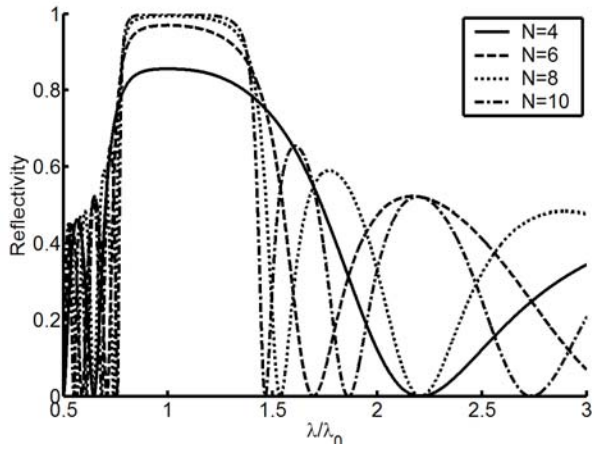

Fig. 2-2 Reflectance spectra of the quarter-wave stacks with different numbers of period

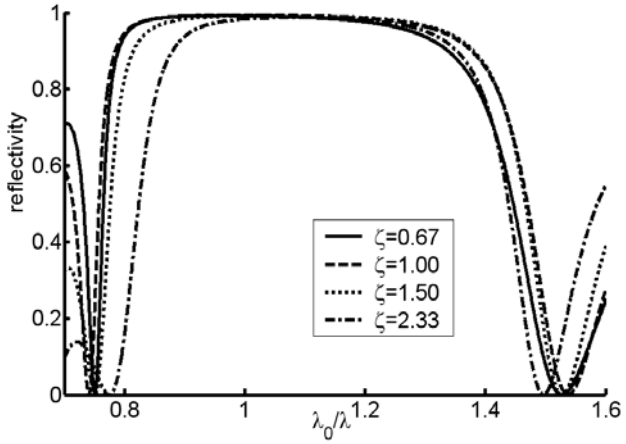

Fig. 2-3 Reflectivity of the periodic stacks with different optical thickness ratio ζ

We now examine the properties of a more general periodic stack, satisfying the condition $n_H d_H + n_L d_L = \lambda_0/2$ [6]. To analyze this generalized structure, we introduced a new parameter, ζ, defined as the ratio between $n_H d_H$ and $n_L d_L$. Fig. 2-3 shows the reflectivity spectra of a periodic stack with N=8 for various values of ζ. We see that the maximum reflectivity at λ_0 and the largest bandwidth are obtained as ζ=1.

2.5 Bidirectional eigenmode propagation (BEP) method for waveguide analysis

The bidirectional eigenmode propagation method is a simple yet powerful modeling technique for studying the propagation in waveguide components. In particular, this approach is useful for the design and the analysis of waveguide structures with large refractive index variations [7]-[9]. In principle, it integrates the advantages of a multimode transfer-matrix method for calculating the propagation of a set of forward and backward traveling eigenmodes with the accurate handling of Maxwell's boundary conditions by the mode-matching method.

With this approach, waveguide components are considered as a sequence of longitudinally invariant sections. The propagation constants and the mode distributions in each waveguide section are solved by Maxwell's equations. The optical field is determined by a superposition of the field distributions of forward and backward traveling eigenmodes, including all guided modes and a set of discrete radiation modes. For each section, the modal distribution is obtained by introducing boundary conditions on the edge of the analysis window. At an interface between different sections the redistribution of each mode in each section is determined by coupling coefficients between the eigenmodes of the both sections calculated by the overlap integral between the modes of these two sections and the continuity of boundary conditions for each polarization. The field variation in each section is obtained by multiplying the amount of the redistribution at the interface and the phase shift inside each section.

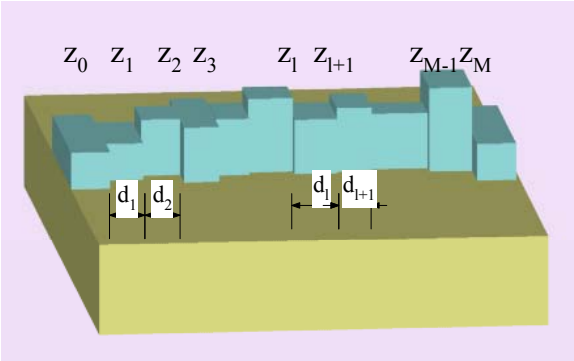

Fig. 2-4 The schematic structure of the waveguide sections

The generalized waveguide structure with M sections is shown schematically in Fig. 2-4. The analysis is focused on the quasi-TE polarized wave, and the derivation for the TM polarized wave can be obtained with similar procedures. The electric and magnetic fields in section l are expressed as a superposition of N eigenmodes with the bidirectional propagation in the z direction

$$
\begin{aligned}
{}^{l}E_x(x,y,z) &= \sum_{i=1}^{N} {}^{l}f_i(x,y)\left({}^{l}A_i e^{-j\,{}^{l}k_{z,i}(z-z_{l-1})} + {}^{l}B_i e^{j\,{}^{l}k_{z,i}(z-z_{l-1})}\right) \\
{}^{l}H_y(x,y,z) &= \sum_{i=1}^{N} {}^{l}f_i(x,y)\frac{{}^{l}k_{z,i}}{\omega\mu}\left({}^{l}A_i e^{-j\,{}^{l}k_{z,i}(z-z_{l-1})} - {}^{l}B_i e^{j\,{}^{l}k_{z,i}(z-z_{l-1})}\right)
\end{aligned}
\qquad \text{.....(2.22)}
$$

where ${}^{l}f_i(x,y)$ are the i-th eigenmode distribution, ${}^{l}k_{z,I}$ are the wave vectors, and ${}^{l}A_i$ and ${}^{l}B_i$ denote the amplitudes for the i-th forward and backward traveling modes, and the coordinate z_{l-1} marks the interface of l-1 and l sections.

At the interface between section l and l+1 the tangential components of the electric and the magnetic fields need to be continuous, giving

$$
\begin{aligned}
{}^{l}E_x(x,y,z=z_l) &= {}^{l+1}E_x(x,y,z=z_l) \\
{}^{l}H_y(x,y,z=z_l) &= {}^{l+1}H_y(x,y,z=z_l)
\end{aligned}
\qquad \text{.....(2.23)}
$$

We also make use of the orthogonality of the modes, given by

$$\iint \frac{1}{n_l^v(x,y)} {}^{l}f_i(x,y)\,{}^{l}f_j(x,y)dxdy = \delta_{i,j} \quad \text{.....(2.24)}$$

where $n_l(x,y)$ is the refractive-index distribution in the section l, $\delta_{i,j}$ is a Dirac delta function, and v = 0 for the TE polarized wave and 2 for the TM polarized wave.

The relation between amplitudes $\{{}^{l}A, {}^{l}B\}$ and $\{{}^{l+1}A, {}^{l+1}B\}$ is denoted as a matrix of ${}^{l}P$

$$\begin{bmatrix} {}^{l}A \\ {}^{l}B \end{bmatrix} = \begin{bmatrix} e^{j\,{}^{l}k_z d_l} & 0 \\ 0 & e^{-j\,{}^{l}k_z d_l} \end{bmatrix} \begin{bmatrix} \frac{1}{2}g(1+\frac{{}^{l+1}k_z}{{}^{l}k_z}) & \frac{1}{2}g(1-\frac{{}^{l+1}k_z}{{}^{l}k_z}) \\ \frac{1}{2}g(1-\frac{{}^{l+1}k_z}{{}^{l}k_z}) & \frac{1}{2}g(1+\frac{{}^{l+1}k_z}{{}^{l}k_z}) \end{bmatrix} \begin{bmatrix} {}^{l+1}A \\ {}^{l+1}B \end{bmatrix} = {}^{l}P \begin{bmatrix} {}^{l+1}A \\ {}^{l+1}B \end{bmatrix} \quad \text{.....(2.25)}$$

where $d_l = z_l - z_{l-1}$, where *g* is the overlap integrals defined as

$${}^{l,l+1}g_{i,j} = \iint \frac{1}{n_l^v(x,y)} {}^{l}f_i(x,y)\,{}^{l+1}f_j(x,y)dxdy \quad \text{.....(2.26)}$$

As the entire structure consists of M sections, the total transfer matrix is represented as

$$P = \prod_{i=1}^{M} {}^{l}P = \begin{bmatrix} P_{11} & P_{12} \\ P_{21} & P_{22} \end{bmatrix} \quad \text{.....(2.27)}$$

The amplitudes of transmitted ${}^{M}A$ and reflected ${}^{0}B$ waves are obtained by setting ${}^{M}B=0$, resulting in

$$\begin{aligned} {}^{M}A &= P_{11}^{-1}\,{}^{0}A \\ {}^{0}B &= P_{21}P_{11}^{-1}\,{}^{0}A \end{aligned} \quad \text{.....(2.28)}$$

In contrast to the transfer matrix method, this approach takes into account the transverse field redistribution in each section, and the coupling between various modes at the boundary, including coupling to radiative modes that reduces the output power

References

[1] H. A Macleod, *Thin-film optical filters*, 3rd ed. (Philadelphia, Institute of Physics Pub., 2001).

[2] A. Thelen, *Design of optical interference coatings*, p. 20 (New York, McGraw-Hill, 1989).

[3] E. Delano, R. Pegis, "Methods of synthesis for dielectric multilayer filters**,"** *Progress in optics*, vol. VII, p.69-135 (North Holland., 1969)

[4] E. Hecht, *Optics*, 3rd ed. (Mass, Addison-Wesley, 1998)

[5] M. Born and E. Wolf, *Principles of optics*: *electromagnetic theory of propagation, interference and diffraction of light*, 7th ed. (New York, Cambridge University Press, 1999)

[6] Baumeister P, "chapter 20 Applications of Thin film coatings," *Military Standardization handbook: optical design* (Washington, Defense Supply Agency, 1962)

[7] G Sztefka, HP Nolting,"Bidirecitonal eigenmode propation for large refractive-index step," IEEE Photon Technol Lett. 5 (5), 554-557 (1993)

[8] J Ctyroky, S Helfert, R Pregla, "Analysis of a deep waveguide Bragg grating," Opt. & Quantum electron 30 (5-6), 343-358 (1998)

[9] J. Willems, J Haes, R. Baets, "The bidirectional mode expansion method fro two-dimensional waveguides: the TM case," Opt. & Quantum Electron 27 (10), 995-1007 (1995)

Chapter 3 Synthesis and Design of Dielectric Square Bandpass Filter Using Anomalous Dispersion Mirrors

In this chapter, we extend the analysis of Smith's method [1] dealing with a multiple-cavity filter as a Fabry-Perot resonator (i.e. a cavity with two frequency-dependent reflectors). We develop a novel technique to implement a flat-top bandpass filter by designing these frequency-dependent mirrors, rather than finding the reflectivity of each reflector and the thickness of each cavity as most of the thin-film filter design methods have done. In Section 3.1 we briefly describe the Smith's method, and mathematically find the optimized conditions to achieve flat-top and nearly unity transmission passband on the basis of the definition of a maximally flat filter with this model. A specific mirror with anomalous dispersion (AD) is required to achieve a maximally flat filter. This type of mirrors is coined "AD mirror". Section 3.2 describes an approach to construct AD mirrors by using multiple-cavity resonators and shows how the bandwidth of an AD-mirror based bandpass filter is related to the width of the AD region. Section 3.3 provides a design procedure to realize a flat-top AD mirrors-based bandpass filter. Section 3.4 presents an example to demonstrate the usefulness of the design strategy and Section 3.5 summarizes the chapter.

3.1 Theory

A. Smith's method

Consider two cascaded non-absorbing multilayer structures A and B separated by a cavity C with thickness d and refractive index n as shown in Fig. 3-1. Suppose that the refractive indices of the input and output media are n_0 and n_s, respectively. Let system A

include all layers from the input medium to the left interface of C and system B consist of all layers from the right interface of C to output medium. Based on the transfer matrix approach (Eq. (2.13)), the relationships between the forward and backward propagating waves in the media outside of system A and B can be expressed as

$$\begin{bmatrix} E_{A+}(z_0) \\ E_{A-}(z_0) \end{bmatrix} = \begin{bmatrix} \frac{1}{t_A} & -\frac{r_A^*}{t_A^*} \\ \frac{r_A}{t_A} & \frac{1}{t_A^*} \end{bmatrix} \begin{bmatrix} E_{A+}(z_m) \\ E_{A-}(z_m) \end{bmatrix} \quad \text{.....(3.1)}$$

$$\begin{bmatrix} E_{B+}(z_{m+1}) \\ E_{B-}(z_{m+1}) \end{bmatrix} = \begin{bmatrix} \frac{1}{t_B} & -\frac{r_B^*}{t_B^*} \\ \frac{r_B}{t_B} & \frac{1}{t_B^*} \end{bmatrix} \begin{bmatrix} E_{B+}(z_N) \\ E_{B-}(z_N) \end{bmatrix} \quad \text{.....(3.2)}$$

where t_A, r_A are transmission and reflection coefficients of system A, and t_B, r_B are those of system B. * denotes the complex conjugate.

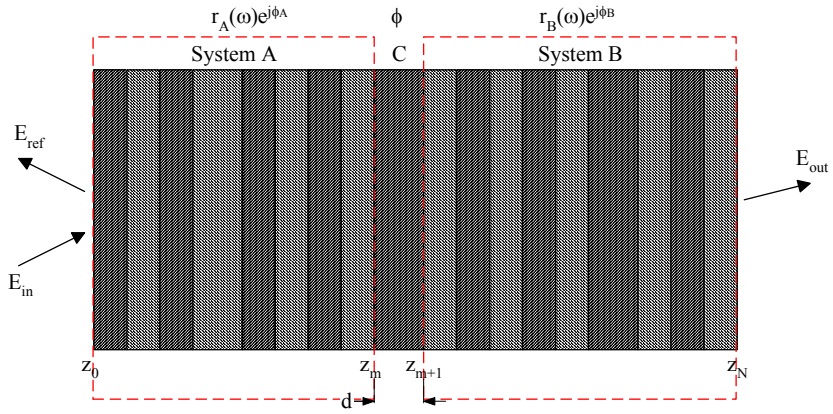

Fig. 3-1 The schematic structure of the filter with the effective interfaces in Smith's method

In film C, the propagating fields experience a phase shift $\phi=\omega c^{-1}ndcos\theta$, where θ is the refractive angle, ω is the frequency of incident wave, and c is light speed, $3x10^8$m/sec. The propagation matrix is

$$\begin{bmatrix} E_{A+}(z_m) \\ E_{A-}(z_m) \end{bmatrix} = \begin{bmatrix} e^{i\phi} & 0 \\ 0 & e^{-i\phi} \end{bmatrix} \begin{bmatrix} E_{B+}(z_{m+1}) \\ E_{B-}(z_{m+1}) \end{bmatrix} \quad \text{.....(3.3)}$$

The overall transfer matrix of the entire structure is calculated by multiplying Eqs. (3.1)-(3.3),

$$\begin{bmatrix} \frac{1}{t_A} & -\frac{r_A^*}{t_A^*} \\ \frac{r_A}{t_A} & \frac{1}{t_A^*} \end{bmatrix} \begin{bmatrix} e^{i\phi} & 0 \\ 0 & e^{-i\phi} \end{bmatrix} \begin{bmatrix} \frac{1}{t_B} & -\frac{r_B^*}{t_B^*} \\ \frac{r_B}{t_B} & \frac{1}{t_B^*} \end{bmatrix} \quad \text{.....(3.4)}$$

Transmission and reflection coefficients are given by

$$t = \frac{t_A t_B e^{-j\phi}}{1 - r_A r_B e^{-2j\phi}} \quad \text{.....(3.5)}$$

$$r = \frac{r_A + r_B e^{-2j\phi}}{1 - r_A r_B e^{-2j\phi}} \quad \text{.....(3.6)}$$

Assuming a lossless structure, the transmittance can be expressed as

$$T = \frac{(1 - R_A)(1 - R_B)}{1 + R_A R_B - 2\sqrt{R_A R_B}\cos\Phi(\omega)} \quad \text{.....(3.7)}$$

where R_A and R_B are the reflectances of systems A and B respectively, $\Phi=2\phi-\phi_A-\phi_B$ with reflection phases of systems A and B being ϕ_A and ϕ_B, respectively.

B. Conditions for flat-top passband

We define the multilayer structure as a maximally flat bandpass filter of N^{th}-order if the first (2N-1) derivatives of transmittance at the frequency ω_0 are all zero, i.e. $d^nT/d\omega^n=0$, n=1… (2N-1)[2]. We first consider a first-order filter, i.e. $dT/d\omega=0$. By deriving Eq. (3.7) we find the conditions for minimum and for maximum of transmittance. Obviously, the later is our goal. As $R_A(\omega_0)=R_B(\omega_0)$ and $\Phi(\omega_0)=2m\pi$, m is an integer, transmittance $T_{max}(\omega_0)=1$. These conditions implicitly indicate that completely constructive interference occurs at ω_0.

Next we require $d^2T/d\omega^2=0$ from which we obtain $d\Phi/d\omega=0$ and $dR_A(\omega_0)/d\omega-dR_B(\omega_0)/d\omega=0$. With a similar procedure, by requiring $d^nT/d\omega^n=0$, n=1, 2… (2N-1), we obtained the conditions $d^n\Phi/d\omega^n=0$, $d^nR_A(\omega_0)/d\omega^n-d^nR_B(\omega_0)/d\omega^n=0$, n=1…N, $R_A(\omega_0)=R_B(\omega_0)$, and $\Phi=2m\pi$. Based on the aforementioned conditions, we see that to achieve higher order flatness, not only do these two mirrors have similar reflection spectra, but also the total phase Φ is independent of frequency, i.e. $\Phi\approx2m\pi$ for the entire passband. In other words, a wave with its frequency within the passband must be in-phase inside the cavity C.

The total phase shift Φ consists of the round-trip phase shift inside the cavity, $\phi=\omega c^{-1}ndcos\theta$, and the reflectance phases ϕ_A and ϕ_B. Since ϕ is a linearly increasing function of frequency, either ϕ_A or ϕ_B has to be an increasing function of frequency to compensate for the phase shift ϕ caused by the cavity, i.e. $d(\phi_A+\phi_B)/d\omega$ at $\omega_0=2c^{-1}ndcos\theta$. In addition, as $\phi_A+\phi_B$ has zero value of higher-order dispersion, the flatness order of the bandpass filter increases. Such a mirror possessing an increasing function of frequency in the reflection phase region is called an anomalous dispersion (AD) mirror [3].

3.2 Implementation of anomalous dispersion (AD) mirrors

A periodic stack with two alternating different materials possesses a high-reflection region obtained around a central wavelength that meets the Bragg condition, i.e. $n_Hd_H+n_Ld_L=\lambda_o/2$. The reflectance phase ϕ of this stack in its high-reflection region is a monotonically decreasing function of frequency, i.e. $d\phi/d\omega<0$. For example, a periodic

quarter-wave stack with a large numbers of periods has the reflectance phase in this region approximately equal to [4]-[5],

$$\pi\left(1-\frac{n_0}{n_H-n_L}\frac{\omega-\omega_o}{\omega}\right) \quad \text{.....(3.8)}$$

for $|\omega-\omega_0|<<\omega_0$, and $\omega_0=2\pi c\lambda_0^{-1}$. As seen in Eq. (3.8), the derivative of reflectance phase at ω_0 is negative, which is undesirable for flat-top filter designs. Instead, a positive value of the derivative of the reflectance phase at ω_0 is a requisite.

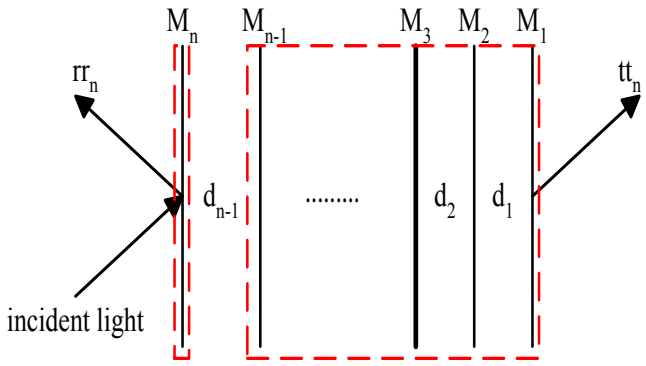

Fig. 3-2 The multiple-cavity structure of the proposed AD mirror

Based on the Kramers–Kronig relations, the reflection spectrum of a mirror with a anomalous dispersion region of reflection phase approximately resembles a parabola with a positive parabolic curvature in that region. A possible approach to implement a mirror with such a profile is to use dielectric resonant mirrors (or the periodic stacks with defects). For example, we can use a mirror consisting of $H(LH)^PL_1(HL)^qH$ with the condition p>q, where H (L) is the quarter-wave layer of high (low) refractive index [3]-[4]. A resonant mirror comprised of N reflectors and N-1 cavities is shown in Fig. 3-2. Suppose that the reflectors consist of periodic stacks or metallic mirrors, i.e. the reflection phase slopes are non-positive. The amplitude and the phase of the reflection coefficient of the j-th reflector M_j are r_j and ϕ_{Mj}, respectively. The phase shift caused by the j^{th}

cavity C_j is defined as ϕ_j, equal to $\omega c^{-1} n_j d_j \cos\theta_j$ with thickness d_j, refractive index n_j and the refractive angle θ_j. Analyzed by Smith's method with the reflector M_N as System A and the structure of $M_{N-1}C_{N-2}\ldots M_2C_1M_1$ as System B sandwiching the cavity C_{N-1}, the reflection coefficient of the entire structure can be expressed as

$$rr_N e^{j\Gamma_N} = e^{i\phi_{M_N}} \frac{r_N - rr_{N-1} e^{-i(2\phi_{N-1} - \phi_{M_N} - \Gamma_{N-1})}}{1 - rr_{N-1} r_N e^{-i(2\phi_{N-1} - \phi_{M_N} - \Gamma_{N-1})}} \quad \text{.....(3.9)}$$

where rr_{N-1} and Γ_{N-1} are the amplitude and the phase of the reflection coefficient of System B.

The amplitude and the phase of the reflection coefficient of the entire system are

$$rr_N = \sqrt{\frac{r_N^2 + rr_{N-1}^2 - 2r_N rr_{N-1}\cos\Phi_{N-1}}{1 + r_N^2 rr_{N-1}^2 - 2r_N rr_{N-1}\cos\Phi_{N-1}}}$$

$$\Gamma_N = \phi_{M_N} + \tan^{-1}\frac{rr_{N-1}\sin\Phi_N}{r_N - rr_{N-1}\cos\Phi_N} - \tan^{-1}\frac{r_N rr_{N-1}\sin\Phi_N}{1 - r_N rr_{N-1}\cos\Phi_N} \quad \text{.....(3.10)}$$

where Φ_{N-1} is the total phase shift caused by the reflection phase of the mirror M_N, that of System B and the thickness of cavity C_{N-1}, equal to $2\phi_{N-1}$-ϕ_{MN}-Γ_{N-1}.

A local minimum of this resonant mirror occurs at $\Phi_N = 2m\pi$. The slope of reflection phase at this point is

$$\frac{d\Gamma_N}{d\omega} = \left[\frac{rr_{N-1}(1 - r_N^2)}{(1 - r_N rr_{N-1})(r_N - rr_{N-1})}\frac{d\Phi_{N-1}}{d\omega} + \frac{d\phi_{M_N}}{d\omega}\right] \quad \text{.....(3.11)}$$

Because the mirror M_N is either dielectric or metallic, i.e. $d\phi_M N/d\omega < 0$, the sign of $d\Gamma_N/d\omega$ is determined by the sign of the product of $(rr_{N-1}\text{-}r_N)$ and $d\Phi_{N-1}/d\omega$. In the next sub-sections, we systematically analyze the resonant mirrors with different numbers of

defects to realize the AD mirrors and synthetically present the dielectric AD mirrors constructed by using materials of SiO_2 (n=1.465) and Ta_2O_5 (n=2.065).

A. One-defect resonant mirror

One of the simplest structures for realizing AD mirrors is obtained by using two reflectors M_1 and M_2 sandwiching the cavity C_1. Because M_1 and M_2 are either periodic stacks or metallic mirrors, the total phase shift $\Phi_1=2\phi_1-\phi_{M1}-\phi_{M2}$ is a monotonically increasing function of ω, i.e. $d\Phi_1/d\omega>0$. In order to achieve a positive value of $d\Gamma_2/d\omega$, (r_2-r_1) has to be positive. In other words, an AD region is realized, as the reflectivity of M_1 is smaller than that of M_2.

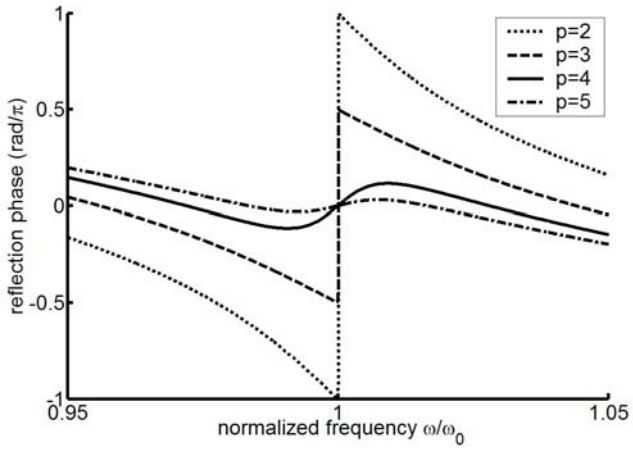

Fig. 3-3 Reflection phase of one-defect mirror with different values of p. The structure of the resonant mirror is $L(HL)^p2H(LH)^qL$ with q=3.

A one-defect dielectric resonant mirror is represented as $L(HL)^pC_1(LH)^qL$, where p and q are integers, H (L) is quarter-wave optical thickness of $Ta_2O_5(SiO_2)$. Suppose that the incident and output media are air. Reflection phases of the mirrors with different relations between r_1 and r_2, obtained by varying the values of p, are shown in Fig. 3-3. Reflection phase is a monotonically increasing function of ω in the cases of $r_1 \geq r_2$. In the

cases of $r_1<r_2$, an AD region is obtained around the center frequency ω_0, which is the operation region for the flat-top passband. In addition, the slope of reflection phase at the center frequency and the width of the AD region decrease with the increase of the values of p. In other words, the width of AD region and the reflection phase slope are both decreased as a result of the increase of the reflectivity of M_2.

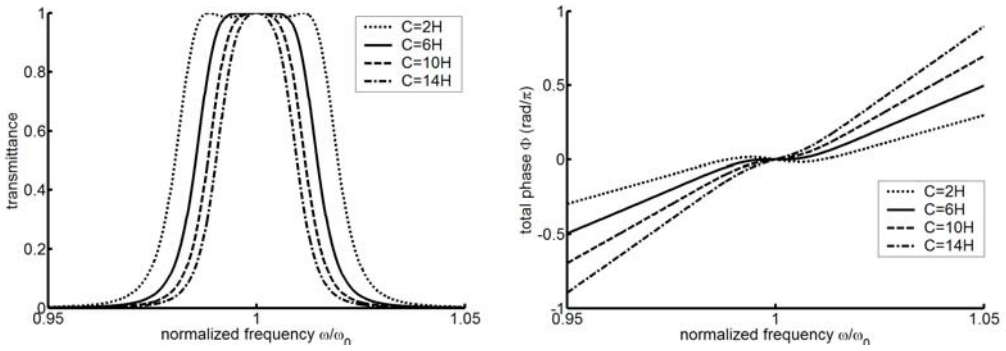

(a) (b)

Fig. 3-4 (a)Transmittance and (b) the total phase shift Φ of bandpass filter design by using two of identical AD mirror with variations of the thickness of the cavity C. The structure of the filter is $L(HL)^3 2H(LH)^5 LCL(HL)^5 2H(LH)^3 L$.

Fig. 3-4(a) shows the transmittance of the filter with different thicknesses of the cavity C by using the two aforementioned AD mirrors. The structure is $L(HL)^3 2H(LH)^5 LCL(HL)^5 2H(LH)^3 L$. The bandwidth of the filter becomes narrower, as the thickness of C increases. The flat-top passband is obtained for C=6H, corresponding to $d\Phi/d\omega=0$ at ω_0 as depicted in Fig. 3-4(b). In the case of $d\Phi/d\omega<0$ at ω_0, ripples in the passband are generated, and the local maximum occurs at wavelengths where the total phase shift is $\Phi=2m\pi$. For $d\Phi/d\omega>0$ at ω_0, the passband tends to become rounder, and the bandwidth becomes narrower as $d\Phi/d\omega$ at ω_0 increases.

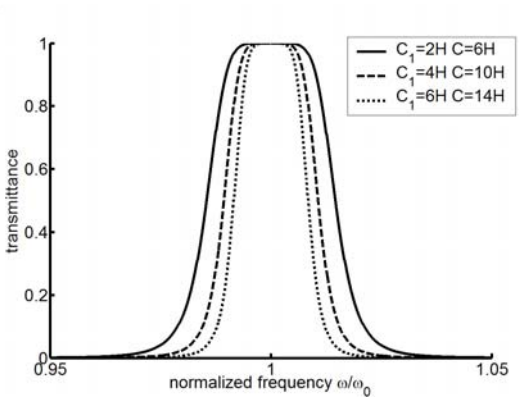

Fig. 3-5 Transmittance of flat-top bandpass filter with variations of the thickness of defect in the one-defect AD mirrors. The structure of the filter is $L(HL)^3C_1(LH)^5LCL(HL)^5C_1(LH)^3L$.

As a criterion for comparison, we define that the flat bandwidth as the spectral width at which the transmittance level is -0.5dB below the peak value. Fig. 3-5 shows flat-top bandpass filter designs of the structure $L(HL)^3C_1(LH)^5LCL(HL)^5C_1(LH)^3L$ for various values of defect C_1 thickness . Thickness of C is chosen to meet the condition of $d\Phi/d\omega \approx 0$. We see that the bandwidth of the filter decreases as C_1 increases. The widths of normalized flat spectral region are 0.021, 0.015, and 0.012 as with thickness of C_1 being 2H, 6H, and 10H respectively. Additionally, the corresponding widths of the AD region are measured as 0.015, 0.013, and 0.011 respectively. We learn that the width of the AD regions are slightly smaller than that of the flatness bandwidth and reduces with increasing C_1. Thus we can control the flatness bandwidth of a filter by changing the thickness of the defects.

To summarize, an AD mirror can be realized by a one-defect resonant mirror as long as the reflectivity of M_2 is larger than that of M_1. In addition, the flatness bandwidth of the filter using two AD mirrors is determined by the width of the AD region of these mirrors. The width of the AD region is controlled by the reflectivities of the two mirrors M_2 and M_1 and the thickness of the defect C_1.

B. Two or more-defect resonant mirror

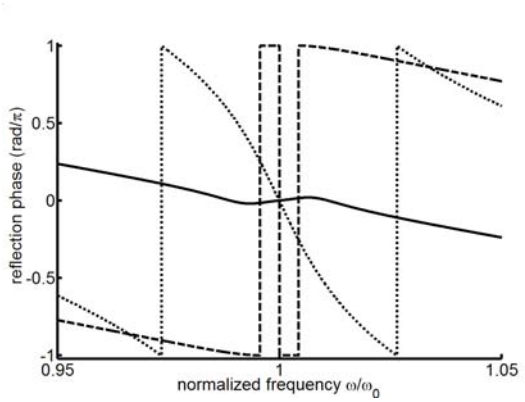

Fig. 3-6 Reflection phase of a two-defect resonant mirror of the structure $L(HL)^sC_2L(HL)^pC_1(LH)^qL$ with different relations between mirrors and defect thickness. The dotted line corresponds to s=0, p=3, q=5, C_1=2H and C_2=2H, the dashed line corresponds to s=0, p=5, q=3, C_1=2H, and C_2=2H, and the solid line corresponds of s=6, p=5, q=3, C_1=2H, and C_2=8H.

A two-defect dielectric resonant mirror has a structure of $L(HL)^sC_2L(HL)^pC_1(LH)^qL$, where s, p and q are integers. Fig. 3-6 shows the reflection phase of the mirror with relations between the one-defect mirror and the defect thickness of C_2. First, in the case of $r_2<r_1$ shown as the dotted line of Fig. 3-6, rr_2 is negative and $d\Gamma_1/d\omega<0$. Referring to Eq. (3.11), it is impossible to obtain an AD region by varying the thickness of defect C_2 and reflectivity of M_3. .

In the case of $r_2>r_1$, $\Gamma_1/d\omega>0$. $\Phi_2=2\phi-\phi_{M3}-\Gamma_1$. Based on different relations between r_3 and rr_2, there are two possible ways to achieve $d\Gamma_2/d\omega>0$; one is $d(2\phi-\phi_{M3})/d\omega<d\Gamma_1/d\omega$ and $r_3(\omega_0)<rr_2(\omega_0)$, and the other is $d(2\phi-\phi_{M3})/d\omega>d\Gamma_1/d\omega$ and $r_3(\omega_0)<rr_2(\omega_0)$. The dashed and solid lines of Fig. 3-6 depict the results under these two conditions. As shown AD regions are obtained for these two cases. Reflection phase spectrum in the former shifts to π and that in the latter is similar to the case of a one-defect mirror. Based on these two types of AD mirrors we simulate a flat-top bandpass

filter satisfying the condition of $d\Phi/d\omega=0$. The corresponding results are shown in Fig. 3-7. We find that the filter implemented by the former type of mirrors has wider bandwidth than that implemented by the latter type of mirror, but approximately the same as that of the filter using one-defeat resonant mirrors. In addition, the filter obtained by using the latter mirror provides a steeper transition band than the others. The flat bandwidths of the two filters are 0.020 and 0.016 and the bandwidths of these two AD mirrors are 0.005 and 0.013 respectively. Like the case of on-defect mirror, the flatness width is slightly larger than the width of AD region.

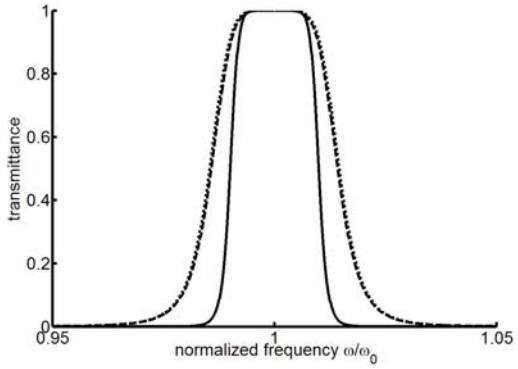

Fig. 3-7 Transmittance of a bandpass filter design by use of two-defect AD mirrors. The structure of the filter is $L(HL)^qC_1L(HL)^pC_2(LH)^sLCL(HL)^sC_2L(HL)^pC_1(LH)^qL$, and the dashed line is the case of q=3, p=5, s=1,and $C_1=C_2=C=2H$, and the solid line is the case of q=3, p=5, s=6, $C_1=2H$, $C_2=8H$, and C=6H. The dotted line is the filter by using one-defect AD mirrors with the structure $L(HL)^32H(LH)^5L6HL(HL)^52H(LH)^3L$

To summarize, we conclude that an AD mirror implemented with a multiple-defect resonant mirror can be analyzed as a defect sandwiched by one reflector and one resonant mirror. To obtain an AD mirror, the resonant mirror should also be an AD mirror if it is constructed by multiple-defect structure. In addition, to steepen the roll-off and to reduce the transmission in the stop band, the reflectivity of the reflector next to the input medium at the center frequency has to be larger than that of the resonant mirror,

and the thickness of defect has to be thick enough to compensate for the phase slope resulting from the resonant mirror. The flat bandwidth region of the filter is determined by the width of the AD region in the mirrors.

3.3 Design procedure

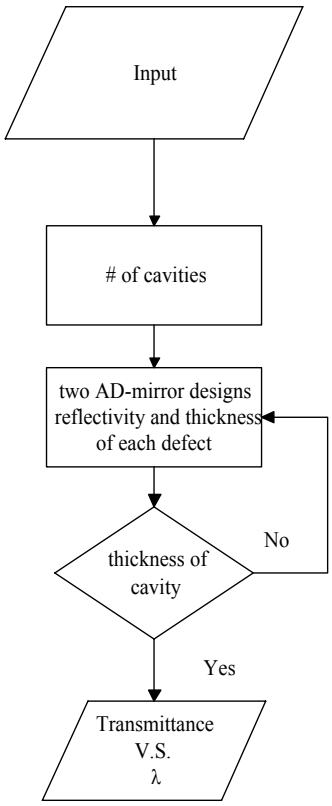

Fig. 3-8 Block diagram of the design procedure to implement a flat-top bandpass filter

Based on the above study and aiming for a bandpass filter with the criteria of (1) -3-dB bandpass bandwidth (2) a flat passband and (3) the bandwidth of the stopband, we apply a design procedure as summarized in Fig. 3-8. The inputs are the desired bandpass filter specifications and the materials for the design. The first step is to determine the number of cavities in the entire structure. Based on the equation of maximally flat

definition, the transmission spectrum of an N^{th} order flatness filter can be described approximately as [2]

$$T = \frac{1}{1+\left(\frac{\omega-\omega_0}{\omega_c-\omega_0}\right)^{2N}} \quad \text{.....(3.12)}$$

With the desired spectrum of the filter in hand, we can now calculate the minimal number of cavities to achieve the desired goal. The second step is to determine the number of defects for each AD mirror and design each AD mirror with the width of the AD region slightly less than the flatness bandwidth. The third step is to combine two designed AD mirrors face-to-face sandwiching the cavity C. Thickness of C is determined to compensate for the phase slope caused by these two AD mirrors. Finally, we adjust the defects or the reflectivity of the AD mirror iteratively until the desired transmission spectrum is obtained.

3.4 Design example

Here we show an example of the bandpass filter design for the application of a WDM system with the specifications as follows. (1) The center wavelength of the filter is 1500 nm. (2) The transmittance wave exceeds -0.5 dB in the wavelength region between 1549.89 and 1550.11 nm. (3) The full spectral width of the passband at the -3-dB transmittance level should not be larger than 0.3 nm. (4) The spectral width at the -20-dB transmittance level should not exceed 0.6 nm. Given is an incident medium of air, a substrate with a refractive index of 1.52, and two nonabsorbing coating material with refractive indices of 1.465 (L) and 2.065 (H). We assume that the rear side of the substrate is coated with a nonabsorbing zero-reflectance antireflection coating.

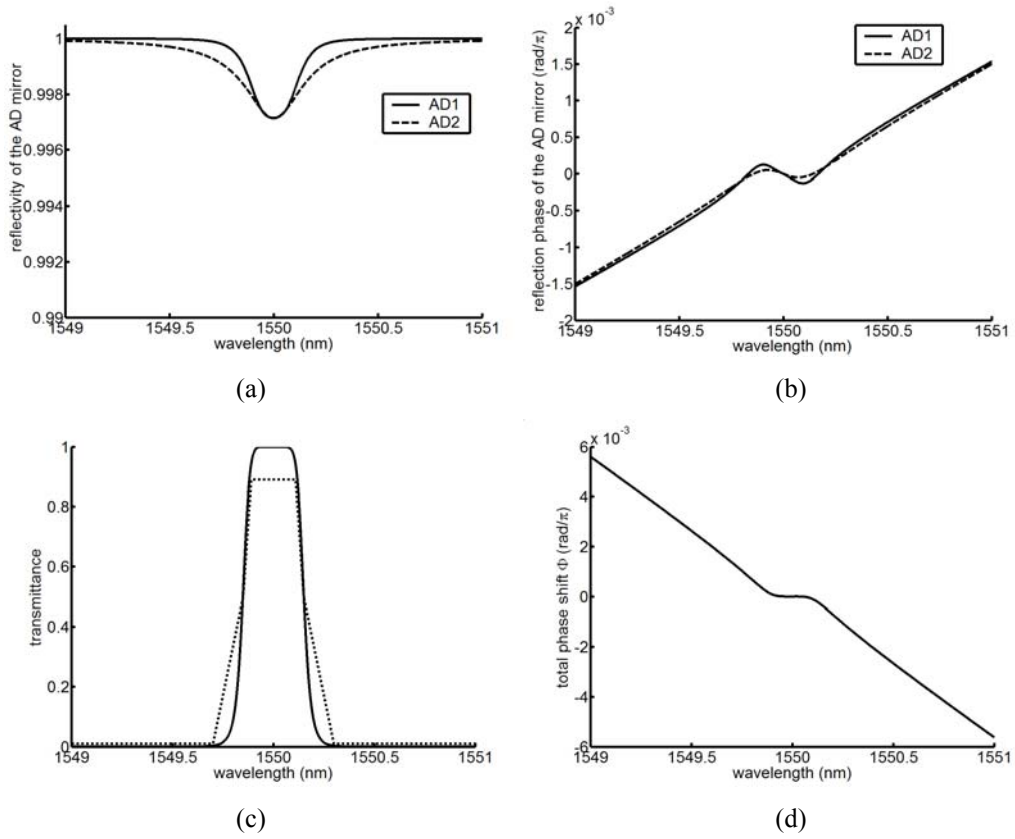

Fig. 3-9 An example of the bandpass filter design (a)Reflectivities of the designed AD mirrors. The solid line is the AD mirror next to the substrate and the dashed is that next to the air. (b) Reflection phase of the designed AD mirrors. (c) The final design of the bandpass filter with the structure of $0.66L1.65HL(HL)^{9}4HL(HL)^{19}4HL(HL)^{20}4HL(HL)^{19}2HL(HL)^{9}$. The dotted line represents the requirements of the desired filter. (d) The total phase shift Φ of the design.

Using Eq. (3.12), the minimal number of cavities to accomplish these requirements is 4. Subsequently, one AD mirror is designed as a two-defect resonant mirror and the other is a one-defect resonant mirror. First, we design a two-defect AD mirror next to the substrate. The entire structure of the AD mirror is now $L(HL)^{p}C_1L(HL)^{q}C_2L(HL)^{s}$ with integers p, q, and s, and multiple half-wave thicknesses of C_1, and C_2. We successively determine these values to achieve the width of the AD region ~0.19 nm to be slightly smaller than the flat bandwidth. p, q and s are 9, 19 and

20, respectively. C_1 and C_2 are 2H and 4H, respectively. The reflection spectrum and the reflection phase are shown as solid lines in Fig. 3-9(a)-(b).

Next, we determine the other AD mirror next to the air side with the structure $L(HL)^{p'}C_1{\cdot}L(HL)^{q'}$. Due to difference between the input and the output media, we choose q'=19, and the reflectivity and reflection phase of $L(HL)^{p'}$ has to be 0.993916 and 0 at the center wavelength in order to obtain the maximum transmittance with the conditions of $R_1(\lambda_0)=R_2(\lambda_0)$ and $\Phi(\lambda_0)=2m\pi$. Unfortunately, the reflectivities of the quarter-wave stack with p'=9 and 10 are 0.9914 and 0.9957, respectively. Consequently we need to add non-quarter-wave layers in order to obtain a reflectivity of 0.993916. A 21-layer reflector with the structure of $L_1H_1L(HL)^9$ is chosen and the thickness of L_1 and H_1 are numerically decided as 0.66L and 1.65H to have the mirror with R(1550) of 0.993916 and reflection phase of 0. The reflection spectrum and reflection phase of this AD mirror with $C_{1'}$=4H with the AD width of 14.45 nm are depicted as dashed lines in Fig. 3-9 (a)-(b).

The last step is to determine the cavity length C of this bandpass filter to achieve approximately constant Φ in the passband as shown in Fig. 3-9(d). The transmittance spectrum of the entire structure design is shown in Fig. 3-9(c) with the thickness of the cavity C=4H. The calculated flatness bandwidth is 0.237 nm, the 3-dB bandwidth is 0.302 nm and –20dB bandwidth is 0.526 nm. This presented design is aiming to match the requirement of –3dB bandwidth while maximizing the width of flatness and narrowing the width of –20 dB bandwidth.

3.5 Summary

We have presented a systematic approach to calculate the optimized conditions to achieve a maximally flat bandpass filter of multiple-cavity type. We found that frequency-dependent mirrors with an anomalous dispersion region in reflection phases play an important role in the implementation of a filter with a ripple-free passband. A method to design these AD mirrors is provided by using multiple-defect resonant mirrors and an algorithm to construct a flat-top dielectric bandpass filter with specifications is developed by realizing two of these AD mirrors.

References

[1] S. D. Smith, “Design of multilayer filters by considering two effective interfaces,” J. Opt. Soc. Am. 48, 43-50 (1958).

[2] A. V. Oppenheim, R. W. Schafer and J. R. Buck, *Discrete-time signal processing*, 2nd ed. (Prentice Hall, N.J., 1999)

[3] Y.V. Troitski, “Dispersion-free, multiple-beam interferometer,” Appl. Opt. 34, 4717-22 (1995).

[4] Y.V. Troitski, “Synthesis of mirrors with anomalous dispersion of the reflection phase,”.Opt. Eng. 34(5), 1503-7 (1995)

[5] DE Inspec, RJ Pegis, “Methods of synthesis for dielectric multilayer filters**,”** in *Progress in optics,* vol.VII (North Holland, London, UK, 1969), 69-135

Chapter 4 Wide-Field of View GaAs/AlxOy 1-D Photonic Crystal Filter

4.1 Introduction

An optical filter having a wide range of acceptance angles (wide angular bandwidth) and simultaneously a narrow spectral (i.e., wavelength) passband would be extremely useful in a free-space optical communication system among mobile nodes, where the relative bearing of the transmitter-receiver pair is unknown. Such a filter will reject the out of passband ambient light coming from the environment (e.g., sun, moon, and other sources). The transmission bandwidth of such a filter needs to be wide enough to transmit the information-carrying beam consisting of the optical carrier and the sidebands. Such functionality can be achieved by introducing a narrow flat-top transmission band into a broad stop band. The design of such a spectral filter operating with wide angular bandwidth requires special attention, as these two characteristics (i.e., angle and wavelength) are not independent.

In this chapter, we present the design, fabrication and characterization of a wide-field-of-view narrow band wavelength filter using the principles of a 1-D PC structure with multiple defects (i.e., resonant cavities) and the design method developed in the previous chapter. In Section 4.2 we describe the design procedure to achieve a square bandpass filter, optimized to minimize the shift in wavelength versus the angle of incidence of the input radiation. In Section 4.3 we present the tolerance of the design with the possible inaccuracies of design parameters. In Section 4.4 we describe the fabrication procedures, optical characterization results of the fabricated filters and

comparison with the design performance. In Section 4.5 we summarize the content of this chapter.

4.2 Design principles and approach

Our goal is to design a filter that transmits narrow bandwidth laser radiation incident from wide angular bandwidth range and simultaneously rejects ambient light coming from the environment. Conceptually, a 1-D PC structure made of high contrast refractive index materials implements a filter with very wide reflectance bandwidth to reject the ambient light. By introducing a single defect in the 1-D PC structure, we can introduce a narrow transmittance band at the desired optical frequency. Such a design can be seen as a simple Fabry-Perot cavity, transmitting radiation centered at the resonant frequency. The bandwidth of the transmission depends on the reflectivity of the mirrors realized in our case by the 1-D PC structure. The reflectivity usually needs to be high to achieve good rejection of the out of band radiation, thereby producing a narrow resonant transmission band in the stop band of such a PC-based filter. Unfortunately, when the angle of incidence in such a 1-D filter changes, the resonant transmission band shifts in wavelength as a result of the rejection of the desired signal. To overcome this issue, we develop a novel design optimization procedure for wide field of view filters based on introducing multiple resonant cavities into the 1-D PC structure in order to simultaneously minimize the angular sensitivity of the filter and optimize the passband shape and width for the specific application.

There are two main issues that need to be addressed in constructing a filter with a flat-top transmission passband operating with wide angular bandwidth signals: (1) the

flat-top passband and (2) the wide angular transmittance bandwidth as discussed below. In the following discussion, we will show results for the TE polarization state, while noting the same approach is applicable to the TM polarization.

A. Flat top passband

In the previous chapter, a flat top transmission band can be obtained under the conditions $\Phi=2m\pi$ and $d\Phi/d\omega=0$ for operation at the design wavelength λ_o [1]. In order to meet the condition $d\Phi/d\omega=0$, AD mirrors are required to provide the desired reflectance phase.

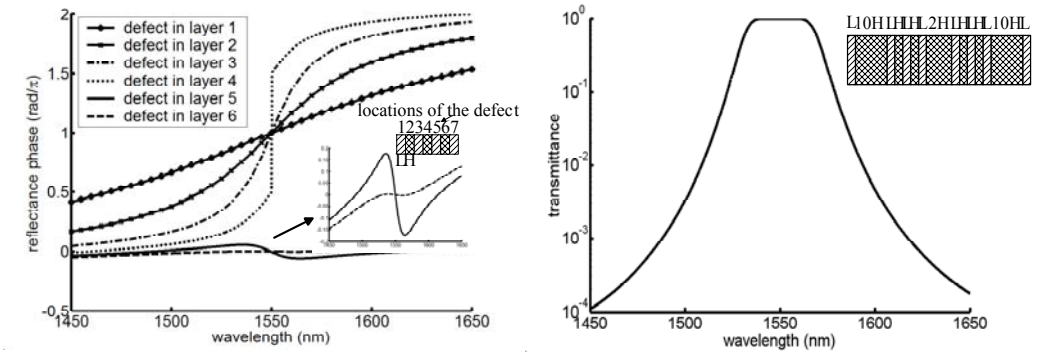

(a) (b)

Fig. 4-1 (a) Reflectance phase vs wavelength for an AD mirror realized using a 7 layer stack (H|LHLHLHL|H) with n_H=3.374 and n_L=1.50. Optical thickness of L and H is $\lambda_o/4$ at λ_o of 1550 nm and in one layer a defect is introduced having a thickness of a full-wave, λ_o. The upper inset is the structure of 7-layers stack, and the lower inset is the enlarged curves for the reflectance phases of the AD mirrors with the defect in the fifth or sixth layer, respectively. (b) Transmittance of a flat-top bandpass filter having a structure H|L10HLHLHL2HLHLHL10HL|H

Consider a 1-D PC made of 7 layers LHLHLHL (see inset of Fig. 4-1(a)), where H and L respectively represent the quarter-wave thickness of GaAs and Al_xO_y layers with corresponding refractive indices n_H=3.374 and n_L=1.50 for the design wavelength of 1550 nm. A given layer can be converted into a defect by increasing the thickness of that layer, thereby altering the reflectance and reflectance phase of the stack. Fig. 4-1(a)

shows the reflectance phase of a PC with different locations of the defect. The desired AD in reflectance phase is obtained when the defect is located in the fifth or sixth layer. In addition, as the location of the defect is moved from the fifth to sixth layer, the AD region increases but the slope of reflection phase at 1550 nm decreases. The slope of the reflection phase needs to be chosen to compensate for the phase variation of $\omega c^{-1} n d \cos\theta$ acquired by resonance frequency waves propagating in the cavity. By using these AD mirrors in designing the bandpass filter, a flat-top transmission band can be obtained. Fig. 4-1(b) shows the transmittance of a flat-top bandpass filter designed with two identical AD mirrors having a defect located in the sixth layer, and a resonator cavity of $\lambda_o/2$ optical thickness. In order to compensate for the phase shift caused by the cavity and obtain unity transmittance at λ_o, the optimized optical thickness of the defect in the AD mirror has to be $2.5\lambda_o$.

B. Wide field of view

Next we consider the dependence of the filter transmittance properties on the angle of the incident radiation. It is well known that as the incident angle increases, not only does the center of the resonant transmission band shift to shorter wavelengths, but its shape is also altered. For example, consider an AD mirror composed of layers $L_1H_1L_1H_1L_1H_2L_1$, where L_1 and H_1 represent the optical thicknesses of the GaAs and Al_xO_y layers, and satisfy the relation $L_1+H_1=\lambda_o/2$. H_2 is the optical thickness of the defect in the AD mirror causing the resonance to occur at 1550 nm. The 15-layer bandpass filter can be described by $H|L_1H_2L_1H_1L_1H_1L_1H_3L_1H_1L_1H_1L_1H_2L_1|H$, where H_3 is the optical thickness of the resonant cavity C, determining the transmittance spectrum.

The optical thickness ratio $\zeta = H_1/L_1$. Fig. 4-2(a) depicts examples of the transmittance of this structure with ζ=0.67, 1.00, 2.33 and 4.00 for incident angles of 0°, 25° and 50° in air. As the incident angle increases, we find that not only does the transmittance at 1550 nm decrease to values less than 1, but also the shape of the transmittance curve is distorted for small values of ζ. In addition, as ζ increases, the bandwidth increases while the spectrum shift decreases. Fig. 4-2(a) indicates that the parameter ζ can be used to optimize the desired field of view. In the optimization process we would like to determine the cavity material and the optical thickness ratio ζ of the AD mirrors by considering the following characteristics of the filter: spectrum shift, transmittance at the design wavelength deviating from normal, and the filter bandwidth.

In the design process we begin with the material of the cavity. The actual optical path inside the medium decreases as the incident angle increases (i.e., the optical thickness of the cavity in the Fabry-Perot structure is $ndcos\theta$, and as the incident angle increases, the center of the transmittance spectrum shifts to shorter wavelength). It is evident from Snell's law that to minimize the effect of angle of incidence we should use a high refractive index material (GaAs) in the cavity, minimizing the shift of the center wavelength of the transmittance band of the filter. For example, for a half-wave thickness layer and incidence angle in air varying from 0 to 50±, the corresponding wavelength shift using a defect made of GaAs layer will be only 40 nm.

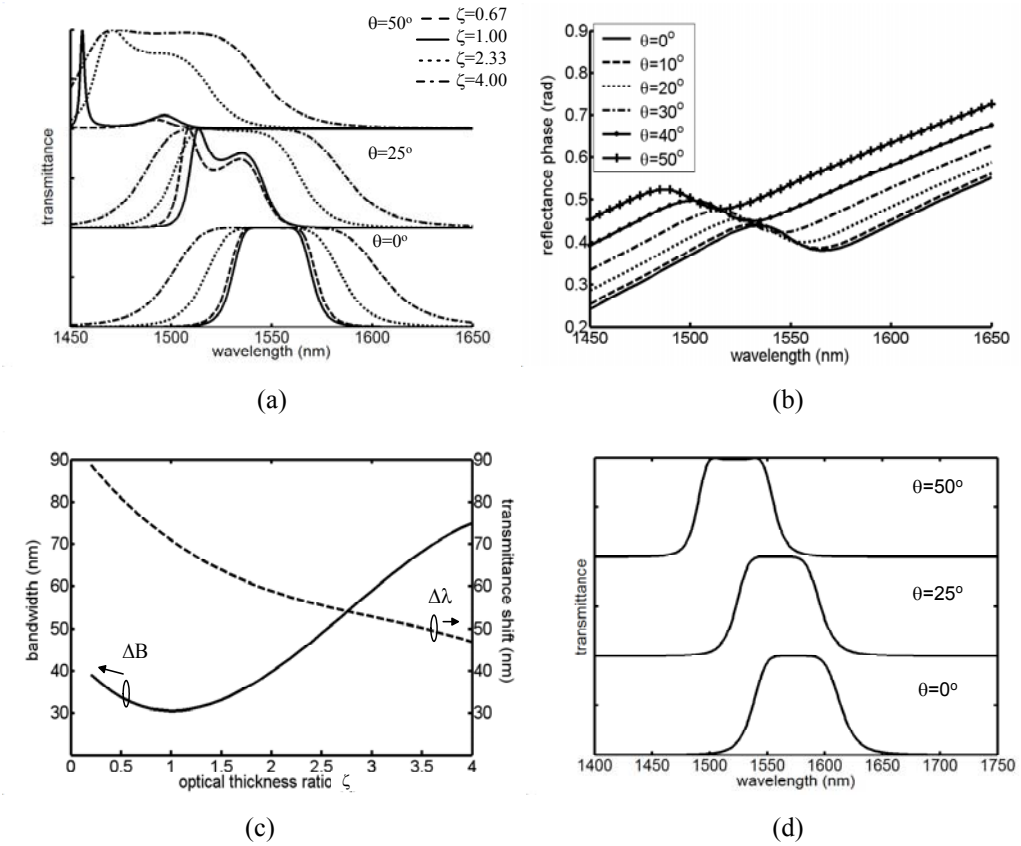

Fig. 4-2 (a) Bandpass filter designs with different optical thickness ratios η analyzed for transmittance with incidence angles θ =0°, 25°, and 50°. The filter is H|L1H2L1H1L1H1L1H3L1H1L1H1L1H2L1|H with optical thickness ratio η=H1/L1. The dashed line corresponds to ζ=0.67 with b=9.84 and c=1.87. The solid line is the case of ζ=1, H2=10H and H3=2H. The dotted line is the case of ζ=2.33, H2=6.29H and H3=2.26H, and the dash-dotted line is the case of ζ=4, H2=6.46H, and H3=2.42H. The results are calculated for TE polarization. (b) Reflectance phases of the AD mirror with ζ=2.33 with incidence angles θ =0°, 10°, 20°, 30°, 40° and 50° (c) Shift of the center wavelength of the filter $\Delta\lambda_{50}$ and the filter bandwidth ΔB of a 15-layer flat-top bandpass filter vs ζ. The spectrum shift $\Delta\lambda_{50}$ is found by changing the incidence angle from 0 to 50° and the bandwidth ΔB is the range where the transmittance is larger than 0.9 at normal incidence. (d) Transmittance of the designed filter at incidence angles of θ =0°, 25°, and 50°.

The second parameter we use in our design is the optical thickness ratio (ζ) of the AD mirrors. To reduce angular selectivity we use a GaAs substrate material with 7-layer AD mirror consisting of $L_1H_1L_1H_1L_1H_2L_1$. First we consider obtaining high transmittance independently of the angle of incidence at the design wavelength (1550 nm). This implies that for the center wavelength λ_o we would like to achieve invariance

in θ for the total phase shift Φ with the approximate value of (2m)π such that Eq. (3.7) is invariant in θ. This condition can be satisfied when the variation of the phase change caused by the cavity length is equal to the variation of the phase upon reflection from the AD mirrors. It is evident that as the incident angle increases, the phase variation due to the cavity length decreases. Next, we examine the variation of the phase upon reflection from the AD mirrors as the incident angle increases. Fortunately, the reflectance phase of the AD mirrors in the AD region at the design wavelength also decreases as the angle of incidence increases, compensating for the phase variation of Φ [2]. Ref[2] shows that the reflectance phase is related to the wavelength and the total optical thickness of the multilayer structure. However, as the incident angle is tilted, the total optical thickness is also reduced. Consequently, the reflectance phase in the AD region is reduced approximately in proportion to the total optical thickness. Fig. 4-2(b) shows an example of reflectance phase of the AD mirror, $H|L_1H_1L_1H_1L_1H_2L_1|H$ with ζ=2.33, with different incident angles. The reflectance phase in the AD region is reduced as the incident wave is tilted, whereas outside this regime it is increased. In this instance, however, at incident angles larger than 20°, the reflectance phase at 1550 nm increases with incident angle. The anomalous region of the reflectance phase, and the reflectance spectrum of the AD mirrors shift to shorter wavelengths simultaneously with the incident angle. Additionally, the width of the AD region determines the bandwidth of the bandpass filter. Therefore, the bandwidth of the bandpass filter has to be designed larger than the amount of the spectrum shift of the AD mirrors within the desired range of the variation of the incident angles in order to obtain high transmittance at λ_o.

First, we define two parameters:$\Delta\lambda_\theta$, the shift of the center wavelength of the bandpass filter as the incidence angle is changed from 0° to θ°. The second parameter is the filter transmission bandwidth, ΔB, that is defined as the wavelength range for transmittance larger than 0.9 at normal incidence. Fig. 4-2(c) shows $\Delta\lambda_{50}$ and ΔB variations of a 15-layer flattop bandpass filter structure, $H|L_1H_2L_1H_1L_1H_1L_1H_3L_1H_1L_1H_1L_1H_2L_1|H$, for various values of the optical thickness ratio η. We observe that ΔB(ζ) is a minimum at ζ=1, whereas $\Delta\lambda_{50}(\zeta)$ is a monotonically decreasing function. The two curves intersect at an optical thickness ratio of approximately ζ=2.8, showing that for an optical thickness ratio larger than 2.8, the amount of the spectrum shift is smaller than the bandwidth of the bandpass filter and can be ignored, making a good approximation to our desired filter performance design.

By using the thickness ratio ζ=2.8 obtained in the previous discussion, the thickness of the GaAs layer (H_1) is 160.5 nm and that of Al_xO_y (L_1) is 131.3 nm. Due to the different media on the two sides of the mirrors, a modification of the seventh layer is necessary to obtain approximately unity transmittance at 1550 nm at normal incidence. The structure of the AD mirror next to the air is changed to $L_1H_1L_1H_1L_1H_2{}'L_1{}'H_1{}'|$air and next to the substrate to $L_1H_1L_1H_1L_1H_2{}''L_1{}''|H$, and hence the total number of layers in the final design is 16. $L_1{}'$, $H_1{}'$, and $L_1{}''$ are adjusted to obtain the same reflectance of the structure $H|L_1{}'H_1{}'|$air, and $H|L_1{}''|H$ at 1550 nm. In addition, $H_2{}'$ and $H_2{}''$ have to be adjusted to obtain the resonance of two AD mirrors at 1550 nm.

From Fig. 4-2(b), we know that ΔB is roughly 54 nm at the intersected point. Consequently, the choices of $L_1{}'$, $H_1{}'$, $L_1{}''$, $H_2{}'$ and $H_2{}''$ have to achieve a bandwidth of the

AD region larger than 54 nm. The thicknesses of $L_{1'}$, $H_{1'}$, and $L_{1''}$ are 92.9 nm, 214.3 nm and 195.3 nm, respectively. The thickness of $H_{2'}$ is 493.5 nm whereas that of $H_{2''}$ is 502.7 nm. Then by positioning these two AD mirrors in opposition, H_3 is adjusted to achieve a flat-top passband - in this case 515.4 nm. The transmittance of the final design for TE polarization incidence with incident angles of θ=0°, 25°, 50° are shown in Fig. 4-2(d). The full width at half maximum (FWHM) at normal incidence is 76.4 nm and ΔB is 53 nm. In addition, the wavelength shift is 51.67 nm as the incident angle is changed from 0° to 50°, which is smaller than ΔB, as desired.

4.3 Tolerance of the design

It is impossible to produce a multilayer design as good as simulated results and the discrepancy predominantly results from imperfect materials, inaccurate thickness growth, etc. In the ensuing is a discussion of the sensitivities of our design on these possible factors: accuracy of the refractive index of Al_xO_y, the thickness errors of each layer and the absorption of the materials.

A. Refractive index of Al_xO_y

The Al_xO_y layer is obtained by oxidation of epitaxial AlAs/GaAs flims, and the refractive index varies depending on the content ratio of Al and O [3]-[8]. Fig. 4-3 shows the simulation results of the design by changing the refractive index of Al_xO_y layers from 1.45 to 1.55. As n_L increases, the spectrum shifts to a longer wavelength without the distortion of the spectrum with roughly 5.31 nm. Consequently, the design is little influenced on the variation of n_L except for spectrum shifting.

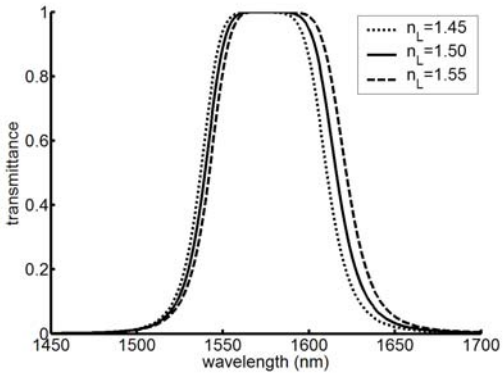

Fig. 4-3 Simulation of the effect of the refractive index of Al_xO_y in the bandpass filter design

B. The thickness of each layer

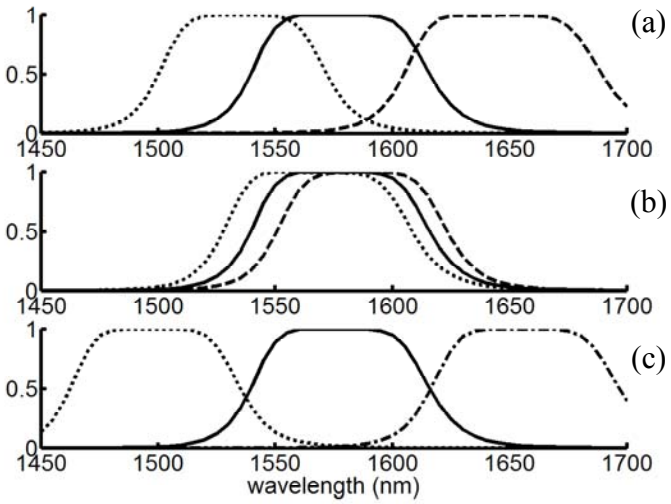

Fig. 4-4 Effect of thickness variation on the designed bandpass filter (a) variation of InGaAs layers ±5% . (b) variations of Al_xO_y layer with ±5% and (c) variation of InGaAs and Al_xO_y layers with the same rate ±5%.(dashed line for +5 % variation, solid line for 0% variation, and dotted line for -5% variation)

Suppose that the practical growth thickness of the i^{th} layer is $d_i=d_{i,design}(1+f_i(x))$, wherein the i^{th} layer has growth thickness of d_i, designed thickness of $d_{i,design}$, and thickness variation of $f_i(x)$. Fig. 4-4(a) shows transmittance shift due to the thicknesses of GaAs layers varying from 0.95% to 1.05% of the designed thicknesses. In addition to the shift, the bandwidth of transmittance is smaller as the thicknesses of the layers reduce.

The total amount of shift is 104.5 nm with 10% thickness variations of the GaAs layers. Fig. 4-4(b) illustrates similar phenomena with thickness changes of the Al_xO_y layers. However, the shift amount (that is 23.08 nm) is much less than that of variations on GaAs layers due to thinner total thickness of the Al_xO_y layers. Fig. 4-4(c) shows transmittance with different variations of the thicknesses of GaAs and Al_xO_y layers at the same rate. We find that the spectrum is approximately the same except for shifting.

C. Absorption of materials

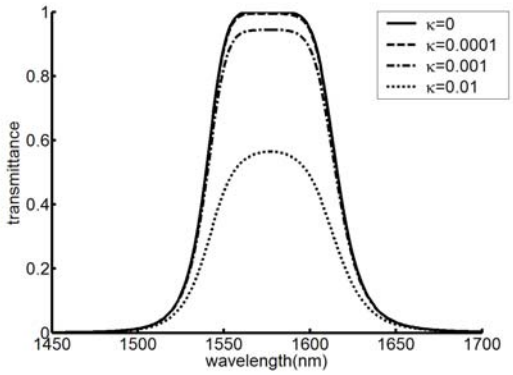

Fig. 4-5 Transmittance of the design with the variations of absorption coefficient

Due to impurities of materials or defects in the coating, losses associated with all layers are inevitable. Fig. 4-5 shows simulated transmittance of the designed with the introduction of the absorption into the layers. The refractive indices of the materials become n-iκ under the assumption all materials have the same absorption coefficient. As shown, the transmittance reduces due to the increase of the absorption. In addition, the spectral shape becomes rounder as well. As $\kappa=10^{-4}$, the absorptance (=1-R-T) at the wavelength of 1550 nm is 0.6%, and as $\kappa=10^{-2}$, the absorptance becomes 43.5%

Summarizing the study, we find this design is not sensitive to the variations of the refractive indices in materials and the inaccuracies of the growth thicknesses. However,

the absorption of the materials predominantly controls the performance of the filters. As $\kappa<2x10^{-3}$, the absorptance of the whole system at the center wavelength is less than 0.5 dB.

4.4 Fabrication and characterization

The filter design procedure discussed in Section 4.2 was used to construct a filter made of a multilayer structure of the high refractive index contrast materials GaAs/ Al_xO_y. The fabrication approach is based on growing a multilayer structure of GaAs/AlAs, followed by an oxidation process converting AlAs into Al_xO_y. Binary GaAs/AlAs multilayers are grown by MBE at 600±C. Nominal film thicknesses are calibrated in-situ by RHEED measurements, but actual values are determined by ex-situ optical normal incidence reflection and angularly dependent transmission measurements. The structure consists of a GaAs buffer layer followed by the layers detailed in Table I. Actual thicknesses are again determined optically—in this case with an error of ~1.5%—which results in a shift in the center wavelength of the passband of about 23 nm.

In order to measure the transmission of relatively small devices in a large range of angles of incidence, a configuration analogous to confocal imaging is adopted, as shown in Fig. 4-6. A variable aperture pinhole is imaged onto the particular device to be measured from the transmitted side. Illumination from a broadband tungsten-halogen source is limited to a spot size of ~50 μm in diameter on a particular device to be measured. In this way, a low power microscope objective with a long working distance is utilized without inhibiting rotation of the sample to large incident angles. Samples are lapped and polished, and an InGaAs CCD array is used for imaging and alignment. The

signal is simultaneously sent to a scanning monochromator-photodetector apparatus to measure the spectral response from 1000 nm to about 1700 nm (limited in this case by the response of the InGaAs photodiode).

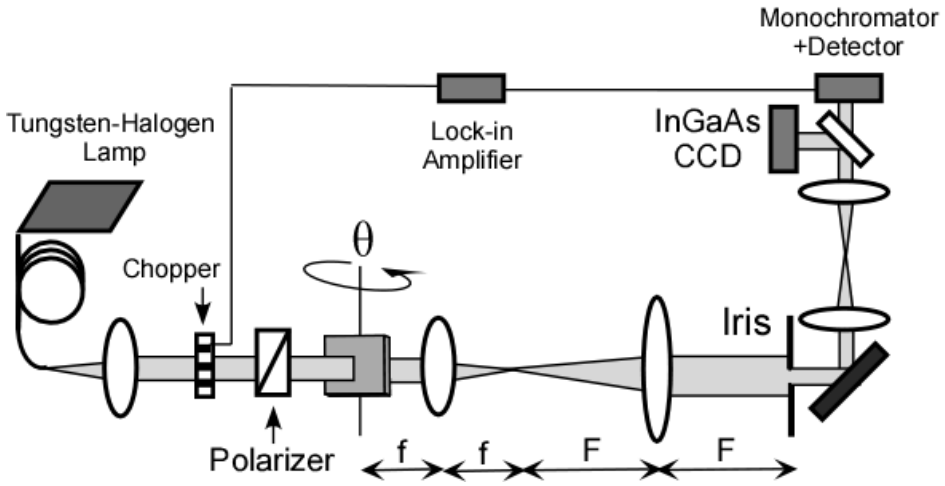

Fig. 4-6 Optical characterization apparatus. The broadband incident beam is collimated, and polarized. The sample is then 4F imaged via a lens onto a pinhole for alignment and control of measurement area, and 4F imaged again onto an InGaAs CCD and spectrum analysis setup.

Measured transmission spectra for TE polarization at normal incidence are shown in Fig. 4-7(a). In this curve, the dispersion of GaAs was included to accurately fit the spectral features of the transmission beyond the stop-band of the filter below about 1300 nm, while the oxide is considered dispersion-free with a constant index 1.50 as determined above. The measured values are found in good agreement with the calculations over the whole spectral range from 1000 nm to 1700 nm. All results are shown normalized to the transmission maximum due to Fresnel reflection from the back surface of the substrate that changes with the angle of incidence, with a maximum of over 90%. Fig. 4-7(b) shows details on the behavior of the transmission band as a function of the angle of incidence for the TE polarization, offset by angle of incidence for clarity. The wavelength shift over the angle change from 0° to 50° is 44 nm, which is quite close

to the expected design value of 51.67 nm. Additionally, ΔB=37.4 nm at the normal incidence. As noted above, the transmittance band tends to narrow for the TE polarization as expected—from about 65 nm FWHM at normal incidence to 57 nm at 50°, which is slightly smaller than the predicted values of 76.4 and 67 nm, respectively.

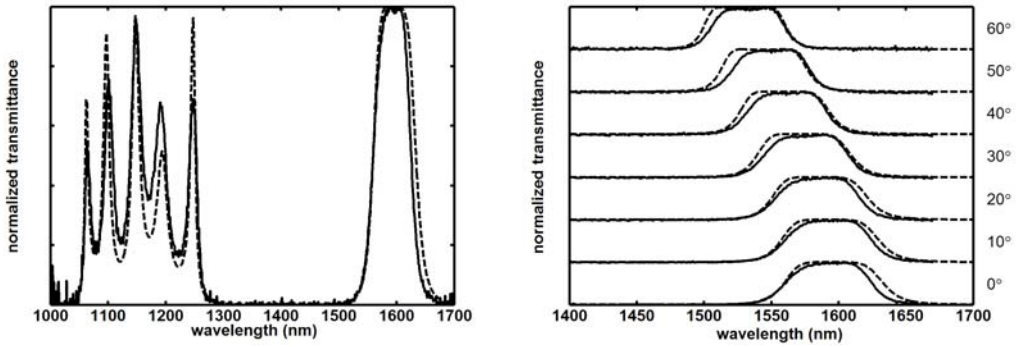

(a) (b)

Fig. 4-7 (a) Normal incidence transmittance of the filter shows the stop band and the narrow transmission band. Measured data is shown in solid line, and the calculated values, with the oxide index of 1.50, are dashed. Dispersion in the GaAs is accounted to accurately fit the data in the lower wavelength regime. (b) Transmittance for various angles of incidence. The solid and dashed lines correspond to the measured data and the calculated data using transfer matrix methods.

4.5 Summary

In summary, we have demonstrated the design, fabrication, and characterization of a resonant spectral filter with a wide stop band and a flat-top passband based on a GaAs/Al_xO_y material system. The design method provides an analytic and systematic approach to simultaneously optimize the passband width, shape and angular sensitivity characteristics. The design of the multiple-defect 1D PC-based filter is optimized by adjusting the optical thickness ratio of the anomalous-dispersion Bragg mirror layers in a high-index-contrast material system. In addition, the optimized design incorporates the experimentally determined optical properties of the oxidized GaAs/Al_xO_y layers to facilitate good agreement between the calculated and measured results.

A flat-top bandpass filter design for center wavelength 1550 nm with FWHM 76.4 nm and wavelength shift of 51.67 nm as the incident angle is varied from 0 to +50° is presented. Experimental characterization of the fabricated device shows a center wavelength at 1600 nm with FWHM of 65 nm and wavelength shift of 44 nm as the incident angle varies from 0 to +50°. The experimental results are in good agreement with the design, taking into consideration the spectrum shift to longer wavelength resulting from a roughly 1.5% thickness error in the fabrication of each layer.

4.6 Acknowledgements

The text of this chapter, in part or in full, is a reprint of the material as it appears in the Applied Optics [9]. The dissertation author was the primary researcher and/or the co-authors listed in this publication directed and supervised the research which forms the basis for this chapter.

References

[1] YV. Troitski, "Dispersion-free, multiple-beam interferometer," Appl. Opt. 34**,** 4717-22 (1995).

[2] A.V. Tikhonravov, P.W. Baumeister, K.V Popov, "Phase properties of multilayers," Appl. Opt. 36**,** 4382-92 (1997).

[3] E. F. Schubert, M. Passlack, M. Hong, J. Mannerts, R. L. Opila, L. N. Pfeiffer, K. W. West, C. G. Bethea, and G. J. Zydzik, "Properties AlAs/GaAs films of Al O optical coatings on GaAs produced by oxidation of epitaxial," Appl. Phys. Lett. 64, 2976–2978 (1994)

[4] See, for example, KD Choquette, KM Geib, CIH Ashby, RD Twesten, O Blum, HQ Hou, DM Follstaedt, BE Hammons, D Mathes, R Hull, "Advances in selective wet oxidation of AlGaAs alloys," IEEE J. Selected Topics in Quantum Electronics.**3,** 916-26 (1997), and the references therein.

[5] H.Q. Jia, H. Chen, W.C. Wang, W.X. Wang, W.Li, Q Huang, J. Zhou, and Q.K. Xue, "Improved thermal stability of wet oxidized AlAs," Appl. Phys. Lett. 80**,** 974-976 (2002).

[6] K.J. Knoop, R.P. Mirin, D.H. Christensen, K.A. Bertness, A. Roshko, and R.A Synowicki, "Optical constants of $(Al_{0.98}Ga_{0.02})_xO_y$ native oxides," Appl. Phys. Lett. 73**,** 3512-3514 (1998).

[7] P. Sifkis, P. Paddon, V. Pcradouni, M Adamcyk, C. Nicoll, A.R. Cowan, T. Tiedje, and Jeff F. Young, "Near-infrared refractive index of thick, laterally oxidized AlGaAs cladding layers," J. Lightwave. Technol. 18, 199-202 (2000).

[8] Hall, D.C, Wu, H, Kou, L., Lou, Y., Epstein, R.J., Blum, O., and Hou. H., "Refractive index and hydroscopic stability of $Al_xGa_{1-x}As$ native oxides," Appl. Phy. Lett. 75**,** 1110-1112 (1999).

[9] Chyong-Hua Chen, Kevin Tetz, Wataru Nakagawa, and Y. Fainman, "Wide-field-of-view GaAs/AlxOy one-dimensional photonic crystal filter," Appl. Opt. 44 (8), 1503-1511 (2005*)*

Table 1 The designed thicknesses of the 15-layer filter

Layer	Design Thickness [nm] (As grown)	Design Thickness (Oxidized)
1 AlAs	224.5	195.3
2 GaAs	502.7	502.7
3 AlAs	150.9	131.3
4 GaAs	160.5	160.5
5 AlAs	150.9	131.3
6 GaAs	160.5	160.5
7 AlAs	150.9	131.3
8 GaAs	515.4	515.4
9 AlAs	150.9	131.3
10 GaAs	160.5	160.5
11 AlAs	150.9	131.3
12 GaAs	160.5	160.5
13 AlAs	150.9	131.3
14 GaAs	493.5	493.5
15 AlAs	106.8	92.9
16 GaAs	214.3	214.3

Chapter 5 Resonant-Cavity-Enhanced PIN Photodiode with Broad Quantum Efficiency Spectrum

5.1 Introduction

High speed and high sensitivity resonant cavity-enhanced (RCE) photodetectors (PDs) are promising devices for free-space optical communications, optical interconnects, metrology, and optical sensing applications [1]-[5]. Insertion of a photosensitive active media within a Fabry-Perot resonant (FPR) cavity enhances the detection quantum efficiency due to the multiple reflections between the two mirrors of the FPR cavity, effectively increasing the absorption depth of the active media. Additionally, the FPR cavity can be designed to have a very narrow band spectral transmission in order to satisfy a particular application. However, for certain applications (e.g., high speed telecommunications) that desire a broader and flat-top transmission band for wide angular bandwidth (e.g., free space communications), a RCE PD built with a simple FPR filter will be limited due to (1) high wavelength sensitivity as a result of the narrow transmission function determined by the characteristics of the cavity (length, mirror reflectivity) and (2) high sensitivity to the angular bandwidth due to strongly angular dependence of the FPR cavitye at a given wavelength. Moreover, fabrication of such a RCE detector will be challenging due to the difficulty in meeting the tolerance of aligning the resonance frequency.

In this chapter, we analytically derive the design rules for achieving a RCE PD with a flat-top spectral response, and provide an example of such a device working in the

telecommunication spectral band. In Section 5.2 , we present a semi-analytical formulation to accurately describe quantum efficiency of a RCE PD. In addition, we systematically develop an analytic approach to achieve flat-top quantum efficiency of the RCE PD by examining the properties of both mirrors, including spacers and their relations to the thickness of the active layer. We show that the shape of the quantum efficiency spectrum (or response) can be controlled by engineering the reflection phase properties of the spacer and the incident mirror, called the entrance mirror. The flat-top passband is obtained when the entrance mirror has an anomalous dispersion (AD) region in the reflection phase of the mirror. When the design of the mirror satisfies the optimum conditions, the flat-top quantum efficiency is obtained and the flatness of the spectral bandwidth is determined by the width of the AD region. In Section 5.3 we present numerical results for implementation of a RCE PD with flat-top quantum efficiency, and discuss engineering the spectral bandwidth response of the device. In Section 5.4, we optimize the parameters to maximize the angular bandwidth of these types of photodiodes by discussing the trade-off between the design parameters shown in Section 5.3. Section 5.5 provides a summary and discussions for further improvements of the device.

5.2 Principle

There exist two methods to calculate quantum efficiency of RCE PDs: one is an analytical formulation presented by Kishino et al in 1991[1] and the other is a numerical method using the transfer matrix method (TMM) [2], [3]. Due to the inclusion of the standing wave effect (SWE) and neglecting reflection at the interfaces between the active layer and the surrounding spacers in their model, the calculated results obtained by the

former need modification [6]-[10], and it becomes difficult to interpret some of the physical effects. On the other hand, because the latter method does not account for losses of the materials except in the active layer, it is inaccurate when applied to a structure with lossy materials for the mirrors. This occurs, for example, when one of the mirrors is metallic – as in the case addressed here. Therefore, here we develop another semi-analytical method to accurately describe quantum efficiency of conventional PIN RCE PDs. Instead of calculating the performance of spacers and mirrors separately, we group the spacer and the mirror, and then calculate its reflection and transmission properties by TMM. By calculating the power absorbed in the active layer, we obtain the quantum efficiency by the ratio of the absorbed power, $P_{absorption}$ to the input power, P_{in}. Detailed analysis is developed next.

A. Analysis

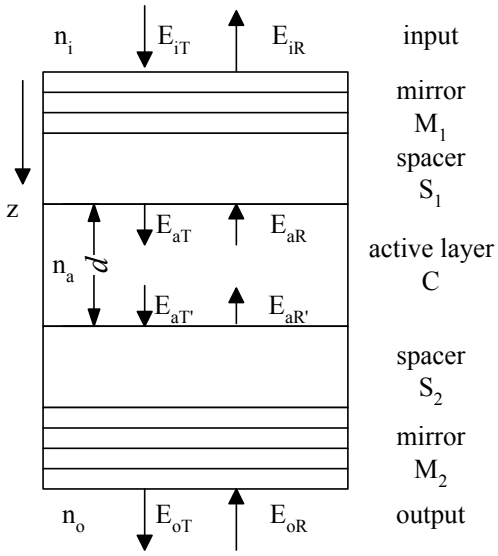

Fig. 5-1 Schematic structure of a generalized RCE photoreceiver

The conventional structure of a RCE device is shown schematically in Fig. 5-1. The photo-absorptive active layer (i.e., the detector layer) of thickness d, refractive index n_a and absorption coefficient α is inserted into a FPR cavity. The active layer C with two spacers S_1 and S_2 are integrated into a cavity made of two mirrors M_1 and M_2. The optical fields $\{E_{iT}, E_{iR}\}$, and $\{E_{oT}, E_{oR}\}$ denote transmitted and reflected waves in the input and output regions, respectively. $\{E_{aT}, E_{aR}\}$ describe the traveling waves at the interface between the active layer and the spacer S_1, whereas $\{E_{aT'}, E_{aR'}\}$ represent the traveling waves at the interface between the active layer and the spacer S_2. The relationships between $\{E_{iT}, E_{iR}\}$,$\{E_{aT}, E_{aR}\}$, and $\{E_{aT'}, E_{aR'}\}$,$\{E_{oT}, E_{oR}\}$ can be obtained via TMM [11] expressed by

$$\begin{bmatrix} E_{iT} \\ E_{iR} \end{bmatrix} = \begin{bmatrix} \frac{1}{t_{11}} & \frac{-r_{12}}{t_{12}} \\ \frac{r_{11}}{t_{11}} & \frac{1}{t_{12}} \end{bmatrix} \begin{bmatrix} E_{aT} \\ E_{aR} \end{bmatrix}$$

$$\begin{bmatrix} E_{aT'} \\ E_{aR'} \end{bmatrix} = \begin{bmatrix} \frac{1}{t_{21}} & \frac{-r_{22}}{t_{22}} \\ \frac{r_{21}}{t_{21}} & \frac{1}{t_{22}} \end{bmatrix} \begin{bmatrix} E_{oT} \\ E_{oR} \end{bmatrix}$$

$$\begin{bmatrix} E_{aT} \\ E_{aR} \end{bmatrix} = \begin{bmatrix} e^{(\alpha/2+j\beta)d} & 0 \\ 0 & e^{-(\alpha/2+j\beta)d} \end{bmatrix} \begin{bmatrix} E_{aT'} \\ E_{aR'} \end{bmatrix} \quad \text{.....(5.1)}$$

where $\{t_{11}, r_{11}\}$, $\{t_{12}, r_{12}\}$ are the transmission and reflection coefficients of the multilayer structure of the entrance mirror (i.e. the mirror M_1 and spacer S_1), as seeing from the input medium and from the active layer medium, respectively. Similarly, $\{t_{21}, r_{21}\}$, $\{t_{22}, r_{22}\}$ are transmission and reflection coefficients of the structure constructed by the bottom mirror (i.e. the spacer S_2 and mirror M_2), as seen from the active layer medium and from

the output medium, respectively. Here β is the propagation constant, equal to $k_o n_a$, where k_o is the wavenumber, $2\pi\lambda^{-1}$, and λ is the wavelength of the optical field.

The total power absorbed in the active layer is [1]-[2],

$$P_{absorption} = \frac{n_a}{2Z_o}\left(\left|E_{aT}\right|^2 + \left|E_{aR'}\right|^2\right)\left(1 - e^{-\alpha d}\right) \quad \text{.....(5.2)}$$

where Z_o is the characteristic impedance of electromagnetic waves in vacuum.

Finally, the quantum efficiency η of the RCE PD can be described by

$$\eta = \frac{P_{absorbtion}}{P_{in}} = \frac{n_a}{n_i}\frac{\left|t_{11}\right|^2\left(1 + r_{21}{}^2 e^{-\alpha d}\right)}{\left|1 - r_{12}r_{21}\frac{t_{11}}{t_{12}}e^{-\alpha d - 2j\beta d}\right|^2}\left(1 - e^{-\alpha d}\right) \quad \text{.....(5.3)}$$

If there is no absorption in the materials forming the entrance mirror in the operational spectral bandwidth of the device, then Eq.(5.3) can be rewritten as

$$\eta(\lambda) = \frac{(1 - r_1(\lambda)^2)(1 + r_2(\lambda)^2 e^{-\alpha d})(1 - e^{-\alpha d})}{(1 + r_1(\lambda)^2 r_2(\lambda)^2 e^{-2\alpha d} - 2r_1(\lambda)r_2(\lambda)e^{-\alpha d}\cos(2\beta d - \phi_1(\lambda) - \phi_2(\lambda))} \quad \text{.....(5.4)}$$

where we use the relations $r_{12} = r_1 e^{j\phi_1}$ and $r_{21} = r_2 e^{j\phi_2}$, and r_1, r_2 are amplitudes of r_{12} and r_{21}, ϕ_1, and ϕ_2 are the phases of them.

Compared to the analytical formulation [1], Eq. (5.4) is similar except that the calculation of r_1, r_2, ϕ_1, and ϕ_2 includes the properties of the spacers and mirrors, and hence the SWE is excluded in this model. In addition, as all layers of the structure except the active layer are lossless, this equation is equivalent to 1-R-T, where R and T correspond to reflectance and transmittance of the whole RCE PD structure, which is the same formulation to calculate quantum efficiency by TMM [2].

B. Conditions to obtain high quantum efficiency with flat-top spectrum

To design a RCE PD that will possess a flat-top and high quantum efficiency around the center wavelength λ_o, we need to control the design parameters to optimize the value of quantum efficiency. Suppose that the absorption coefficient of the active layer is non-dispersive, i.e. α is independent of wavelength. Since Eq. (5.4) has the same form as the analytical formulation [1], the maximum quantum efficiency can be obtained if $\Phi(\lambda_o)=2\beta d-\phi_1(\lambda_o)-\phi_2(\lambda_o)= 2m\pi$ (m=…-2, -1, 0, 1, 2…) and $r_1(\lambda_o)=r_2(\lambda_o)e^{-\alpha d}$ [1]. Next, to decrease the wavelength dependence of quantum efficiency (i.e., flat-top condition), we need to assure that the second derivative of η be as close to zero as possible around λ_o. The latter condition can be achieved by setting the first derivatives of r_1, r_2, and Φ at λ_o to zero.

Because η increases monotonically with r_2, we need r_2 to have a local maximum with zero first derivative at λ_o to achieve high quantum efficiency. By closely examining Φ, the term $2\beta d$ decreases as the wavelength increases. Because r_2 has a local maximum at λ_o, the phase ϕ_2 increases around λ_o as the wavelength increases. Therefore, ϕ_1 has to decrease with increasing wavelength in order to compensate for the phase variation of Φ caused by $2\beta d$ and ϕ_2. A mirror with such a property is called an AD mirror [12] and can be constructed by a resonant mirror as presented in Chapter 3 . Additionally, in order to achieve the flat-top passband (i.e., quantum efficiency) condition, r_1 has to be designed to have a local minimum at λ_o to achieve zero value of its first derivative.

In this section, we conclude that to achieve the highest value and flat passband of quantum efficiency, the conditions of (1) $\Phi(\lambda_o)=2m\pi$, (2) $r_1(\lambda_o)=r_2(\lambda_o)e^{-\alpha d}$, and (3)

$d\Phi(\lambda_o)/d\lambda=0$ have to be simultaneously satisfied. In the following section, we present several simulation results to discuss the effects of the entrance mirror designs on the performance of the RCE PDs, and additionally also discuss the design rules to optimally engineer the bandwidth of such a RCE PD with an AD mirror as the entrance mirror.

5.3 Numerical results

A. Materials

To simplify the fabrication and the discussion, we use a metallic mirror as the mirror M_2. To be compatible with fabrication process, Gold (Au, n_{Au}=0.56-9.81i) and Titanium (Ti, n_{Ti}=4.04-3.82i) are chosen [13]. Here, we choose n+-doped InP (n_{InP}=3.18), i-$In_{0.53}Ga_{0.47}As$ (n_{InGaAs}=3.6) and p+-doped InP for our heterojunction PIN PD. The absorption coefficient of $In_{0.53}Ga_{0.47}As$ is $10^4 cm^{-1}$. All values are given for the wavelength of 1500 nm. For the dielectric mirror M_1, we choose $In_{0.523}Al_{0.477}As$ (n_{InAlAs}=3.2) and $In_{0.531}Ga_{0.417}Al_{0.052}As$ ($n_{InGaAlAs}$=3.5) with bandgaps at 924 nm and 1450 nm [14], respectively. In the following simulations, we set the center wavelength of the design to λ_o=1560 nm, and the bottom mirror consisting of 294.4 nm-thick p+ InP (S_2), 5nm-thick Ti (M_{2a}) and 500nm-thick Au (M_{2b}) to simplify the discussion. The thicknesses of InAlAs/InGaAlAs (L/H) for dielectric mirror are 91.3nm and 139.4nm. In addition, S_1 and C represent thicknesses of the spacer n+InP layer and that of the InGaAs active layer, respectively.

B. Quantum efficiency with varying entrance mirror reflection phase

As discussed above, the flat-top passband is obtained when the entrance mirror has an AD reflection phase. This property can be achieved using a mirror consisting of

$S_1L(HL)^pH_1H(LH)^qLH_2$ with the condition p>q, where H_1 and H_2 are the thickness in the InGaAlAs layer, and p and q are the number of InAlAs/InGaAlAs pairs as discussed in Section 3.2 . To achieve the 3rd optimized condition, $d\Phi(\lambda_o)/d\lambda=0$, the derivative of ϕ_1 at λ_o have to be

$$\frac{d\phi_1}{d\lambda} = (2n_a d - \frac{d\phi_2}{dk_o})\frac{dk_o}{d\lambda} \quad \text{.....(5.5)}$$

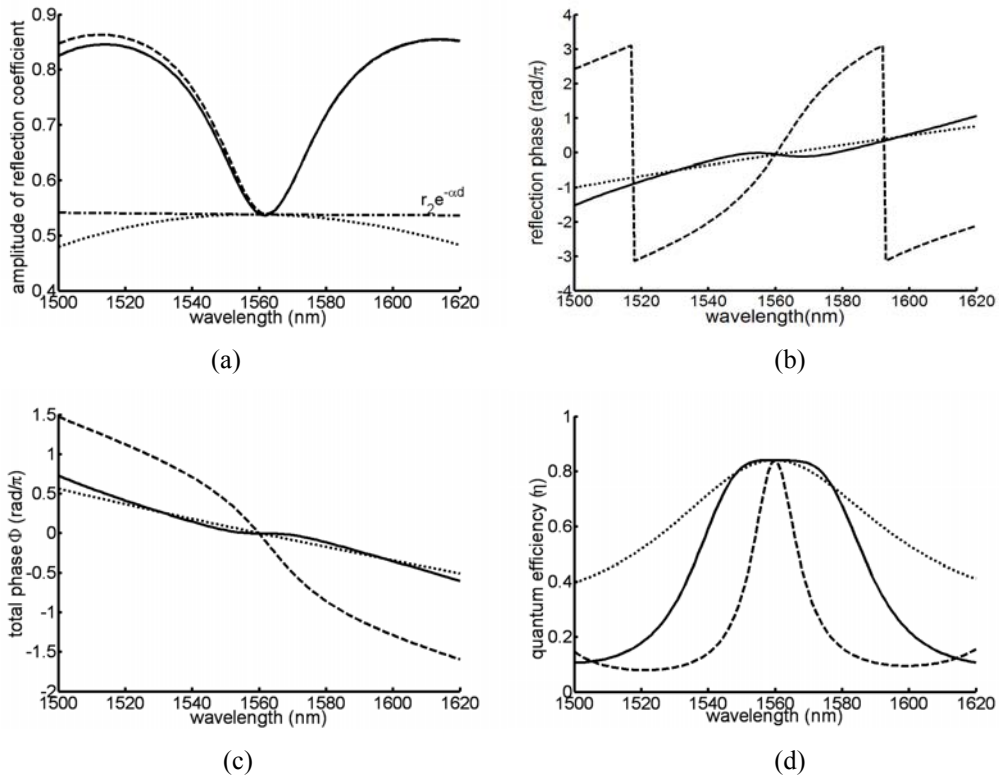

Fig. 5-2 Simulation results with different designs of the RCE PDs with the structure of $H_2L(HL)^qH_1(LH)^pLS_1CS_2M_2$, where p=13, q=7, H_1=249 nm, H_2=69.7 nm and S_1=355.8 nm (solid line), p=7, q=14, H_1=468.64 nm, H_2=69 nm, and S_1=220 nm (dashed line), and p+q=6, H_1=139.4nm, H_2= 61.5 nm and S_1= 358.3 nm (dotted line). Here, L and H are 91.3nm and 139.4nm. (a) Amplitude of the reflection coefficients of the entrance mirror with the structure of $S_1L(HL)^pH_1(LH)^qLH_2$, and the dash-dotted line is the curve of $r_2e^{-\alpha d}$. (b) Reflection phase of the entrance mirror ϕ_1. (c) Total phase shift Φ of RCE PDs. (d) Quantum efficiency of RCE PDs.

With this mirror as the entrance mirror of the RCE PD, the structure of our design is $H_2L(HL)^qH_1(LH)^pLS_1CS_2M_2$. For example, with an active layer 467.6 nm thick, we analytically obtain a maximum quantum efficiency of 0.84 when the amplitude of the

reflection coefficient of the entrance mirror r_1 is 0.54 at λ_o and $\Phi(\lambda_o)=2m\pi$. There are many combinations of H_2, H_1, S_1, p and q that satisfy the above specifications, and Fig. 5-2 shows the simulation results of three examples of the entrance mirror designs with the condition p>q (p=13, q=7), p<q (p=7, q=14), and H_1=H (p+q=6). Fig. 5-2(a) illustrates the relation between r_1 and the values of $r_2e^{-\alpha d}$. The three mirror designs satisfy the second condition, $r_1(\lambda_o)=r_2(\lambda_o)e^{-\alpha d}$, and the design for the case p>q has spectrum similar to that for the case p<q, whereas the design for the case H_1=H corresponds to conventional dielectric mirror performance. Fig. 5-2(b) shows that the reflection phase ϕ_1 has the desired AD region around λ_o only for the case of p>q. Fig. 5-2(c) displays the corresponding total phases ($\Phi(\lambda_o)=2m\pi$ in all cases). In addition, for the case p<q, Φ has the steepest variation at λ_o and for the case p>q, Φ has approximately zero variation at λ_o, and hence we expect that the quantum efficiency for the p>q case will have a flat-top response because it also satisfies our third condition $d\Phi(\lambda_o)/d\lambda=0$. Fig. 5-2(d) displays the corresponding quantum efficiencies, demonstrating that these three designs have the same maximum quantum efficiency of 0.84. Additionally, for the case p>q a flat-top passband is achieved around λ_o with a steeper edge response than that for the case H_1=H. The bandwidth at 0.02 dB (99.5 %) down from the peak is 13.3 nm. By examining the reflection phase ϕ_1 (Fig. 2(b)), we find that this value is approximately the same as the width of a AD region of ϕ_1, 13.6 nm. Quantum efficiency for the p<q case has the steepest edge response with the narrowest bandwidth. Even though only the entrance mirror has the AD property, a RCE PD possesses flat-top quantum efficiency spectrum where the width of the flatness is close to that of the AD region in reflection phase.

C. Spectral bandwidth engineering

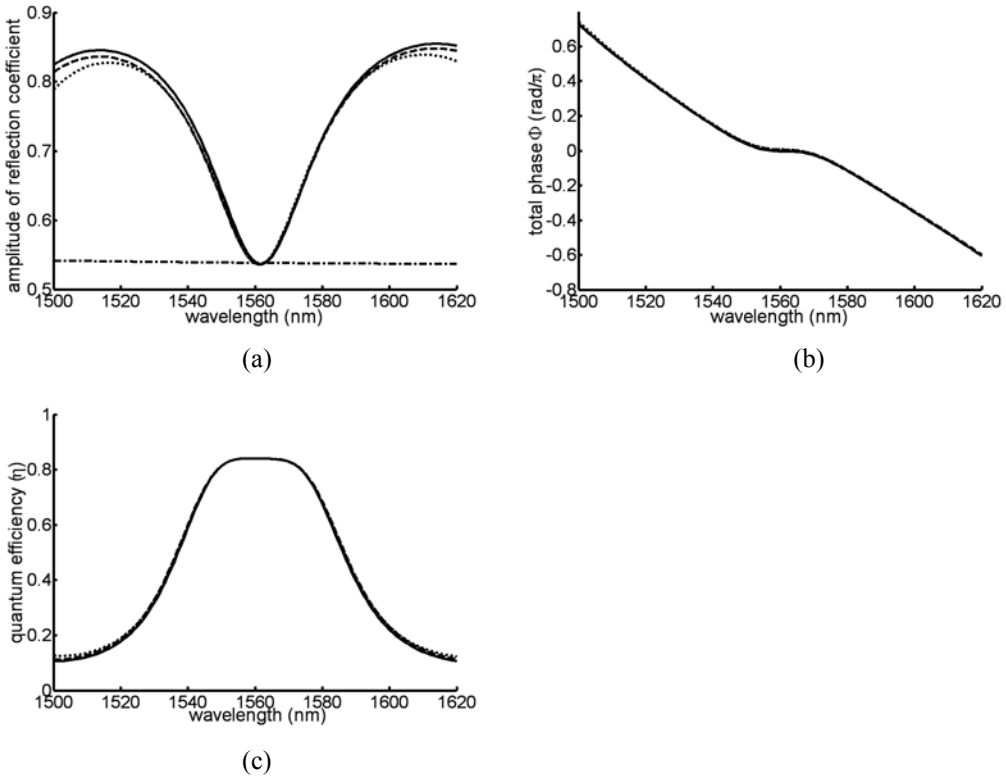

Fig. 5-3 The performance and the properties of the RCE PDs with the structure of $H_2L(HL)^qH_1(LH)^pLS_1CS_2M_2$, where p=13, q=7, H_1=249.0 nm, and H_2=69.7 nm (solid line), p=12, q=6, H_1=694.2 nm, and H_2=69.5 nm (dashed line) and p=11, q=5, H_1=1362.3 nm, H_2=69.5 nm (dotted line). Thickness of active layer C is 467.6 nm and S_1=355.8 nm. (a) The corresponding amplitude of the reflection coefficients of entrance mirrors $S_1L(HL)^pH_1(LH)^qLH_2$, and the dash-dotted line is the curve of $r_2e^{-\alpha d}$. (b) Total phase shift Φ of these three designs. (c) Corresponding quantum efficiency.

In this sub-section, we discuss the effect of the design parameters of $H_2L(HL)^qH_1(LH)^pLS_1CS_2M_2$ structure on the spectral bandwidth of a RCE PD. The flat-top bandwidth of quantum efficiency is nearly the same as the width of the AD region of the entrance mirror's reflection phase. In addition, Ref. [15] shows that the AD region width can be controlled by the reflection amplitudes of dielectric mirrors M_{1a} $(HL)^pLS_1$, and M_{1b}, $(LH)^qLH_2$, and the thickness of the defect which correspond to p, q and H_1. As a result, different values of p, q, and H_1 of the AD mirrors are chosen to satisfy the

optimized conditions, and their properties and performance are shown in Fig. 5-3. In Fig. 5-3(a), we see all three designs have similar amplitude of reflection coefficient spectra except at the off-resonance. In addition, as seen in Fig. 5-3(b), the total phases Φ in these examples are approximately the same. Hence, as expected, these designs have approximately the same quantum efficiency – except off-resonance – as shown in Fig. 5-3(c). As the reflectance of the AD mirror at off-resonance is smaller, slightly higher quantum efficiency is obtained. These results indicate that the bandwidth of the quantum efficiency is independent of the choices of p, q, and H_1 for a structure of $H_2L(HL)^qH_1(LH)^pLS_1CS_2M_2$ with fixed thicknesses of the active layer and the bottom mirror.

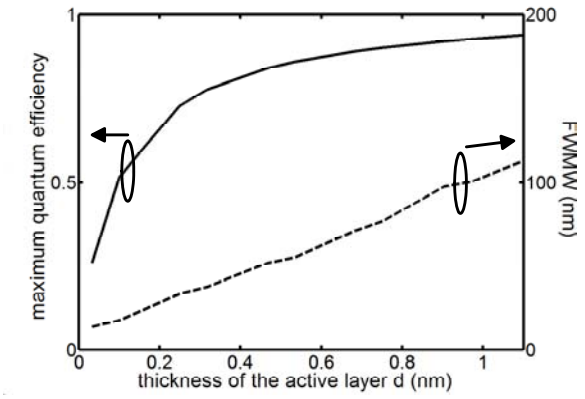

Fig. 5-4 The maximum quantum efficiency and bandwidth of the RCE PD with the structure of $H2L(HL)^qH_1(LH)^pLS_1CS_2M_2$ with the variations of the active layer's thickness

Subsequently, we investigate the dependence of the maximum quantum efficiency and bandwidth on the thickness of the active layer (see Fig. 5-4). Here the bandwidth is defined as full width at half of the maximum (FWHM) of quantum efficiency. We observe that both the maximum and the bandwidth of quantum efficiency increase as the thickness of the active layer d increases, showing that the bandwidth is approximately a linearly increasing function.

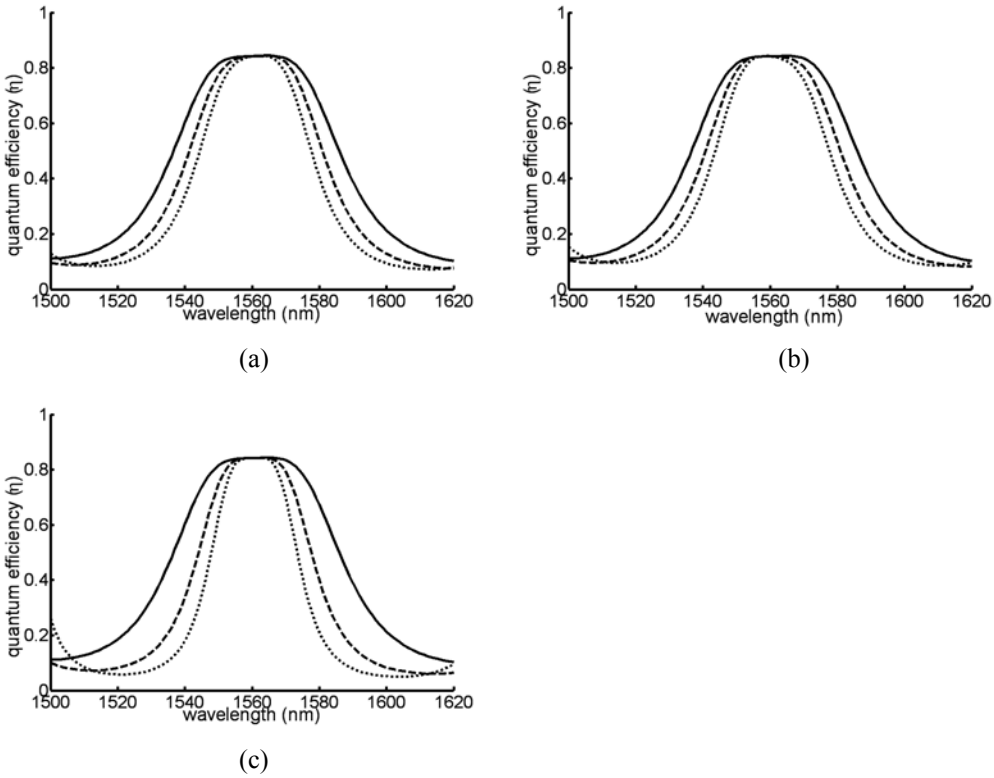

Fig. 5-5 Quantum efficiency with different orders of the cavity thickness H_1 and the spacer S_1 (a) Quantum efficiency of PDs with H_1=249.0 nm (solid line), 1137.9 nm (dashed line), and 2026.8 nm (dotted line). S_1=355.8 nm. (b) Quantum efficiency with S_1=355.8 nm (solid line), 1340.0 nm (dashed line), and 2324.2 nm (dotted line). H_1=249 nm. (c) Quantum efficiency with H_1=249.0 nm and S_1=355.8 nm (solid line), H_1=1137.9 nm and S_1=1340.0 nm (dashed line), and H_1=2026.8 nm and S_1=2324.2 nm (dotted line).

It is well known that the passband becomes narrower when high-order spacers in thin-film design are used [16]. We investigate these effects first by increasing the length of layer H_1 to operate at a higher-order thickness. Base on Eq. (3.11), the consequence of increasing the thickness of H_1 is a decrease of the reflection phase ϕ_1 at λ_o, and also an increase of Φ at λ_o. Fig. 5-5(a) shows the quantum efficiency with H_1=249, 1137.9 nm, and 2026.8 nm for RCE PDs with the structure of $H_2L(HL)^q\ H_1\ (LH)^pLS_1CS_2M_2$, where p=13, q=7, H_2=69.7 nm and S_1=355.8 nm. We see that as H_1 increases, the maximum quantum efficiency is unchanged. However, the FWHM of the transmission is reduced and also the curve's edge shape is rounded. The corresponding widths at 0.02 dB below

peak value are 13.3, 9.50, and 5.8 nm. On the other hand, as we increase the thickness of the spacer S_1 to higher-order thickness, we find a reduction in reducing the phase slope of ϕ_A at λ_o, and consequently Φ decreases at λ_o. Fig. 5-5(b) shows the quantum efficiency with S_1=355.8, 1340.0 and 2324.3 nm as H_1=249.0 nm, showing results similar to those for the case of higher-order H_1. The corresponding widths at 0.02 dB down from peak value are 13.3, 8.7 and 5.7 nm. We find that the quantum efficiency does not have a maximally flat passband because the third optimization condition is not satisfied. The above discussion demonstrates that the increases of H_1 and S_1 affect the slope of Φ at resonant wavelength differently, and for completion we show quantum efficiency with the different values of H_1 and S_1 which satisfy our third optimization condition in Fig. 5-5(c). The corresponding widths at 0.02 dB below from peak value are 13.3, 9.5 and 7.3 nm. We see that these designs possess not only wider flat-top width than those with either higher-order of H_1 or S_1, but also steeper edge response. Summarizing, the bandwidth of a RCE PD with $H_2L(HL)^qH_1(LH)^pLS_1CS_2M_2$ can be adjusted by varying the thickness of the active layer, the cavity H_1 and the spacer S_1.

5.4 Field of view

The other issue is the angular sensitivity of the photodiode. As has been investigated in Chapter 4 , while the incidence is tilted, not only does the reflection spectrum of the AD mirror shift to a shorter wavelength, but also reflection phase in the AD region decreases within several degrees of incident angles, thereby compensating for the phase reduction inside the cavity, i.e. the active layer, due to incident angle variations. In addition, the increase of optical thickness ratio ζ of the mirrors results in lessening

sensitivity of the mirror to the tilt of incident wave. Fig. 5-6 illuminates calculated quantum efficiency of two designs with different optical thickness ratios ζ and different incident angles θ. It indicates that a slightly narrower bandwidth in the case of ζ=1 is obtained as a result of the larger reflection phase slope in the quarter-wave stack. However, as the incident angle becomes 40°, distortion in the passband is realized with 0.3-dB reduction in the maximal quantum efficiency due to mismatch in the condition of $r_1(\lambda_o)=r_2(\lambda_o)e^{-\alpha d}$. On the other hand, in the case of ζ=1.66, although the bandwidth is slightly wider than in the case of ζ=1, the maximal quantum efficiency reduces only 0.08 dB with the spectrum shape remained. Consequently, less angular sensitivity and less spectrum distortion are achieved with the increase of the optical thickness ratio ζ.

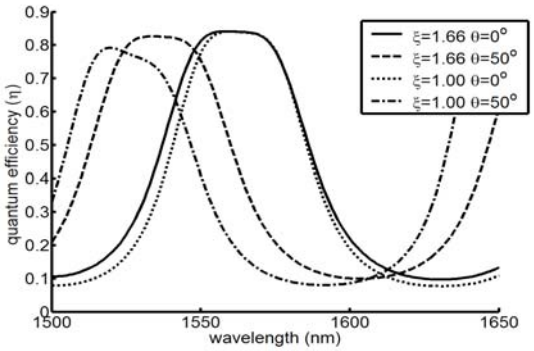

Fig. 5-6 Incident angle dependence of the designs with different optical thickness ratio ζ. The design structure is $H_2L(HL)^qH_1(LH)^pLS_1CS_2M_2$. Here, in the case of ζ=1.66, L=91.3, H=139.4, H_1=249.0, H_2=69.7 and S_1=355.8 nm, whereas in the case of ζ=1, L=111.1, H=121.5, H_1=224.4, H_2=120, and S_1=376 nm.

As seen in Fig. 5-6, as the incident angle increases, the spectrum shifts to a shorter wavelength with approximately unvaried spectrum, and hence the field of view is determined by the trade-off between the spectrum shift and the bandwidth of the photodiode. Fig. 5-7 shows the flatness bandwidth ΔB and the amount of spectrum shift $\Delta\lambda_\theta$ with different optical thickness ratios ζ to implement AD mirrors with equal total

number of layers in structures. As expected, the minimal flatness bandwidth is obtained as ζ=1, and $\Delta\lambda$ reduces as ζ increases. Furthermore, we see that $\Delta\lambda_{50}>\Delta B>\Delta\lambda_{40}$ in all ζ cases. An intersection at ζ=1.96 is obtained showing that the photodiode with optical thickness ratio ζ=1.96 has the optimized field of view of 45°. However, it indicates that it is impossible to achieve field of view of 50° by varying the optical thickness because the maximal deviation of ΔB and $\Delta\lambda$ with ζ=0.45~2.33 is roughly 3 nm, but the variation of $\Delta\lambda$ is roughly 5.6 nm as the incident angle changes from 45° to 50°. Therefore, in order to increase the field of view, i.e. increase the bandwidth of the photodiodes, the thickness of the active layer has to increase as studied in Section 5.2

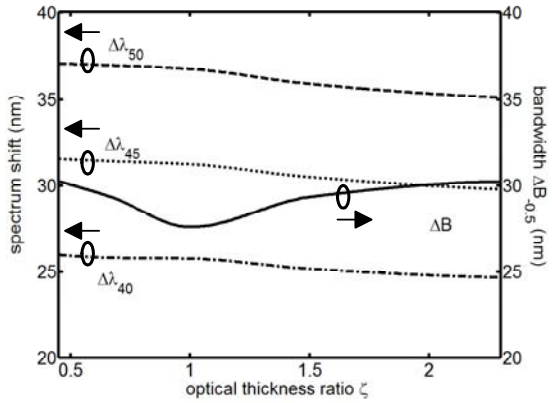

Fig. 5-7 The effect of the optical thickness ratio on the amount of the spectrum shift $\Delta\lambda$ with different incident angle variations and the flatness bandwidth

Shift spectrum and the flatness bandwidth with optical thickness ratio ζ=1.66 as a function of the active layer's thickness d is shown in Fig. 5-8(a). As d increases, the flatness bandwidth ΔB increases while the spectrum shift $\Delta\lambda$ decreases due to the thinner total thickness of the AD mirror with thicker d. In addition, the intersected points for optimum d are 430, 616, 753 and 810 nm corresponding to the field of views of 40, 50, 60

and 65°. Therefore, a wider field of view would be obtained by increasing the active layer's thickness d instead of increasing the optical thickness ratio ζ. Fig. 5-8(b) shows an example of the angular dependence of a RCE photodiode with the optimized d=753 nm and ζ=1.66, and similar phenomena to the results shown in Fig. 5-6 are obtained except wider bandwidth and larger quantum efficiency in the passband as a result of a thicker active layer. ΔB=42.52 nm and $\Delta\lambda_{60}$=42.46 nm. Hence, the optimum angular bandwidth is found by choosing the optimum thickness of the active layer. Examining the quantum efficiency at off-resonance, higher quantum efficiency is also obtained – 0.2 in this case, thereby quantum efficiency at off-resonance increases with the increase of the active layer, which is undesirable. Summarizing, the field of view is determined by the trade-off between the bandwidth and quantum efficiency at off-resonance of the RCE photodiode.

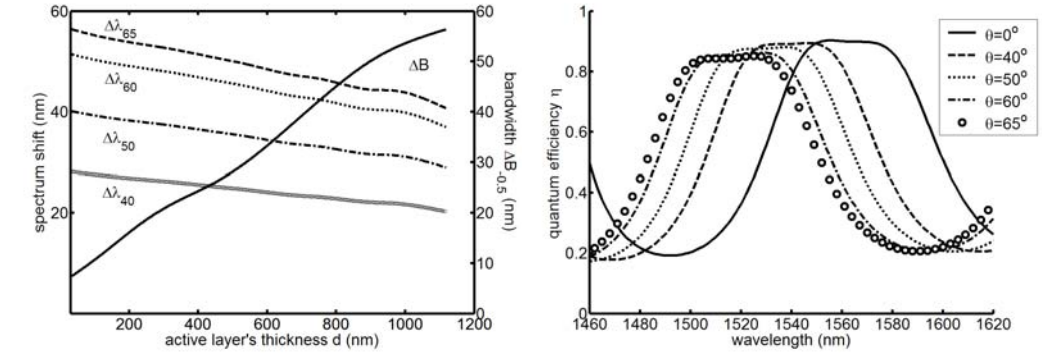

(a) (b)

Fig. 5-8 (a) The effect of the active layer's thickness on the amount of the spectrum shift Δλ with different incident angle variations and the flatness bandwidth (b) Angular dependency of a RCE PD design with the structure $H_2L(HL)^qH_1(LH)^pLS_1CS_2M_2$, where L=91.3, H=139.4, H_1=475.6, H_2=88.9 , C=753 and S_1=182.1 nm

5.5 Conclusion

We have theoretically demonstrated a RCE InGaAs PIN PD with broad spectrum and high quantum efficiency. By substituting an AD mirror for standard Bragg mirror as the entrance mirror and controlling the slope of the round trip inside the active layer, both a flat-top passband and high quantum efficiency can be achieved. By investigating a one-defect AD mirror, we find that the spectral bandwidth of a RCE PD is determined by the width of the AD region of the mirror. In addition, not only the maximum of quantum efficiency but also the spectral bandwidth increases as the active layer's thickness increases. The spectral bandwidth can be engineered by introducing a high-order spacer to the cavity of the AD mirror and increasing the thickness of the spacer S_1 to high order.

The enhancement of the field of view is roughly 2~3° with 0.45~2.33 variations for the optical thickness of the AD mirror made by InAlGaAs/InAlAs systems, and less angular sensitivity is achieved by increasing the thickness of the active layer as a consequence of broadening the bandwidth of the photodiode to compensate for the spectrum shift, but thereby increasing the quantum efficiency at off-resonance. Trade-off between bandwidth, spectrum shift and quantum efficiency at off-resonance limits the field of view of the device. The field of view of the devices is determined by the active layer's thickness for the low index-contrast mirrors, and high-contrast mirror would be a good approach not only to minimize the total thickness devices, but also to reduce the angular sensitivity by optimally choosing the optical thickness ratio of the dielectric mirrors.

5.6 Acknowledgements

The text of this chapter, in part or in full, is a reprint of the material as it appears in the Applied Optics [17]. The dissertation author was the primary researcher and/or the co-authors listed in this publication directed and supervised the research which forms the basis for this chapter.

References

[1] K Kishino, MS Unlu, J-I Chyi, J Reed, L Arsenault, and H Morkoc, "Resonant cavity-enhanced (RCE) photodetectors," IEEE J. Quantum Electron.27, 2025-34 (1991).

[2] MS Unlu, K Kishino, HJ Liaw, and H Morkoc, "A theoretical study of resonant cavity-enhanced photodetectors with Ge and Si active regions," J. Appl. Phys.71, 4049-58 (1992).

[3] MS Unlu, and S Strite, "Resonant cavity enhanced photonic devices," J. Appl. Phys.78, 607-39 (1995).

[4] K Liu, Y Huang, and X Ren, "Theory and experiments of a three-cavity wavelength-selective photodetector," Appl. Opt. 39, 4263-9 (2000).

[5] H-H Tung, and C-P Lee, "Design of a resonant-cavity-enhanced photodetector for high-speed applications," IEEE J. Quantum Electron. 33, 753-60 (1997).

[6] F. Y Huang, A Salvador, X Gui, N Teraguchi, and H Morkoc, "Resonant-cavity GaAs/InGaAs/AlAs photodiodes with a periodic absorber structure," Appl. Phys. Lett. 63, 141-143 (1993).

[7] A Srinivasan, S Murtaza, J. C Campbell, and B. G Streetman, "High quantum efficiency dual wavelength resonant-cavity photodetector," Appl. Phys. Lett. 66, 535-537 (1995).

[8] B Temelkuran, E Ozbay, J. P Kavanaugh, G Tuttle, and K. M Ho, "Resonant cavity enhanced detectors embedded in photonic crystals," Appl. Phys. Lett. 72, 2376-2378 (1998).

[9] Y. H Zhang, H. T Luo, and W. Z Shen, "Study on the quantum efficiency of resonant cavity enhanced GaAs far-infrared detectors," J. Appl. Phys. 91, 5538-5544 (2002).

[10] C Li, Q Yang, H Wang, J Yu, Q Wang, Y Li, J Zhou, H Huang, and X Ren, "Back-incident SiGe-Si multiple quantum-well resonant-cavity-enhanced photodetectors for 1.3-μm operation," IEEE Photon Technol. Lett. 12, 1373-1375 (2000).

[11] A Thelen, Design of optical interference coatings (McGraw-Hill, New York, 1989)

[12] YV Troitski, "Dispersion-free, multiple-beam interferometer," Appl. Opt. 34, 4717-22 (1995).

[13] E.D. Palik, *Handbook of optical constants of solids*, Volume I, III, (Academic, New York, 1998).

[14] W Kowalsky, and J Mahnss, "Monolithically integrated InGaAlAs dielectric reflectors for vertical cavity optoelectronic devices," Appl. Phys. Lett. 59, 1011-12 (1991).

[15] Y. Y Troitski, "Dielectric mirrors with the anomalous dispersion of the reflection phase," Optics and Spectroscopy 77, 503-506 (1994).

[16] H. A Macleod, *Thin-film optical filters*, 3rd ed. (Institute of Physics, Philadelphia, 2001).

[17] Chyong-Hua Chen, Kevin Tetz, and Y Fainman, "Resonant-cavity-enhanced PIN photodiode with broad quantum efficiency spectrum by use of an anomalous dispersion mirror," Appl. Opt. 44(29), 6131-6140 (2005)

Chapter 6 Fabrication and Characterization of a RCE PD

6.1 Introduction

In Chapter 5 , we discussed how to design a RCE photodiode with a flat-top quantum efficiency spectrum and explored the angular sensitivity of the design. In this chapter, we present the fabrication and characterization of this back-illuminated PD. In Section 6.2 , we show the effects of variations of design parameters, e.g. variation of absorption coefficient, accuracy of the properties of materials to the performance of this RCE PD. In Section 6.3 , we briefly describe the manufacture process and characterize the growth epitaxial layers. In Section 6.4 , we characterize the performance of the fabricated devices and compare the measurements to our numerical predictions. The summary is provided in Section 6.5 .

6.2 Sensitivity of the design

Under practical conditions, the discrepancy between the ideal design and fabricated device predominantly results from imperfect materials, inaccurate thickness growth, etc. In the following, we discuss the sensitivity of our design on these possible factors for a RCE PD with the structure of $H_2L(HL)^qH_1(LH)^pLS_1CS_2M_2$ with p=13, q=7, H_1=249.0 nm, H_2=69.7 nm and S_1=355.8 nm.

A. Absorption coefficient of the active layer

The variation of α primarily affects the value of $r_2e^{-\alpha d}$, and results in mismatching our second optimization condition, $r_1=r_2e^{-\alpha d}$ at λ_o. Fig. 6-1 shows that maximum quantum efficiency increases as α increases. However, by calculating the optimized

maximal quantum efficiencies with α=0.8x10^4, 1.0x10^4 and 1.2x10^4 cm^{-1}, we find that the values obtained at λ_o in the case of α=0.8x10^4 and 1.2x10^4 cm^{-1} are slightly smaller than those calculated under the optimized conditions. In addition, the bandwidth of the quantum efficiency is reduced as α increases. In the case of α=0.8x10^4 cm^{-1}, a broader passband with ripples inside is obtained. The ripples occur at the wavelength where $r_1=r_2e^{-\alpha d}$. In contrast, for the case of α=1.2x10^4 cm^{-1}, we observe a rounded passband due to the fact that there is no intersection between r_1 and $r_2e^{-\alpha d}$.

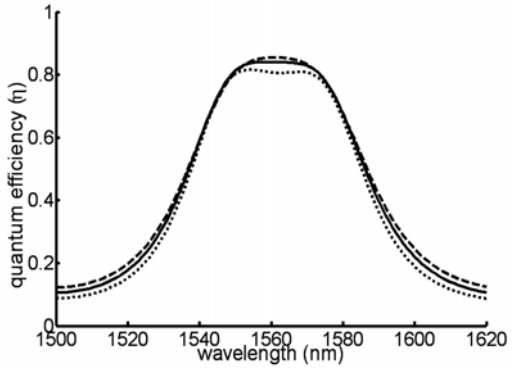

Fig. 6-1 Quantum efficiency vs. absorption coefficient: α=1.2x10^4 cm^{-1} (dashed line), 1x10^4 cm^{-1} (solid line), and 0.8x10^4 cm^{-1} (dotted line)

B. Refractive indices and thickness of dielectric layers

Next we discuss the sensitivity of our design on the variations of refractive indices and the thicknesses of the dielectric mirror M_1. The refractive indices of the materials with alloy compositions vary with the concentration of the content [1]. Fig. 6-2 shows the spectra of r_1 with various values of InGaAlAs ($n_{InGaAlAs}$) and InAlAs (n_{InAlAs}), and the corresponding quantum efficiency spectra. We see that the quantum efficiency spectra shift to shorter wavelength as the refractive index of InGaAlAs ($n_{InGaAlAs}$) or InAlAs (n_{InAlAs}) decreases, because decreasing n_{InAlAs} or $n_{InGaAlAs}$ results in the reflectance

spectra of M_1 shifting to shorter wavelength. In addition, decreasing n_{InAlAs} results in the increases of the reflectance of M_1, and thus the spectrum of quantum efficiency has a narrower and rounded shape due to the absence of an intersection between r_1 and $r_2e^{-\alpha d}$. In contrast, the reflectance of M_1 decreases as a result of the decrease of $n_{InGaAlAs}$, and hence the broad quantum efficiency spectrum with ripples is obtained due to two intersected points between r_1 and $r_2e^{-\alpha d}$.

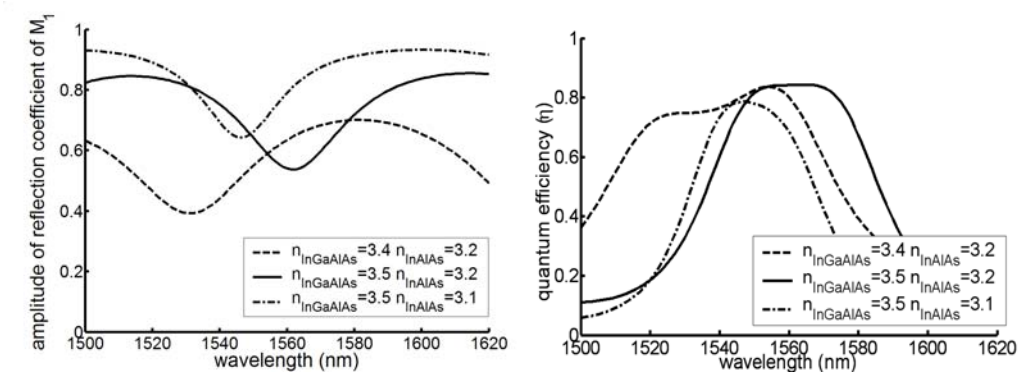

(a) (b)

Fig. 6-2 Effect of variations in the refractive indices of InGaAlAs and InAlAs materials (a) The amplitude of the reflection coefficients r_1 with the variations of $n_{InGaAlAs}$ and n_{InAlAs}. (b) The quantum efficiency with corresponding values of $n_{InGaAlAs}$ and n_{InAlAs}.

Next, we consider the effect of thickness variations of the dielectric mirror M_1, and the calculated quantum efficiency with ±3% deviation of InGaAlAs and InAlAs layer thicknesses are shown in Fig. 6-3. As either InGaAlAs or InAlAs layers' thicknesses increase, the quantum efficiency shifts to shorter wavelengths due to the decrease of the total optical thickness of the device. In addition, the shape of spectrum is distorted as the variation extends, where the distortion is attributed to the mismatch of the first condition. We also observe that the distortion resulting from variations of InGaAlAs layers is worse than that of InAlAs layers because deviation of the total phase Φ caused by variations of InGaAlAs layers is larger than that of InAlAs layers due to $n_{InGaAlAs}>n_{InAlAs}$. In summary,

we find that when our first optimization condition is not satisfied, it leads to distortion of the spectrum and smaller quantum efficiency. In addition, this design is more sensitive to the refractive index variations of M_1 than its thickness variations.

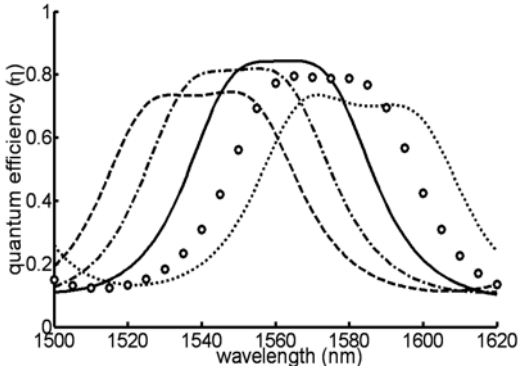

Fig. 6-3 Quantum efficiency with different thickness of InAlAs and InGaAlAs layers with 97% variation of InAlAs layer and 100% of InGaAlAs layer (dashed line), 100% variation of InAlAs layer and 100% of InGaAlAs layer (solid line), 103% variation of InAlAs layer and 100% of InGaAlAs layer (dotted line), 100% variation of InAlAs layer and 97% of InGaAlAs layer (dash-dotted line), and 100% variation of InAlAs layer and 103% of InGaAlAs layer (circle).

6.3 Fabrication and characterization of epitaxial layers

The RCE PD with the structure of $H_2L(HL)^qH_1(LH)^pLS_1CS_2M_2$ with p=13, q=7, H_1=249.0 nm, H_2=69.7 nm and S_1=355.8 nm was fabricated using metal-organic chemical vapor deposition (MOCVD) on a semi-insulating (SI) InP substrate. Due to back-illumination, we add a 2-layer anti-reflection (AR) coating using SiO_2 (n=1.45) and SiN (n=2.0) with 149.7 and 134.7 nm in the thicknesses of SiO_2 and SiN, respectively [16]. The growth multilayer structure is shown in Fig. 6-4(a).

Before evaporating the metallic layers, the reflectance spectra of these epitaxial layers are characterized and shown in Fig. 6-4(b). We find that the measured spectrum roughly shifted 10 nm to shorter wavelengths, compared to the designed calculation. In addition, the resonance dip at 1550 nm is slightly narrower than the designed. The fitted

line is the simulation results obtained by including the dispersion of refractive indices for all the materials, and using correcting factors of 1.02 on InAlAs layer thickness, 0.98 on the thickness of InGaAlAs layers, 0.998 on n+ and p+-InP layer, and 1.02 on i-InGaAs layer. The parameters are chosen to fit the measured spectrum from 1500 to 1600 nm.

Au	500 nm
Ti	5 nm
p+ InP	294.4 nm
i-InGaAs	467.6 nm
n+ InP	355.8 nm
InGaAlAs	139.4 nm
InAlAs x13	91.3 nm
InGaAlAs	249.0 nm
InAlAs	91.3 nm
InGaAlAs	139.4 nm
InAlAs x6	91.3 nm
InGaAlAs	69.7 nm
S.I. InP substrate	
SiN	134.7 nm
SiO_2	149.7 nm

(a)

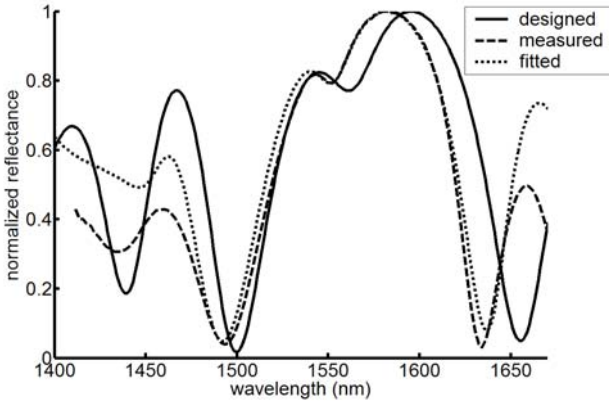

(b)

Fig. 6-4 (a) Schematic diagram of the layers of the fabricated device (b) Normalized reflectance spectra of the design results (solid line), measured data (dashed line) and optimization results by fitted reflectance spectrum from 1500 to 1600 nm (dotted line). The measurement and calculation is taken by looking from the epitaxial side to the substrate without evaporation and the substrate-side is unpolished.

Because the cutoff wavelength of an InGaAs photodiode is roughly 1650 nm, the acquired reflectivity is slightly smaller than the actual values as a result of the discrepancy between the fitted and measured data. In addition, due to the high loss of InGaAlAs in 1450 nm spectrum, the introduction of an absorption coefficient is necessary to obtain accurate information. Here, the absorption coefficient of InGaAlAs is assumed to be 10^4 and 10 cm^{-1} at the wavelengths of 1450 and 1550 nm, respectively, with an exponential dispersion equation, and reflectance is expectedly reduced.

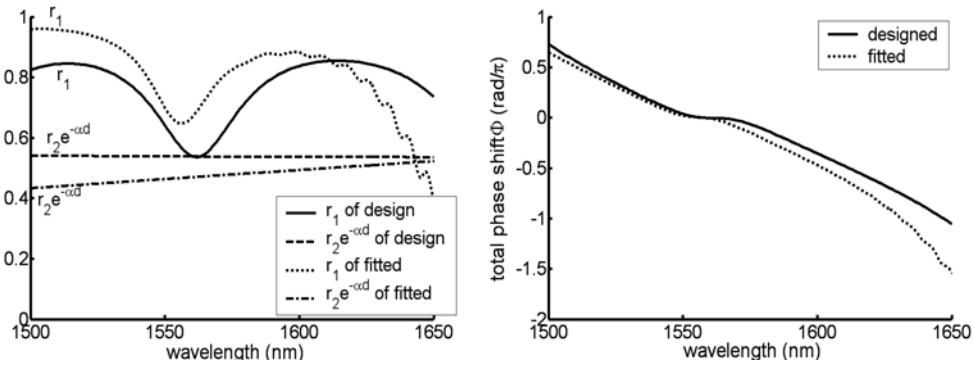

(a) (b)

Fig. 6-5 (a)The relation of the conditions (2). Solid and dashed lines present r_1 and $r_2e^{-\alpha d}$ of the design, respectively, whereas dotted and dash-dotted lines are those calculated by the optimized parameters obtained by fitting the reflectance spectrum in Fig. 6-4(b). (b) total phase shift Φ

Fig. 6-5(a) and (b) show r_1, $r_2e^{-\alpha d}$ and Φ calculated by the design parameters and the optimized parameters fitted to the reflectance spectrum. As shown, we find that $r_2e^{-\alpha d}$ has a smaller value than expected and is not constant due to the dispersion of the active layer. In addition, the spectrum of r_1 shifts to 1550 nm with higher value than expected. Hence, our second optimization condition is not perfectly satisfied. The spectrum of the total phase Φ is similar to that of the design except its shift by 10 nm to shorter wavelength. Therefore, we expect that smaller maximum and rounded and narrower bandwidth would be obtained, similar to the performance obtained in the previous discussion of the sensitivity due to refractive index variations.

6.4 Characterizations

A. Quantum efficiency

Two experiments based on different optical sources were carried out to acquire the quantum efficiency spectrum of the devices. To study the electrical and optical performances of devices, first we use the laser as an input source to characterize the

fabricated devices. Fig. 6-6 depicts the scheme of the photo-response measurement apparatus. A 1520-1570nm-range tunable laser source is coupled to a single-mode fiber and light is delivered to the devices by fiber. Needle probes mounted on translation stages were contacted to the devices to characterize the photo-electronic properties of the photodiode. Above the photodetector, a microscope and an infrared CCD camera are located to image the photodetector.

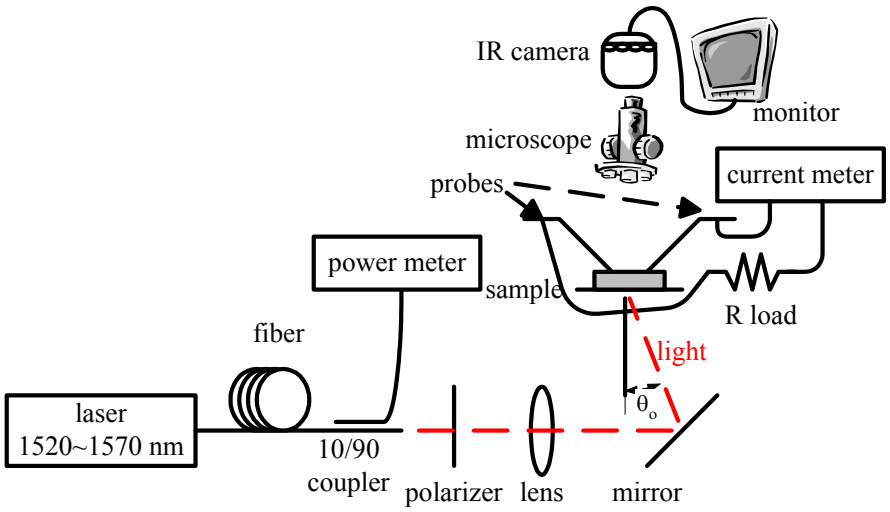

Fig. 6-6 Schematic arrangement of photodetector characterization

Fig. 6-7(a) shows the experimental quantum efficiency spectrum measured at 4.5V reverse bias under a 5-dBmW optical input power. The peak quantum efficiency is 0.8 at the wavelength of 1550 nm. Next, we characterized the photocurrent variations with different reverse bias voltages and input optical powers at the wavelength of 1550 nm, and the results are shown in Fig. 6-7(b). As seen, the photocurrent was reaching saturation as the bias voltage increases to several volts with constant input power as a result of full depletion of the active layer. In addition, with a bias voltage of -4.3 V or larger, a linear photoresponse is obtained up to the optical power of 6.9 dBmW -the

maximum power obtained from the laser. The photocurrent of 3.2 mA is achieved at 6.9-dBmW optical power.

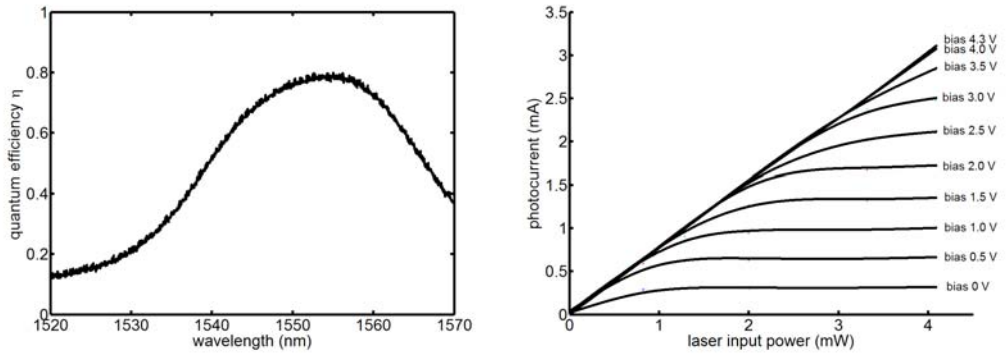

(a) (b)

Fig. 6-7 (a) Experimental quantum efficiency spectrum of the fabricated photodiode and (b) measured photocurrent as a function of the optical input laser power with variation of reverse biases at the incidence wavelength of 1550 nm.

The other method to obtain the photocurrent is to utilize a tungsten-halogen light source, spectrally resolved with a scanning monochrometer, with the signal detected by standard lock-in techniques, whose schematic setup diagram is shown in Fig. 6-8. The benefit of this method is to obtain the photoresponse to the whole wavelength spectrum, and Fig. 6-9 indicates the quantum efficiency spectra of the design calculated by use of Eq. (5.4), the measured data in the bias-free cases, and the simulation using parameters in the fitted case from Fig. 6-4(b) and calculated by Eq.(5.3). As shown in Fig. 6-9, the designed PD possesses high quantum efficiency at 1560 nm with the value of 0.84. In addition, FWHM of the quantum efficiency is about 54.7 nm and the 0.02 dB drop bandwidth is 13.3 nm. The measured data shows the peak quantum efficiency at 1550 nm is 0.80, and FWHM is 36.0 nm and the width of the 0.02 dB drop is 3.4 nm, which both are smaller than designed results but in relatively good agreement with results calculated using parameters fitted to the reflectance spectrum.

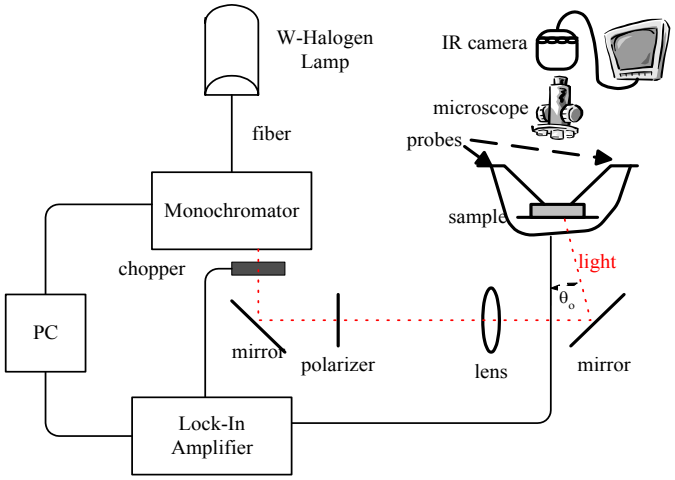

Fig. 6-8 Schematic characterization setup to measure the whole spectrum response of the photodiode.

Apart from the peak at 1550 nm, another peak at 1657 nm was observed as well. The bandwidth of the 0.02dB drop is 2.3nm. Compared with the width at 1550 nm, this implicitly illustrated that a broader spectrum of quantum efficiency was obtained by replacing the conventional first mirror with an AD mirror, even though the flat top conditions were not exactly achieved. Additionally, the inconsistency of calculated results and measured data at the 1450 nm spectrum region results from the bandgap wavelength of InGaAlAs at 1450 nm [2] with the composition of $In_{0.531}Ga_{0.417}Al_{0.052}As$, as a consequence of obtaining the highly absorptive mirrors for the wavelength less than 1450 nm spectrum, and a demonstrated simulations with absorption for InGaAlAs layers (shown as dotted line in Fig. 6-9) shows dramatic reduction of quantum efficiency in the 1450 nm spectrum.

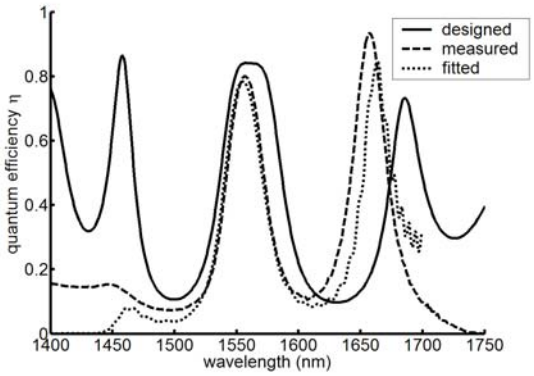

Fig. 6-9 Quantum efficiency of the design (solid line), measured (dashed line) and calculated by optimized parameters obtained by fitting the reflectance spectrum (dotted line)

B. Angular sensitivity

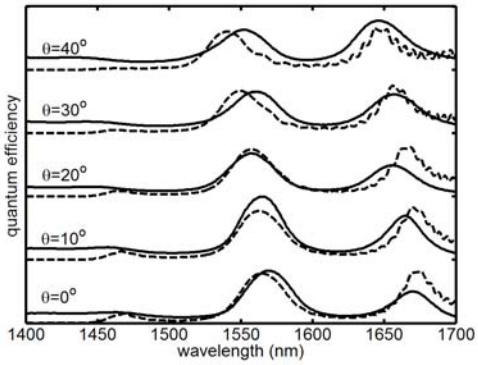

Fig. 6-10 Quantum efficiency spectra of the measured (solid line) and calculated by optimized parameters (dashed line) for different incidence angles

Fig. 6-10 shows the quantum efficiency spectra with the variations of incident angles by adjusting the angles of the mirror below the stage of the measurement setup in Fig. 6-8 and the calculated spectra using parameters in the fitted case from Fig. 6-4(b). The amount of spectrum shift is roughly 17.54 nm as the incident angle tilts from 0 to 40°, approximately in agreement with the calculated results. Examining the measured peak power at the 1550 nm spectrum, we found that the power randomly varied as angle increased, and speculated it was a consequence of non-uniform AR coatings on the other side of the substrates and unfocused beam impinging on the samples.

C. Frequency response

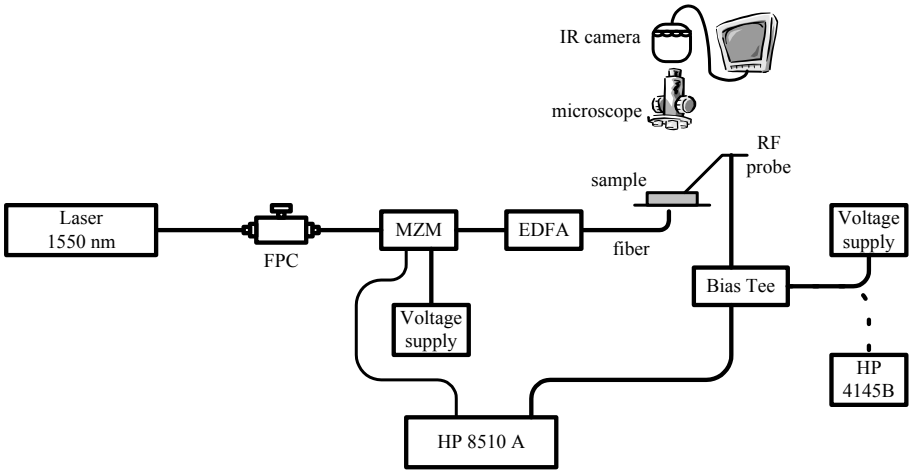

Fig. 6-11 Measurement setup to characterize frequency response of photodetector. FPC is fiber polarization controller, MZM is Mach-Zehnder modulator, and EDFA is Erbium doped fiber amplifier

Frequency response was carried out with a HP8510A network analyzer in the frequency range from 30MHz to 15 GHz at 1550 nm wavelength by measuring the S_{21} parameter. Fig. 6-11 depicts the characterization apparatus. In the optical part, the laser operated at 1550 nm was connected to a fiber polarization controller (FPC) to control the polarization state of the laser. The light was delivered to a 15GHz Mach-Zehnder modulator (MZM) to modulate the input signal and the FPC was adjusted to maximize the output power of MZM. Due to the high insertion loss of the MZM, an Erbium doped fiber amplifier (EDFA) was connected to the output of MZM. A bare fiber was connected to the EDFA and the device was illuminated via the other end of the fiber. The device was put on the translation stage and contacted by microwave probes of 50-Ω characteristic impedance and biased through a bias tee. The input of the MZM was connected to the input port of an HP8510A networking analyzer and the coaxial wire from the bias tee was connected to the output port of the HP8510A.

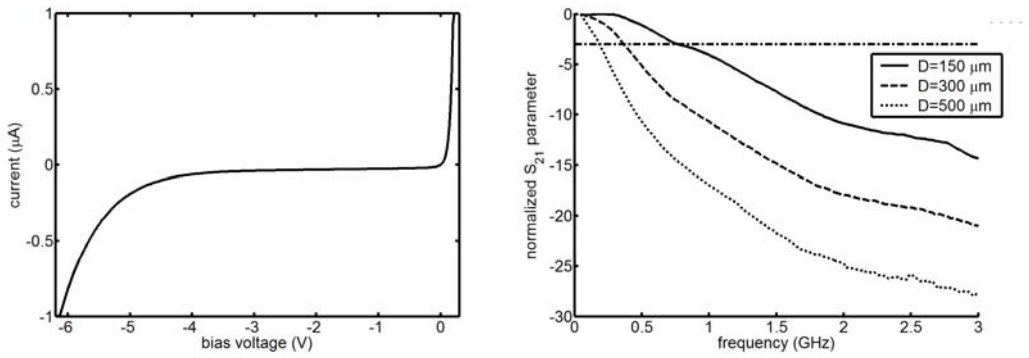

(a) (b)

Fig. 6-12 (a) I-V curve of the fabricated photodiode and (b) frequency response of the photodiode with the devices' sizes of 150 (solid line), 300 (dashed line) and 500 μm (dotted line)

First, a HP4145B semiconductor parameter analyzer was connected to the bias tee to measure the I-V curve of the photodiode with the results shown in Fig. 6-12(a). We found that the cutoff voltage, defined as the voltage at the reverse current 10^{-6} A, is –6.3V. Next, the wire was connected to a voltage supply with reverse bias 2 V. Before starting to obtain frequency response of the photodiodes, we used calibration kits to calibrate the whole system. The measured frequency responses with different sizes of devices are shown in Fig. 6-12(b). The bandwidth of these devices with the diameters of 150 μm, 300 μm, and 500 μm are 0.7514, 0.3714, and 0.1987 GHz, respectively.

Theoretically, the speed of photodiodes is mainly limited by transit time which is the drift time across the depletion region and RC time which is the charging and discharging times of inherent and parasitic capacitances. The bandwidth of the device f_{3dB} can roughly be express as [3]

$$f_{3dB}^{-1} = 0.45\left(\frac{d}{v_h + v_e}\right) + \frac{2\pi R_L \varepsilon_a A}{d} \quad \text{.....(6.1)}$$

where d is the thickness of the depletion region. v_h and v_e are the hole and electron velocities, respectively. ε_a is the permittivity of the depletion layer, A is the area of the

device, and R_L is the total resistance. Fig. 6-13 shows the theoretical simulation by Eq.(6.1) and the measured bandwidth with different sizes of devices. We find that bandwidth significantly decreases with the sizes of devices. In our devices, the transit time is roughly 9.26 fsec, and RC time is 1.38 nsec for device's diameter of 150 μm; hence, for large size devices, such as our devices, the limitation of speed is dominated by RC constant bandwidth. In addition, the measured data are slightly larger than the theoretical values probably due to undercut etching of the top mesa, thereby obtaining a smaller device capacitance.

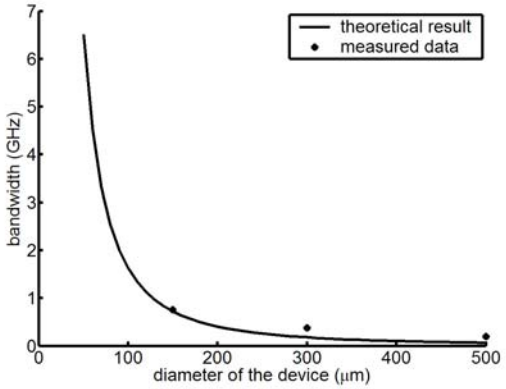

Fig. 6-13 Bandwidth with variations of sizes of devices. Asterisk (*) denotes the measured data and solid line shows theoretical results.

6.5 Conclusion

A design with a maximum quantum efficiency of 0.84, FWHM 54.7 nm and field of view of 40° is presented, fabricated and characterized. Experimental results with maximum quantum efficiency of 0.80 and FWHM of 36.0 nm were obtained. The mismatch between the simulated design and the actual device is due to the fabrication error of the layer thickness growth and neglecting the materials' dispersion in the design. The spectrum shift is 17.54 nm as incident angle is varied from 0 to 40°, and the field of

view is reduced due to the non-flat-top transmission band obtained. The bandwidth of 0.75 GHz is obtained as the diameter of the device is 150 μm and the increase of speed could be achieved by reducing the size of the photodiode.

6.6 Acknowledgements

The text of this chapter, in part or in full, is a reprint of the material as it appears in the Applied Optics [4]. The dissertation author was the primary researcher and/or the co-authors listed in this publication directed and supervised the research which forms the basis for this chapter.

References

[1] MJ Mondry, DI Babic, JE. Bowers, and LA Coldren, “Refractive-indexes of (Al, Ga, In) As epilayers on InP for optoelectronic applications,” IEEE Photon Technol. Lett. 4,627-630 (1992)

[2] W Kowalsky, and J Mahnss, “Monolithically integrated InGaAlAs dielectric reflectors for vertical cavity optoelectronic devices,” Appl. Phys. Lett. 59, 1011-12 (1991).

[3] M. S. Unlu, S. Strite, “Resonant cavity enhanced photonic devices,” J. Appl. Phys. 78 (2), 607-639 (1995).

[4] Chyong-Hua Chen, Kevin Tetz, and Y Fainman, “Resonant-cavity-enhanced PIN photodiode with broad quantum efficiency spectrum by use of an anomalous dispersion mirror,” Appl. Opt. 44(29), 6131-6140 (2005)

Chapter 7 Compact and Integrated TM-pass Waveguide Polarizer

7.1 Introduction

Optical waveguide polarizers are essential components in integrated photonics, especially for devices and systems operating with a single polarization (SP) such as fiber-optic gyroscopes, electro-optic switching arrays, coherent optical communication modules and more. The functionality of optical waveguide polarizers is to allow only one polarization state (TE or TM) to propagate while the other polarization state is eliminated. A good polarizer is characterized by low insertion loss and high extinction ratio. Many types of waveguide polarizers have been realized over the years, including, for example, metal-clad waveguides [1]-[4] and birefringence waveguides [5],[6], but few of them are TM-pass types. One class of such polarizers is based on using a metal-cladding layer with either a grating [7],[8] or a nanocomposite structure [9] to absorb the propagating TE polarization wave. However, the propagation loss of these devices is relatively high. A different concept is using a polarization splitter structure such as a directional coupler to split TE and TM modes into horizontal or vertical integrated waveguides [10], but for either of these cases complex and specific structures need to be used. Devices based on deposition of birefringent materials or form birefringent multilayers have been proposed as well, where TE polarization is eliminated due to different TE and TM cutoff wavelengths [11],[12]; but unfortunately a relatively long distance (usually several millimeters) is needed to achieve a high extinction ratio.

It is well known that most waveguide devices are polarization dependent due to the different boundary conditions for each polarization [13],[14]. Typically, TE and TM modes propagate with slightly different propagation constants. The birefringence increases as the structure has an abrupt index change and geometrical variations, e.g. slot waveguides [15]. These types of birefringent waveguides have been demonstrated for mostly air guiding of the TE-like mode. In this paper, we propose a novel TM-pass waveguide polarizer based on geometry-induced birefringence. Our device is based on introducing a slot into the waveguide, operating as a directional coupler that produces high birefringence. By proper design, the waveguide confines only TM modes, i.e. a SP waveguide is achieved. With integration of Y-branch mode-converted waveguides, a high extinction ratio and low loss TM-pass polarizer is realized. The proposed device is based on a GaAs ridge waveguide on top of an AlAs layer, although the concept can be easily applied to other material systems, e.g. silicon on insulator (SOI) and polymer waveguides. By using the 3-D semivectorial FDTD method [16], a numerical study of this polarizer is carried out. The simulation results indicate that an extinction ratio of 20.3 dB and an insertion loss of 0.54 dB can be obtained with a device length of 26 μm at a wavelength of 1.55 μm.

7.2 Design of a TM-pass waveguide polarizer

The proposed device is composed of identical input and output waveguides and a TM-pass polarizer in between. The device consists of GaAs (n=3.374) as a guiding layer and AlAs (n=2.95) as a substrate layer. The input and the output sections are designed as single-mode ridge waveguides operating at 1.55 μm wavelength. Let the width of the

waveguide be W=1 μm and its height be H=0.5 μm. The effective indices of TE_{00} and TM_{00} modes calculated by the semivectorial finite difference (FD) method with Dirichlet boundary conditions [17] are 3.119 and 3.085, respectively.

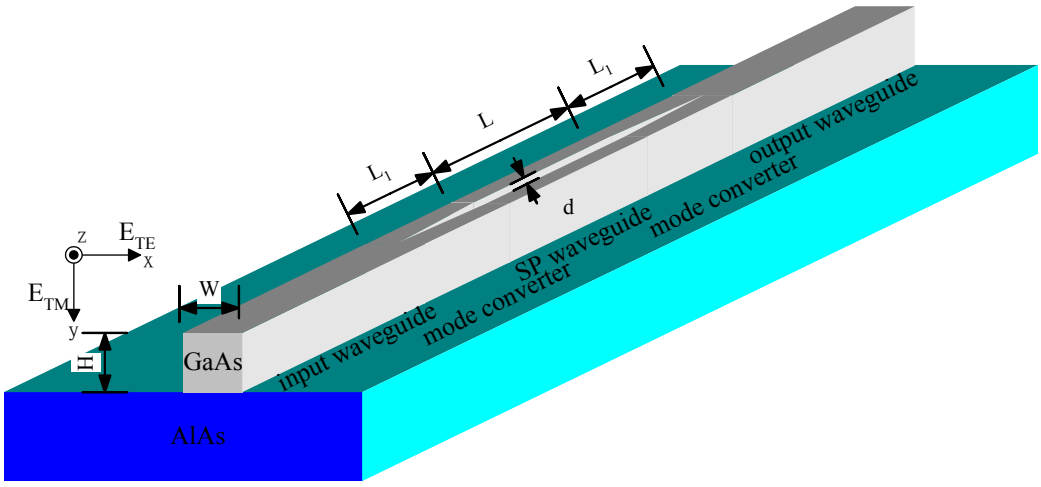

Fig. 7-1 The schematic structure of the TM-pass polarizer. The input and output waveguides are ridge waveguides with width W and height H. A TM-pass SP waveguide is a ridge waveguide with the same size of input and output. A slot filled with air is centered at the SP waveguide with width d and length L. Y-branch mode-conversion waveguides are between input/output and SP waveguides with the length of L_1.

The TM-pass polarizer consists of a TM-like SP waveguide sandwiched between two identical mode-converters. A schematic drawing of the proposed design is shown in Fig. 7-1 with L_1 being the length of the mode converter, L being the length of the TM-like SP waveguide and d being the distance between the two parallel waveguides.

First, we investigate the polarization dependence of the SP waveguide shown in Fig. 7-1. The width of each ridge waveguide is w_1. Its height is H, same as the input and output (I/O) waveguides, i.e. 0.5 μm. The separation between the two waveguides is d, and the total width is $d+2w_1=W$. The cross-section of the proposed SP waveguide structure (onset) and effective indices of the lowest TE-like and TM-like modes of this waveguide versus d are shown in Fig. 7-2. The results clearly indicate that effective

indices for the two polarization modes decrease as d increases. However, the effective index of the TE-like mode (dashed line) decreases much faster than that of the TM-like mode (solid line). No guided mode for the TE polarization is supported as d >0.02 μm, while a guided TM-like mode is sustained as long as d <0.14 μm. Therefore, if the separation distance d is between 0.02 and 0.14 μm, a TM-like SP waveguide can be realized.

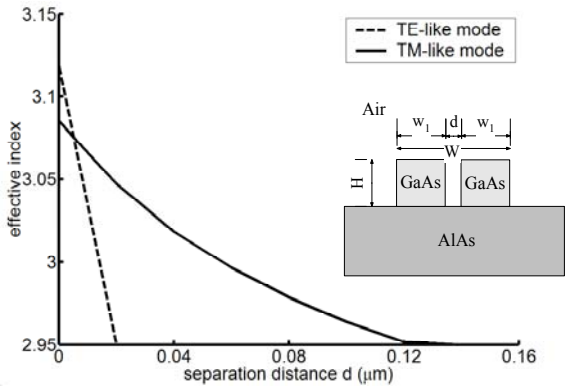

Fig. 7-2 Effective indices for the lowest TE-like (dashed line) and TM-like (solid line) modes of the SP waveguide versus different separation distance d. The inset shows the cross-section of the simulated SP waveguide.

The field distributions of the fundamental TM modes for the input and the SP waveguides with d=0.1 μm are shown in Fig. 7-3. Since the TM field is localized within the high-index region, there is a significant mode mismatch between the I/O waveguides and the SP waveguide, giving rise to substantial insertion loss. The coupling efficiency from the input waveguide to the SP waveguide with d=0.1 μm was found to be 0.86, calculated by the following overlap integral [18] with $E_{in}(x,y)$ and $E_{out}(x,y)$ denoting the mode profiles of the input and the SP waveguides, respectively:

$$g = \frac{\left|\iint E_{in}(x,y)E_{out}(x,y)dxdy\right|^2}{\iint\left|E_{in}(x,y)\right|^2 dxdy \iint\left|E_{out}(x,y)\right|^2 dxdy} \quad \text{.....(7.1)}$$

The coupling loss due to mode mismatch at the interface of the input and the SP waveguides given by $10\log_{10}(g)$ is -0.67 dB. In order to mitigate the coupling loss, we introduce mode conversion sections between the I/O and the SP waveguides. The mode converter allows an adiabatic mode transition from the I/O waveguide sections to the SP waveguide.

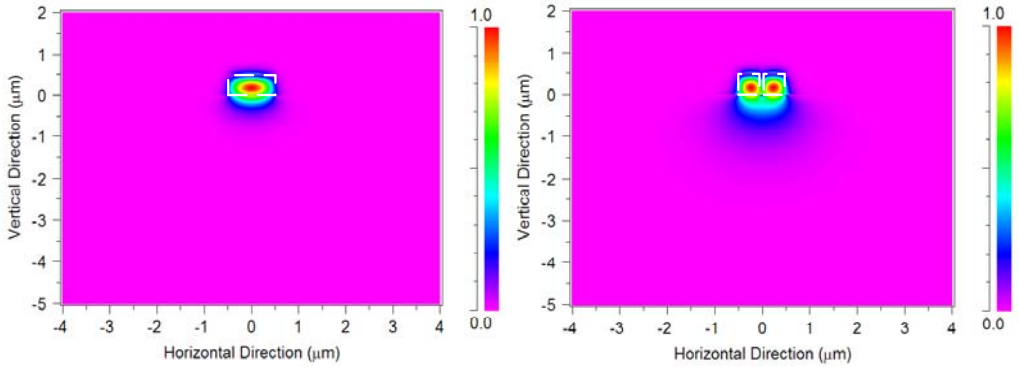

(a)TM_{00} mode of the input waveguide (b) The lowest TM-like mode of the SP waveguide

Fig. 7-3 E_y field profiles of the fundamental TM modes of the input waveguide (left) and the SP waveguide with d=0.1 μm (right). The white dashed line shows the cross section of waveguides.

We use an inner symmetric Y-branch waveguide with length L_1 as a mode converter shown in Fig. 7-1. In Fig. 7-4, we show the effects of the variations of L_1 on the power loss of the incident wave propagating along the structure consisting of an input waveguide, a mode converter with length L_1 μm and the SP waveguide with d=0.1 μm and L=10 μm. The calculated results are obtained by using the 3-D FDTD method with the TM_{00} mode of the input waveguide as the input signal. One can see that the power loss diminishes as L_1 increases. As L_1=0, the power loss is –0.61 dB, slightly smaller than the value predicted by the overlap integral. This is probably because the radiation modes excited by the incident wave do not vanish entirely within 10 μm length of the SP

waveguide. With L_1>3 μm, the mode conversion loss is less than -0.25 dB, which is acceptable for telecommunication applications.

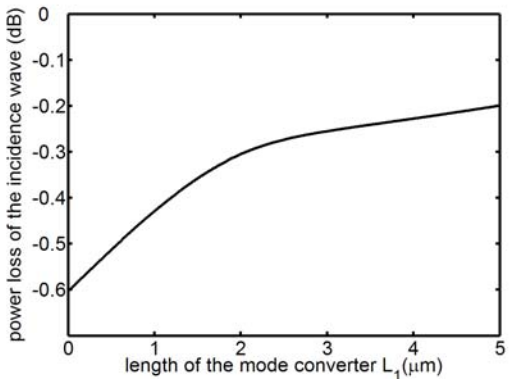

Fig. 7-4 Power loss of the TM_{00} mode incidence wave with variations of the length of the Y-branch waveguide L_1.

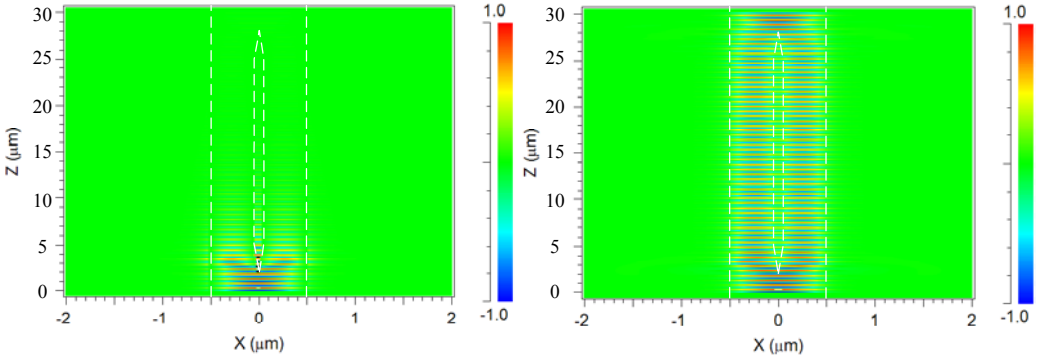

Fig. 7-5 Field distributions of the incidence waves with TE (a) and TM (b) polarizations propagating in the waveguide polarizer.

Fig. 7-5(a) and (b) show the calculated propagation behaviors in the waveguide polarizer with L_1=3 μm, d=0.1 μm and L=20 μm for TE and TM polarizations, respectively. The results are obtained using FDTD with the incident wave at the input waveguide being the fundamental mode for each polarization. As expected, the guided TE-like mode is not supported in the SP waveguide, and thus the TE_{00} mode leaks into the substrate as it propagates through the polarizer. Contrarily, the TM_{00} mode is well

confined in the SP waveguide structure without observable decay of the field power. The overall loss is minimized by the implementation of the mode converter.

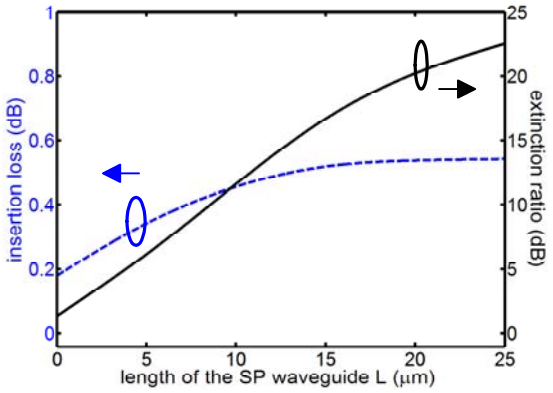

Fig. 7-6 Performance of the proposed TM polarizer with different length of the SP waveguide L. The dashed line is the insertion loss of the whole device and the solid line is the extinction ratio.

Fig. 7-6 shows the calculated insertion loss of the TM polarization and the extinction ratio of the waveguide polarizer as a function of the SP waveguide length L with L_1=3 μm and d=0.1 μm. Here, the extinction ratio of a polarizer is defined as the power ratio of TM_{00} and TE_{00} modes in the output waveguide, i.e. $10\log_{10}(P_{TMo}/P_{TEo})$, where P_{TMo} and P_{TEo} are the power of the TM_{00} and TE_{00} modes in the output waveguide. The insertion loss is defined as the total power loss of the TM_{00} mode in the output waveguide, i.e. $-10\log_{10}(P_{TMo})$. For the TE polarization, the power loss increases with L and becomes larger than 20 dB at L>18.7 μm. On the other hand, for the TM polarization, the power loss of about 0.54 dB is almost invariant with L>15 μm, roughly twice the coupling loss from the mode converter with L_1=3 μm, since the TM-like mode is guided by the SP waveguide structure (scattering loss due to waveguide roughness is neglected due to the short length of the device). As L=20 μm, the device exhibits an extinction ratio of 20.3 dB and an insertion loss of 0.54 dB.

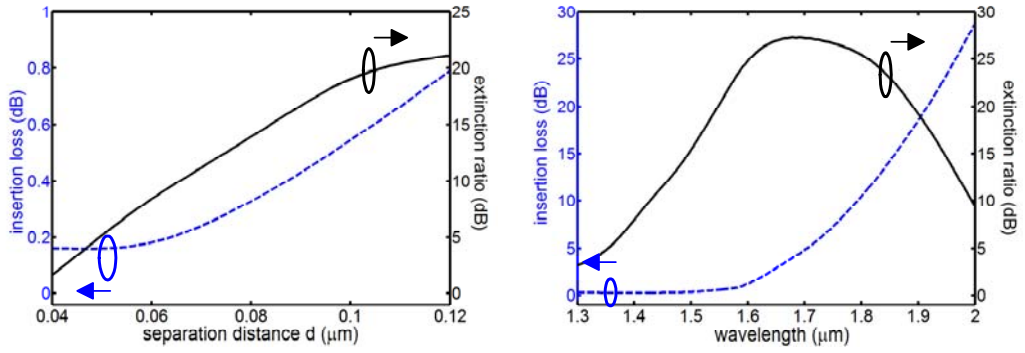

(a) (b)

Fig. 7-7 (a) Insertion loss and extinction ratio of the polarizer with variations of the separation distance d. (b) Insertion loss and extinction ratio as a function of wavelength.

Fig. 7-7(a) shows the effects of the variations of the separation distance d on the insertion loss and on the extinction ratio of the polarizer with L_1=3 μm and L=20 μm. We see that both the extinction ratio and the insertion loss grow with an increase of d. The extinction ratio is increasing with d because the propagation loss of the TE_{00} mode in the SP waveguide is increasing, while the propagation loss for the TM_{00} mode is negligible over the range of 20 μm. On the other hand, mode mismatch between the input and the SP waveguides becomes larger with the increase of d, and consequently the power loss for the TM polarization, predominately resulting from the coupling loss, also increases. This can be compensated by using a longer mode converter (larger value of L_1). The corresponding cutoff wavelengths for the lowest TE-like and TM-like modes of the SP waveguide with d=0.1 μm are 1.32 and 1.61 μm respectively, defining the wavelength region of operation for the proposed device. The wavelength dependency of a typical device with L_1=3 μm, d=0.1 μm and L=20 μm is shown in Fig. 7-7(b), which is calculated by using 3-D FDTD with TE_{00} and TM_{00} modes as the incident waves. One can easily notice that the insertion loss remains approximately constant for wavelength

shorter than 1.61 μm. The extinction ratio shows an optimum around 1.68 μm. This is because the power loss of the TE_{00} mode decreases significantly for shorter wavelengths, while the power loss of the TM_{00} mode increases for wavelength larger than 1.61 μm.

7.3 Conclusions

A TM-pass waveguide polarizer is proposed and analyzed. The device consists of a coupler waveguide section supporting only TM-like modes, and a Y-branch section allowing an adiabatic mode conversion between the input/output waveguides and the SP ridge waveguide. The device is optimized using 3-D semivectorial FDTD method. With a length 20 μm of the SP waveguide and two 3 μm-long Y-branch waveguides, an extinction ratio of 20.3 dB is obtained with the insertion loss on the order of 0.5 dB. Higher extinction ratio can be achieved either by increasing the length of the SP waveguide or by increasing the separation distance with only a slight increase of the insertion loss. In addition, the insertion loss of the device could be reduced either by increasing the length of the mode converter or by reducing the separation distance of the two waveguides.

7.4 Acknowledgements

The text of this chapter, in part or in full, is a reprint of the material as it appears in the Optics Express [19]. The dissertation author was the primary researcher and/or the co-authors listed in this publication directed and supervised the research which forms the basis for this chapter.

References

[1] E. M. Garmire and H. Stoll, "Propagation losses in metal-film-substrate optical waveguide," IEEE J. Quantum Electron. **8**, 763-6 (1972).

[2] W. Johnstone, G. Stewart, T. Hart, and B. Culshaw, "Surface plasmon polaritons in thin metal films and their role in fiber optic polarizing devices," J. Lightwave Technol. **8**, 538-44 (1990).

[3] T. Nakano, K. Baba, and M. Miyagi, "Insertion loss and extinction ratio of a surface plasmon-polariton polarizer: theoretical analysis," J. Opt. Soc. Ame. B **11**, 2030-5 (1994).

[4] C-H Chen, L. Wang, "Design of Finite-length metal-clad optical waveguide polarizer," IEEE J. Quantum Electron. **34**, 1089-97 (1998).

[5] O. Watanabe, M. Tsuchimori, A. Okada, and H. Ito, "Mode selective polymer channel waveguide defined by the photoinduced change in birefringence," Appl. Phys. Lett. **71**, 750-2 (1997)

[6] A. Morand, C. Shanchez-Perez. P. Benech, S. Tedjini, and D. Bosc, "Integrated optical waveguide polarizer on glass with a birefringent polymer overlay," IEEE Photonics Technol. Lett. **10**, 1599-601 (1998)

[7] M. J. BJ. Wang, S. Schablitsky, Z. Yu, W. Wu, and S. Y. Chou, "Fabrication of a new broadband waveguide polarizer with a double-layer 190 nm period metal-gratings using nanoimprint lithography," J. Bac. Sci. Technol. B. **17**, 2957-60 (1999)

[8] M.A. Khan and H.A. Jamid, " Analysis of TM-pass reflection mode optical polarizer using method of lines," in *Proceedings of the 2003 10th IEEE International Conference on Electronics, Circuits, and Systems* (Institute of Electrical and Electronics Engineers, New York, 2003). IEEE. Part Vol.**2**, 555-8.

[9] M. J. Bloemer, and J. W. Haus, "Broadband waveguide polarizers based on the anisotropic optical constants of nanocomposite films," J. Lightwave Technol. **14**, 1534-1540 (1996)

[10] S.K. Kim, K. Geary, D. H. Chang, H.R. Fetterman, H. Zhang, C. Zhang, C. Wang, and W.H. Steier, "TM-pass polymer modulators with poling-induced waveguides and self-aligned electrodes," Electron. Lett. **39**, 721-2 (2003).

[11] K. Baka, T. Iden, and M. Miyagi, “TM-pass glass waveguide polarizer with periodic multilayer cladding overlaid with isotropic dielectric media,” Electron. Lett. **36**, 1461-2 (2000).

[12] S.S. Lee, S. Garner, A. Chen, V. Chuyanov, W. H. Steier, S. W. Ahn, and S-Y Shin, “TM-pass polarizer based on a photobleaching-induced waveguide in polymers,” IEEE Photonics Technol Lett. **10**, 836-8 (1998)

[13] H.A. Haus, W.P. Huang, and A.W. Snyder, “Coupled-mode formulations,” Opt. Lett. **14**, 1222-4 (1989)

[14] P. L. Liu, and B. J. Lin, “Study of form birefringence in waveguide devices using the semivectorial beam propagation method,” IEEE Photonics Technol. Lett. **3**, 913-15 (1991)

[15] V. R. Almeida, Qianfan Xu, C. A. Barrios and M. Lipson, ”Guiding and confining light in void nanostructure,” Opt. Lett. **29**, 1209-11 (2004)

[16] A. Taflove, Computational Electrodynamics: the Finite-Difference Time-Domain Method (Artech House, Boston, 1995).

[17] K. Kawano and T. Kitoh, Introduction to Optical Waveguide Analysis: Solving Maxwell's Equations and the Schrödinger Equation (J. Wiley, New York, 2001).

[18] H. Nishihara, M. Haruna, and T. Suhara, *Optical Integrated Circuits* (McGraw-Hill, New York, 1989).

[19] Chyong-Hua Chen, Lin Pang, Chia-Ho Tsai, Uriel Levy and Y. Fainman, “Compact and integrated TM-pass waveguide polarizer,” Optics Express 13, 5347-5352 (2005) ,http://www.opticsexpress.org/abstract.cfm?URI=OPEX-13-14-5347

Chapter 8 Bandpass Resonant Waveguide Filter with Characteristics of Flat Passband and Wide stopband

8.1 Introduction

High-index contrast photonic bandgap waveguide microcavities are of interest for a variety of applications due to their small sizes and high field confinements [1]-[4]. For optical wavelength division multiplexing applications, compact optical filters with a high quality factor (Q-factor) and selective transmission are desired. For this reason, optical photonic crystal microcavities, such as 1-D photonic crystal mirrors with a defect were analyzed and demonstrated for filtering applications [5]-[7]. However, these filters are inappropriate for systems requiring high transmittance and nearly rectangular passband due to losses of the photonic bandgap mirrors and the Lorentzian filter response of a Fabry-Perot cavity.

In order to enhance the transmission at the desired wavelength, modifications of photonic crystal mirror were carried either by introducing transition mode-matching structures or by tuning the positions of holes at the interface between the photonic crystal mirrors and the cavity [8]-[12]. These approaches utilized the mode matching between the Bloch waves in the photonic bandgap mirrors and the guided modes in the cavity. Implementations of transmission filters with nearly square passband were achieved by introducing multiple resonances (or defects) into the structures and appropriately choosing their locations and dimensions, as demonstrated in [14]-[20]. In this work, we apply the methodology of optical multilayer bandpass filter design to realize a nearly

rectangular optical bandpass waveguide microcavity filter with the benefit of a wide stopband in the spectrum and easy integration with other nanophotonic devices on the same chip. With analogy to the analysis using Smith's method [21], the transmission properties of a microcavity filter are approximately the same as that of the Fabry-Perot resonator as the loss of the photonic bandgap mirror is minimized. Therefore, an AD mirror is required to achieve a flat-top passband [19]-[20]. Hereby an AD mirror implemented by a photonic bandgap monorail waveguide with a one-defect structure is presented. A nearly square bandpass waveguide filter is obtained by having two identical AD mirrors and appropriately choosing the separation length in between to compensate for the phase dispersion of AD mirrors.

The organization of this chapter is as follows: In Section 8.2 we analyze the generalized photonic bandgap waveguide microcavities using the bidirectional eigenmode propagation methods and obtain a formula to describe the transmission properties of the cavities. In Section 8.3 we discuss the design parameters and present an example with high transmission and flat-top passband in the photonic bandgap monorail waveguide microcavities. In addition, numerical results are carried out by using the 3-D FDTD method to numerically validate the design. In Section 8.4 we make the conclusion of this chapter.

8.2 Analysis of photonic bandgap waveguide microcavities

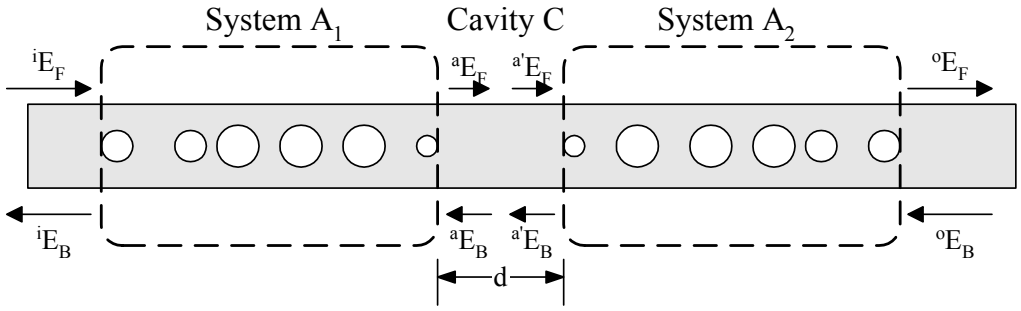

Fig. 8-1 Schematic of a generalized photonic bandgap waveguide microcavity structure

A schematic diagram showing the generalized photonic bandgap waveguide microcavity structure with multiple defects is shown in Fig. 8-1. The structure is divided into two systems, A_1 and A_2, separated by cavity C with the length of d. Let the optical eigenmode fileds $\{{}^{i}E_{gF}, {}^{i}E_{rF}, {}^{i}E_{gB}, {}^{i}E_{rB}\}$, and $\{{}^{o}E_{gF}, {}^{o}E_{rF}, {}^{o}E_{gB}, {}^{o}E_{rB}\}$ denote the forward (F) and backward (B) waves for guided (g) and radiative (r) modes in the input and output regions, respectively. $\{{}^{a}E_{gF}, {}^{a}E_{rF}, {}^{a}E_{gB}, {}^{a}E_{rB}\}$ describe the traveling waves at the interface between cavity C and system A_1, whereas $\{{}^{a'}E_{gF}, {}^{a'}E_{rF}, {}^{a'}E_{gB}, {}^{a'}E_{rB}\}$ represent the traveling waves at the interface between cavity C and system A_2. The relations between $\{{}^{i}E_{gF}, {}^{i}E_{rF}, {}^{i}E_{gB}, {}^{i}E_{rB}\}$, $\{{}^{a}E_{gF}, {}^{a}E_{rF}, {}^{a}E_{gB}, {}^{a}E_{rB}\}$, and $\{{}^{a'}E_{gF}, {}^{a'}E_{rF}, {}^{a'}E_{gB}, {}^{a'}E_{rB}\}$, $\{{}^{o}E_{gF}, {}^{o}E_{rF}, {}^{o}E_{gB}, {}^{o}E_{rB}\}$ can be expressed in the form of the following matrix equations analyzed by using the bidirectional eigenmode propagation method [22]-[24].

$$\begin{bmatrix} {}^{i}E_{gF} \\ {}^{i}E_{rF} \\ {}^{i}E_{gB} \\ {}^{i}E_{rB} \end{bmatrix} = \begin{bmatrix} p_{11} & p_{12} & p_{13} & p_{14} \\ p_{21} & p_{22} & p_{23} & p_{24} \\ p_{31} & p_{32} & p_{33} & p_{34} \\ p_{41} & p_{42} & p_{34} & p_{44} \end{bmatrix} \begin{bmatrix} {}^{a}E_{gF} \\ {}^{a}E_{rF} \\ {}^{a}E_{gB} \\ {}^{a}E_{rB} \end{bmatrix} \quad \text{.....(8.1)}$$

$$\begin{bmatrix} {}^{a'}E_{gF} \\ {}^{a'}E_{rF} \\ {}^{a'}E_{gB} \\ {}^{a'}E_{rB} \end{bmatrix} = \begin{bmatrix} q_{11} & q_{12} & q_{13} & q_{14} \\ q_{21} & q_{22} & q_{23} & q_{24} \\ q_{31} & q_{32} & q_{33} & q_{34} \\ q_{41} & q_{42} & q_{34} & q_{44} \end{bmatrix} \begin{bmatrix} {}^{o}E_{gF} \\ {}^{o}E_{rF} \\ {}^{o}E_{gB} \\ {}^{o}E_{rB} \end{bmatrix} \quad \text{.....(8.2)}$$

$$\begin{bmatrix} {}^{a}E_{gF} \\ {}^{a}E_{rF} \\ {}^{a}E_{gB} \\ {}^{a}E_{rB} \end{bmatrix} = \begin{bmatrix} e^{j\beta_g d} & 0 & 0 & 0 \\ 0 & e^{j\beta_r d} & 0 & 0 \\ 0 & 0 & e^{-j\beta_g d} & 0 \\ 0 & 0 & 0 & e^{-j\beta_r d} \end{bmatrix} \begin{bmatrix} {}^{a'}E_{gF} \\ {}^{a'}E_{rF} \\ {}^{a'}E_{gB} \\ {}^{a'}E_{rB} \end{bmatrix} \quad \text{.....(8.3)}$$

where p and q are transfer elements of the modes for system A_1 and A_2, respectively. β_g and β_r are the corresponding propagation constants for guided and radiation modes in the waveguide of cavity C.

Suppose that only one guided mode exists in the input waveguide, cavity C and output waveguide, and the structure itself has mirror reflection symmetry with respect to the center of cavity C. The transmitted wave going through the output waveguide is denoted as

$$T = \frac{1}{p_{11}p_{33}e^{j\beta_g d}(1 + p_{31}^2 / p_{11}p_{33}e^{-2j\beta_g d} + h(p_{12}, p_{14}, p_{21}, p_{22}...))} \quad \text{.....(8.4)}$$

where $h(p_{12}, p_{14}, p_{21}, \ldots)$ is a function related to the coupling ratio between the guided mode and radiation mode via the perturbations of the structures. Eq. (8.4) is identical to the transmission expression of a Fabry-Perot cavity if $h(p_{12}, p_{14}, p_{21}, \ldots)=0$.

Referred to Eq. (8.4), the maximum transmission might be less than 1 due to the interactions between the radiation mode of the waveguide and the Bloch wave of the photonic crystal mirrors, resulting in $h(p_{12}, p_{14}, p_{21}, \ldots)\neq 0$. In Fig. 8-2, we show the variations of the maximal transmission (T_{max}) calculated by the formula of $T^2(1\text{-}R)^{-2}$ with

different values of reflectivity and loss for the mirrors. Here, the loss (L) is defined as 1-R-T, where R=reflectivity and T=transmittance. We see that T_{max} decreases as the reflectivity increases and dramatically approaches 0 as reflectivity is close to 1-L. In addition, T_{max} increases with the decrease of the loss.

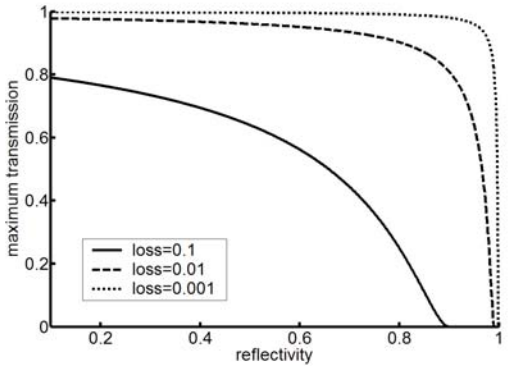

Fig. 8-2 The maximum transmission of a Fabry-Perot cavity as a function of the reflectivity of the mirror with the loss of the mirror being 0.1 (solid line), 0.01 (dashed line) and 0.001 (dotted line)

Let us define a parameter $\kappa=L(1-R)^{-1}$ to describe the effect of the loss on the maximum transmission. T_{max} is simplified as an expression of $(1-\kappa)^2$. Therefore, as $\kappa=0$, i.e. loss=0, $T_{max}=1$. In contrast, if $\kappa=1$, $T_{max}=0$. In addition, for a fixed κ, i.e. fixed T_{max}, the larger R is, the smaller L (loss) is needed. To summarize, high transmission could be obtained as $\kappa\rightarrow 0$, and this could be realized by diminishing the losses of mirrors, and preferably using mirrors with smaller reflectivity.

8.3 Implementation of bandpass waveguide filter with squared passband

As an example, a high index-contrast ridge waveguide made of Silicon (n=3.45) on a silicon dioxide (SiO_2, n=1.445) layer with width of 500 nm, height of 240 nm and deeply etched into the substrate as depicted in Fig. 8-3 is discussed in the following

sections. The holes (n=1) are drilled deeply into the substrate as well. The period of the structure is 430 nm. A 3D FDTD method has been used to simulate the devices with the fundamental TE mode incident into the waveguide. To accomplish high performance bandpass filter, two main issues are addressed: (1) high transmission in the passband and (2) flat-top passband.

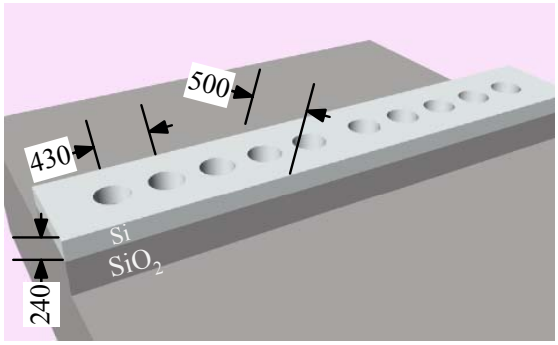

Fig. 8-3 Schematic structure of photonic bandgap monorail waveguide. Unit of each label is nm.

A. Maximum transmission

As discussed in the previous section, one approach to acquire high transmission is to minimize the loss of the photonic bandgap mirror. Two different photonic bandgap mirrors are discussed in this subsection: (a) photonic bandgap mirror without a mode matching section and (b) mirror with mode-matching holes at both sides of the mirror, as displayed in the insets of Fig. 8-4(a) and (b), respectively. The corresponding simulated reflection and loss spectra for these two mirrors are graphed in Fig. 8-4. The mirror in Fig. 8-4(a) provides a bandgap wavelength ranging from 1100 to 1670 nm and that in Fig. 8-4(b) has a high-reflection zone from 1120 to 1770 nm with slightly larger reflectivity than that of Fig. 8-4(a). By examining their loss spectra, we find that the minimal loss occurs in the 1400~1600 nm region, the desired operation spectrum. The loss in Fig. 8-4(a) at the wavelength of 1550 nm is roughly 0.04 and that for Fig. 8-4(b) is

20 times smaller, i.e. 0.002. The calculated κ for these mirrors are 0.9 and 0.16, respectively, and hence we could expect that the corresponding T_{max} constructed by these two mirrors would be 0.01 and 0.7 without considering the coupling effect between the radiation mode inside the defect and the Bloch wave in the mirror, i.e. assuming h=0.

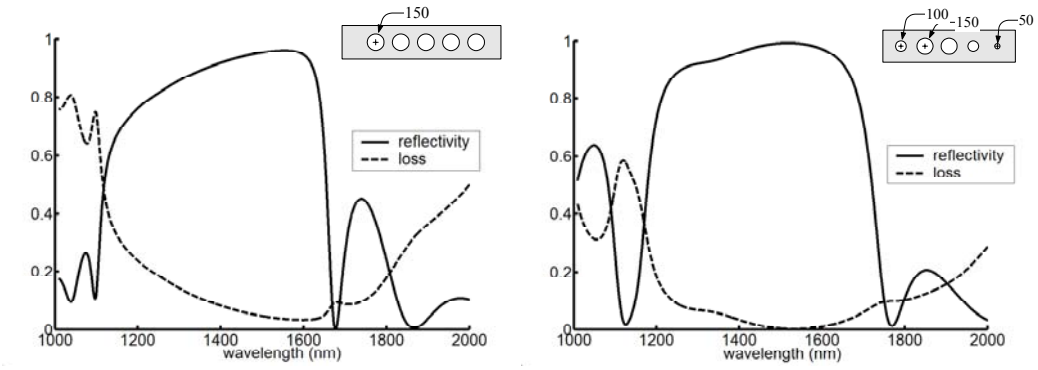

(a) (b)

Fig. 8-4 Reflection (solid line) and loss (dashed line) spectrum of the mirrors (a) without and (b) with mode-matching section. The inset of each figure is the schematic diagram of the simulated photonic bandgap mirrors.

Fig. 8-5(a) and (b) shows the simulated and calculated transmission spectra of a Fabry-Perot resonator constructed by Fig. 8-4(a) with a cavity's length of 388 nm and by Fig. 8-4(b) with the cavity's length of 366.5 nm. The calculated results are obtained by inserting the simulated reflectivity data obtained in Fig. 8-4 into Eq. (8.4) with h=0. The structure of each filter is depicted in the inset of the corresponding figure. The figures indicate that the cavity consisting of mirrors in Fig. 8-4(a) has the maximum transmission of 0.052 at the resonant wavelength of 1554 nm and that constructed by mirror in Fig. 8-4(b) possesses the maximum transmission of 0.74 at the resonant wavelength of 1554 nm. Compared to the calculated results, we find that the discrepancy ascribed to interactions between radiation mode and Bloch wave is negligible for the small κ case. Therefore, the transmission of a photonic bandgap microcavity filter made by the mirror

with small κ could be predicted by use of Eq. (8.4) with $h(p_{12},p_{21}\ldots)=0$ at the expense of slight variations of transmission at resonant wavelength. We also conclude that the mode matching sections are necessary to reduce the loss of the mirror and obtain high transmission.

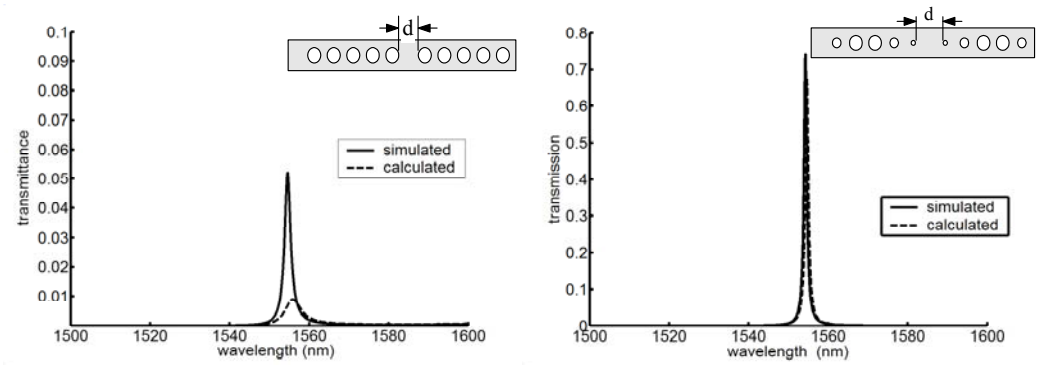

(a) (b)

Fig. 8-5 Numerically simulated (solid line) and theoretically calculated (dashed line) transmission spectra of a Fabry-Perot cavity as a function of wavelength constructed (a) by the mirror in Fig. 8-4(a) and (b) by the mirror of Fig. 8-4(b). The Insets show the simulated structures of Fabry-Perot resonators with d=388 and 366.5 nm.

B. Flat-top passband

As concluded in the previous section, the performance of a photonic bandgap waveguide microcavity filter constructed by photonic bandgap mirrors with small losses (i.e. $\kappa \ll 1$) could be expressed as a Fabry-Peort resonator. According to the principles of thin film bandpass filter design shown in Chapter 3 , a Fabry-Perot resonator with flat-top and high transmission passband is achieved by satisfying the following conditions [19]-[20].

$$\Phi = 2\beta_g d - 2\phi_A = 2m\pi \quad \text{.....(8.5)}$$

$$\frac{d\Phi(\lambda_0)}{d\lambda} \approx 0 \quad \text{.....(8.6)}$$

where Φ is the total phase shift accumulated inside cavity C, ϕ_A is the reflection phase of system A_1 or A_2, m is an integer and λ_0 is the center wavelength.

B.1 Photonic crystal mirror with the anomalous dispersion reflection phase

In order to satisfy Eq. (8-6), we learned in Chapter 3 that a specific mirror possessing anomalous dispersion region in its reflection phase is required, (AD mirror), and could be realized by use of a multiple-defect resonant mirror structure. In addition, an AD mirror with a one-defect structure is sufficed if the reflectivity of the mirror next to the input medium (called input mirror) is larger than that next to the output medium (called output mirror) [25],[26]. The anomalous dispersion region in reflection phase is obtained at the wavelength where the local minimal reflectivity occurs, i.e. the total phase shift inside the defect is $2m\pi$, where m is an integer.

An example demonstrating a one-defect AD mirror made of a monorail waveguide is presented in Fig. 8-6(a). The device is constructed by using the mirror in Fig. 8-4(b) as the input mirror and a three-hole mirror with the radii of 100, 100 and 50 nm (right to left in Fig. 8-6(a)) , as the output mirror. The separation distance between these two mirrors is defined as d_1. In order to obtain the local minimal reflectivity at 1554 nm, the length of the defect is chosen to be 380 nm. Fig. 8-6(b) shows the reflectivity and loss spectra of this AD mirror. We observe a dip in the reflection spectrum occurs at 1554 nm, but there is also a small spike in the loss spectrum at the same wavelength. The loss at 1554 nm is 0.006, roughly 3 times larger than that of the mirror in Fig. 8-4(b). κ becomes 0.043, much smaller than that of the photonic bandgap mirror, and T_{max} is expected to be roughly 0.91 as using this AD mirror to construct a

waveguide filter. Fig. 8-6(b) shows the calculated reflection phase of the AD mirror in the spectrum of 1545~1565 nm. We observe an AD region ranging from 1551 to 1556nm and expect to obtain a flat passband in this region as we properly tune the cavity's length to satisfy the conditions of Eq. (8-6).

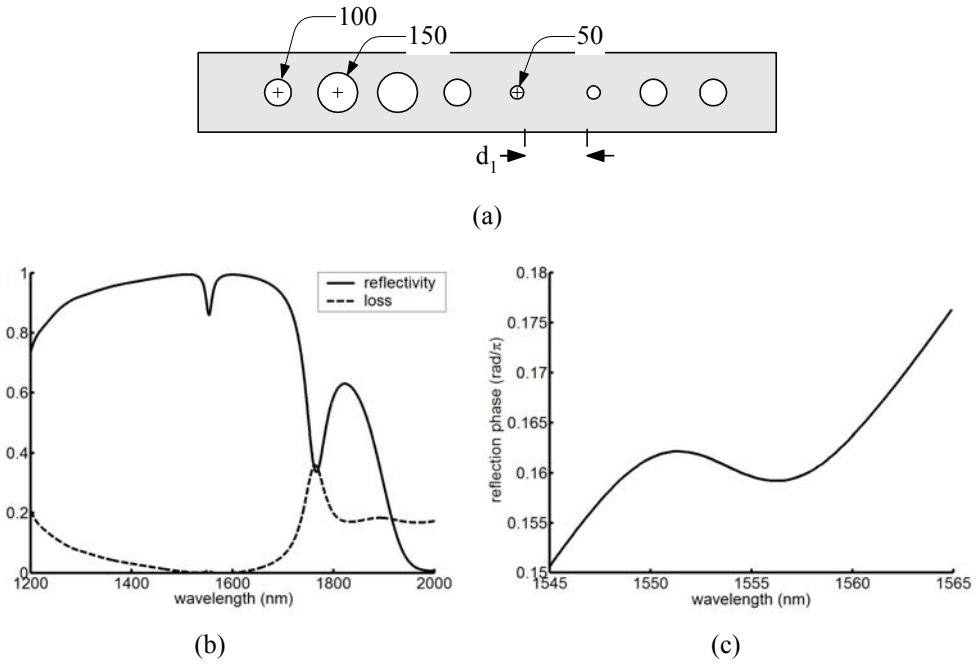

Fig. 8-6 (a) Schematic structure of the one-defect AD mirror with the defect length of d_1. Units are in nm. (b) Reflection (solid line) and loss (dashed line) spectra of the AD mirror with d_1=380 nm (c) Calculated reflection phase of the AD mirror

B.2 Flat-top bandpass waveguide filter

A Fabry-Peort resonator made of the two aforementioned AD mirrors separated by a cavity of d in length is depicted in the inset of Fig. 8-7(a). To satisfy the conditions of Eq. (8.5) and (8.6), d is chosen as 367 nm. Fig. 8-7(a) shows the transmission spectra of the Fabry-Perot resonator with d=367 nm both simulated by using the FDTD method and calculated by using Eq. (8-4) with h=0. We see a flat-top passband centered at the wavelength of 1554 nm. The simulated data illustrates the maximal transmission of 0.88,

and FWHM of 13.6 nm. The bandwidth at -0.5 dB transmission deduction levels is 8.86 nm. The simulated results are in close agreement with the calculated data, except in the region of the high-transmission passband where a slight reduction in transmission (~0.03) is observed. This discrepancy implies that the radiation field slightly reduces the output field in this passband. Fig. 8-7(b) shows the total phase shift Φ as a function of the wavelength, and we see an approximately constant (~2π) at the wavelength of 1551~1556 nm, corresponding to the flat region of the passband.

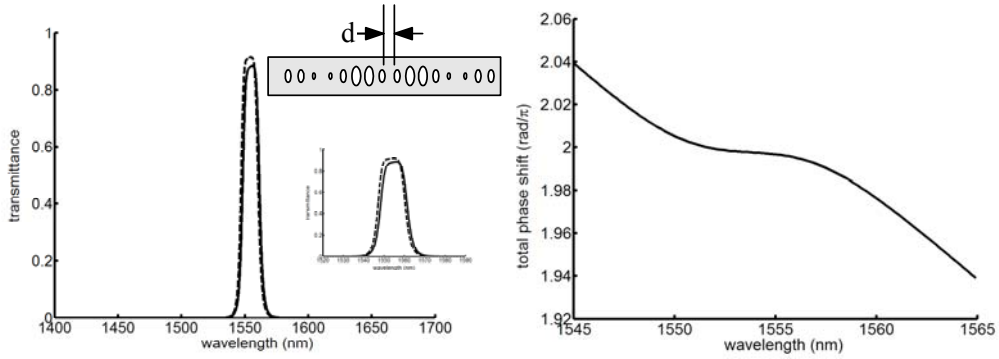

(a) (b)

Fig. 8-7 (a) Simulated (solid line) and calculated (dashed line) transmission spectra of the microcavity with the length of the cavity d=367 nm. The top inset shows the schematic diagram of the simulated photonic bandgap waveguide microcavity filter and the lower inset shows the detailed result around the resonance at 1550 nm. (b) Calculated total phase shift inside the cavity

8.4 Conclusion

By applying thin-film bandpass filter design methodology, we present the design procedures to implement a multiple-defect photonic bandgap waveguide bandpass filter with the characteristics of a flat-top passband and a wide stopband. The first step of the design is to realize an AD mirror, for example, by use of a one-defect structure with reflectivity of the input mirror larger than that of the output mirror and by properly choosing the defect length such that the resonance is located at the center wavelength of

the anomalous dispersion region of reflection phase. . Then, a multiple-defect bandpass filter with a nearly rectangular passband is obtained by constructing two identical AD mirrors separated by a cavity with appropriate length such that the round-trip phase shift inside the cavity satisfies the resonance condition and compensates for the phase dispersion caused by the AD mirrors, resulting in enhanced transmission and flat transmission band.

In order to improve the performance of the filters, the losses of the photonic bandgap mirrors are minimized by adding the mode-matching sections. In the case of $\kappa<<1$ the transmission of the photonic bandgap microcavity filter can be calculated by using the expression of a Fabry-Perot resonator with a slight variation of the maximum transmission. Although the construction of an AD mirror by using one-defect structure results in higher loss than that of a photonic bandgap mirror, the reduction of reflectivity in the concerned spectrum diminishes κ, thereby increasing the maximum transmission of this type of Fabry-Perot filters. With the example of a three-defect bandpasss waveguide filter shows a maximum transmission of 0.88 at 1554 nm, FWHM of 13.6 nm and the width at -0.5 dB transmission deduction level of 8.86 nm. A better performance could be achieved by optimally minimizing the losses of the AD mirrors.

References

[1] JS Foresi, PR Villeneuve, J Ferrera, ER Thoen, G Steinmeyer, S Fan, JD Joannopoulos, LC Kimerling, HI Smith, EP Ippen, "Photonic-bandgap microcavities in optical waveguides," Nature 390, 143-145 (1997)

[2] P Rigby, TF Krauss, "Photonics - The Vs and Qs of optical microcavities," Nature 390, 125-125 (1997)

[3] J.P. Zhang, D.Y. Chu, S.L. Wu, W.G. Bi, R.C. Tiberio, R.M. Joseph, A. Taflove, C.W. Tu, S.T. Ho, "Nanofabrication of 1-D Photonic Bandgap Structures Along Photonic Wire," IEEE Photon. Technol. Lett. 8, 491 (1996).

[4] DJ Ripin, KY Lim, GS Petrich, PR Villeneuve, SH Fan, ER Thoen, JD Joannopoulos, EP Ippen, LA Kolodziejski, "One-dimensional photonic bandgap microcavities for strong optical confinement in GaAs and GaAs/AlxOy semiconductor waveguides," J Lightwave Technol. 17 (11), 2152-2160 (1999)

[5] KY Lim, DJ Ripin, GS Petrich, LA Kolodziejski, EP Ippen, M Mondol, HI Smith, PR Villeneuve, S Fan, and JD Joannopoulos, "Photonic band-gap waveguide microcavities: Monorails and air bridges," J Vacuum Sci & Technol B 17 (3), 1171-1174 (1999)

[6] JC Chen, HA Haus, Shanhui Fan, PR Villeneuve, and JD Joannopoulos, "Optical filters from photonic band gap air bridges," J Lightwave Techno. 14(11), 2575-80 (1996)

[7] TF Krauss, B Vogele, CR Stanley, and De La Rue RM," Waveguide microcavity based on photonic microstructures," IEEE Photonics Technol Lett 9(2), 176-178 (1997)

[8] A.S. Jugessur, P. Pottier, R.M. De La Rue, "One-dimensional periodic photonic crystal microcavity filters with transition mode-matching features, embedded in ridge waveguides," Electron. Lett. 39, 367-369 (2003).

[9] C. Sauvan, G. Lecamp, P. Lalanne, and J. P. Hugonin, "Modal-reflectivity enhancement by geometry tuning in photonic crystal microcavities," Opt. Express 13**,** 245-255 (2005), http://www.opticsexpress.org/abstract.cfm?URI=OPEX-13-1-245

[10] Lalanne P, Hugonin JP, "Bloch-wave engineering for high-Q, small-V microcavities," IEEE J Quantum Electron 39 (11), 1430 –1438 (2003)

[11] P. Lalanne, S. Mias, and J. P. Hugonin, "Two physical mechanisms for boosting the quality factor to cavity volume ratio of photonic crystal microcavities," Opt. Express 12, 458-467 (2004), http://www.opticsexpress.org/abstract.cfm?URI=OPEX-12-3-458

[12] D. Peyrade, E. Silberstein, P. Lalanne, A. Talneau, Y. Chen, "Short Bragg mirrors with adiabatic modal conversion," Appl. Phys. Lett. 81, 829-831 (2002)

[13] A. S. Jugessur, P. Pottier, and R. M. De La Rue, "Engineering the filter response of photonic crystal microcavity filters," Opt. Express 12**,** 1304-1312 (2004), http://www.opticsexpress.org/abstract.cfm?URI=OPEX-12-7-1304

[14] H. A Macleod, *Thin-film optical filters*, 3rd ed. (Philadelphia, Institute of Physics Pub., 2001).

[15] A. Thelen, *Design of optical interference coatings* (New York, McGraw-Hill, 1989).

[16] R. Zengerle and O. Leminger, "Phase-Shifted Bragg-Grating Filters with Improved Transmission characteristics," J. Lightwave Technol. 13, 2354-2358 (1995).

[17] K. Madsen and J. H. Zhao, *Optical filter design and analysis: a signal processing approach* (Wiley, New York, 1999).

[18] A Melloni and M. Martinelli, "Synthesis of direct-coupled-resonators bandpass filters for WDM systems," J Lightwave Technol 20(2), 296-303 (2002)

[19] YV. Troitski, "Dispersion-free, multiple-beam interferometer," Appl. Opt. 34**,** 4717-22 (1995).

[20] C-H Chen, K Tetz, W Nakagawa, and Y. Fainman, "Wide-field-of-view GaAs/AlxOy one-dimensional photonic crystal filter," Appl Opt. 44 (8), 1503-1511 (2005)

[21] S. D. Smith, "Design of multilayer filters by considering two effective interfaces," J. Opt. Soc. Am. 48, 43-50 (1958)

[22] G Sztefka, HP Nolting, "Bidirecitonal eigenmode propation for large refractive-index step," IEEE Photon Technol Lett. 5 (5), 554-557 (1993)

[23] J Ctyroky, S Helfert, R Pregla, "Analysis of a deep waveguide Bragg grating," Opt. & Quantum electron 30 (5-6), 343-358 (1998)

[24] J. Willems, J Haes, R. Baets, "The bidirectional mode expansion method fro two-dimensional waveguides: the TM case," Opt. & Quantum Electron 27 (10), 995-1007 (1995)

[25] Y. Y Troitski, "Dielectric mirrors with the anomalous dispersion of the reflection phase," Optics and Spectroscopy 77, 503-506 (1994).

[26] C-H Chen, K Tetz, and Y Fainman, "Resonant-cavity-enhanced PIN photodiode with broad quantum efficiency spectrum by use of an anomalous dispersion mirror," Appl. Opt. 44(29), 6131-6140, (2005)

Chapter 9 Conclusions

9.1 Summary

This dissertation presents the investigation of optical micro and nano-cavities, primarily for optical communication applications. These micro-cavities are expected to become crucial building blocks in future miniaturized and integrated photonic devices and systems. For a free-space optical communication system, a resonant filter and a resonant photodiode with the properties of flat-top transmission and angular insensitivity were designed, fabricated and characterized. In addition, systematic design methodologies to mathematically analyze these two different devices and to systematically optimize the design parameters of transmissions and angular bandwidths were developed. For the applications of the integrated photonic circuits, a waveguide polarizer with TM-wave passing and a waveguide bandpass filter with flat-top transmission band were designed. With the introduction of the nanostructures into the conventional waveguides, form birefringence is obtained as a result of the geometric variations within the structures. This type of waveguides is a promising candidate for future miniaturized on chip polarization-selective devices such as polarizers, polarization splitters, and polarization delay-lines due to dramatically different propagation velocities for different polarization modes inside these waveguides.

The contribution of each chapter was addressed as follows. In Chapter 3, we presented the analysis of microcavities in 1-Dl photonic crystal structure and described the optimized conditions to achieve a maximally flat bandpass filter. In addition, we

developed the technique to specifically design a cascaded of microcavities as frequency-dependent mirrors with anomalous dispersion region in reflection phases. These mirrors are necessary to realize a ripple-free transmission filters. To demonstrate the usefulness of our design algorithms, an example of a bandpass filter construction is presented.

In Chapter 4, we included the design parameter of angular bandwidth into the methodology developed in the previous chapter, and realized a resonant spectral filter with a wide stop band and a flat-top passband based on a $GaAs/Al_xO_y$ material system by adjusting the optical thickness ratio of the cascaded microcavity based mirrors in a high-index-contrast materials system with the optimization of the transmission bandwidth, shape and angular sensitivity characteristics simultaneously. The devices were fabricated by MBE growth and characterized experimentally. The measured results were found to be in agreement with the optimized design.

In Chapter 5 and 6, we first analyze theoretically the optimized conditions to achieve a resonant photodiode with high quantum efficiency over a broad spectral region by replacing the standard Bragg mirror with an AD mirror as the entrance mirror and by controlling the slope of the round-trip phase shift inside the active layer. In addition, we discuss the trade-off between the bandwidth of the transmission spectrum and angular sensitivity by adjusting the optical thickness ratio of the mirror and varying the thickness of the active layer. We found that the thickness of the active layer plays an important role in the determination of angular bandwidth. A proof-of-concept photodiode is fabricated and characterized. The discrepancy between the simulated design and actual device results from the fabrication error of the layer thickness growth and from neglecting the materials dispersion in the design.

In Chapter 7 and 8 we discussed of the approach of introducing nanostructures within optical waveguides. Specifically, we designed two different polarization-dependent devices by use of the nanostructures and the microcavities. First, we found that significant form birefringence is obtained as the nanostructure is introduced into the waveguide. Based on this effect, we designed a compact TM-pass waveguide polarizer that utilizes the significant difference in cutoff wavelength for each polarization mode in the waveguides with nanostructures. Next, we designed a photonic bandgap microcavity waveguide filter with flat-top transmission band by applying the methodology obtained in Chapter 3 . With the introduction of the mode-matching structure that minimizes the losses of the mirrors and reduces their reflectivities, a multiple-defect waveguide microcavity filter with high transmission, flat-top passband and wide stopband was achieved.

9.2 Future directions

During the last few years, the research field of microcavities and nanocavities is rapidly growing, as these structures are expected to become crucial building blocks in large variety of optical devices and systems. In the following we are briefly describe the potential areas of the applications that would benefit from such structures.

A. Characterization of integrated photonic devices

The experimental verification of the designed devices is critical, as it allows to validate the design principles and the simulations tools, to calibrate the fabrication processes and to provide potential opportunities to investigate the unrevealed or ignored phenomena in the original designs. In this thesis, we demonstrated devices for the

photodetection systems. Nevertheless, the integrated photonic devices with nanostructures are remained to be realized and be characterized. Near-field optical microscopy is a valuable tool for nanoscopic imaging, since the optical signal is collected in the near field, allowing to measure near field interactions and evanescent fields, usually unrevealed by standard measurement techniques. Therefore, in the future, we would like to apply near field microscopy to characterize not only the power spectra of the integrated photonic devices but also the near field distribution along the nanostructures.

B. Nonlinear optics

Multiple-wave mixing processing occurs, as the amplitudes of the electric fields become so large that in a highly polarizable nonlinear medium the nonlinear optical interactions where the photons interact with each other are come about. The electromagnetic fields inside the cavity are enhanced by the order of the finesse, and conversion efficiencies of nonlinear processes can be increased dramatically as nonlinear materials are inserted as the cavities. Therefore, with integration of the nonlinear materials into a microcavity structure, the devices can become high-speed active optical components. In the future, the research would cover the development of methods to design the microcavity mirrors to satisfy the phase matching and the resonance conditions for each of the involved frequencies. We should also develop the simulation tools to calculate the nonlinear effect for the multiple-cavity structures, as well as fabrication and characterization of techniques to demonstrate the concepts and the designed devices.

C. Photonic integrated circuits

With the advent of photonic crystals and the development of nanofabrication technology, large-scale miniature and integrated photonic integrated circuits are becoming a reality rather than a dream. The size of the resonant ring cavity is reduced to ~μm, and 90 degree bending is achievable. By using high index-contrast waveguides integrated with nanostructures, the integrated optical components not only have smaller sizes and low power requirements, but also allow a diversity of unique characteristics to be realized in these types of devices. We anticipate that a multiplicity of other unique properties of nanostructures integrated into different developed optical components will be discovered, and innovative optical integrated devices with multiple functionalities will become available with advantages of reduced dimensions as well as enhancement of performance.

D. Optical sensing systems

Devices and systems for sensing are widely applied in the areas of industry, civil engineering, medicine, defense and research, and a variety of optical sensors are used for measurements of physical and electrical parameters such as temperature, pressure, current, chemicals, and biomolecules. Research is focused on developing cost effective, miniaturized devices with high sensitivity, and low –power consumption. Integration of nanophotonics–based sensors with the integration of nanoscale optoelectronics and nonostructured transducers are expected to be a useful approach to achieve these features.